

AD-A032 262

VON KARMAN INST FOR FLUID DYNAMICS RHODE-SAINT-GENESE--ETC F/G 20/4
FILM COOLED SMALL TURBINE BLADE RESEARCH. VOLUME I. AERODYNAMIC--ETC(U)
JUN 76 C SIEVERDING, P MARCHAL

DA-ERO-75-6-074

NL

UNCLASSIFIED

1 OF 2
AD
A032 262



OF 2
2262

AD

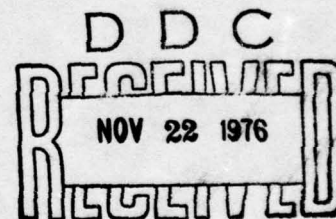
FILM COOLED SMALL TURBINE RESEARCH

VOL.I - AERODYNAMIC STUDY OF SECONDARY FLOWS

1st Year Annual Report

C. SIEVERDING and F. MARCHAL

JUNE 1976



B

EUROPEAN RESEARCH OFFICE
United States Army
London, U.K.

Grant Number DA - ERO - 75-G-074
von KARMAN INSTITUTE FOR FLUID DYNAMICS
Approved for public release; distribution unlimited

AD A032262

UNCLASSIFIED

SECURITY CLASSIFICATION OF THIS PAGE (When Data Entered)

REPORT DOCUMENTATION PAGE		READ INSTRUCTIONS BEFORE COMPLETING FORM
1. REPORT NUMBER	2. GOVT ACCESSION NO.	3. RECIPIENT'S CATALOG NUMBER
4. TITLE (and Subtitle) (6) FILM COOLED SMALL TURBINE BLADE RESEARCH. Volume I. PART I: AERODYNAMIC STUDY OF SECONDARY FLOWS PART II: FILM COOLING EFFECTIVENESS AT SIMULATED TURBINE CONDITIONS		5. TYPE OF REPORT & PERIOD COVERED 1st YEAR ANNUAL REPORT DEC 75 - JUNE 76
7. AUTHOR(s) (10) PART I: C. SIEVERDING & P. MARCHAL PART II: B. E. RICHARDS, J.P. VILLE & C. APPELS		6. PERFORMING ORG. REPORT NUMBER
9. PERFORMING ORGANIZATION NAME AND ADDRESS VON KARMAN INSTITUTE FOR FLUID DYNAMICS 1640, RHODE-SAINT-GENESE, BELGIUM		8. CONTRACT OR GRANT NUMBER(s) DAERO-75-074 (15) VDA-ERO-75-G-074
11. CONTROLLING OFFICE NAME AND ADDRESS USA R&S GP (EUR) BOX 65, FPO NEW YORK 09510		10. PROGRAM ELEMENT, PROJECT, TASK AREA & WORK UNIT NUMBERS 61102A-1T161102B35E 00-530 (16) (17)
14. MONITORING AGENCY NAME & ADDRESS (if different from Controlling Office)		12. REPORT DATE (11) JUNE 1976 (12) 152 P.
		13. NUMBER OF PAGES PART I: 81 PART II: 67
		15. SECURITY CLASS. (of this report) UNCLASSIFIED
		15a. DECLASSIFICATION/DOWNGRADING SCHEDULE
16. DISTRIBUTION STATEMENT (of this Report) APPROVED FOR PUBLIC RELEASE DISTRIBUTION UNLIMITED		
17. DISTRIBUTION STATEMENT (of the abstract entered in Block 20, if different from Report) (9) Annual rept. no. 1 for period ending Jun 76,		
18. SUPPLEMENTARY NOTES		
19. KEY WORDS (Continue on reverse side if necessary and identify by block number) (U) PROPULSION (U) INTERNAL FLOWS (U) FILM COOLING (U) CASCADE FLOWS		
20. ABSTRACT (Continue on reverse side if necessary and identify by block number) SEE OVER		

DD FORM 1 JAN 73 1473 EDITION OF 1 NOV 65 IS OBSOLETE

UNCLASSIFIED

SECURITY CLASSIFICATION OF THIS PAGE (When Data Entered)

367 475

20. ABSTRACT

The overall study concerns an investigation on the cooling and aerodynamic problems associated with a high speed turbine cascade of small blade height for use on small gas turbines. The secondary flow behavior in turbines is presented in Vol. I and the cooling aspects are presented in Vol. II.

Vol. I reports on the study of small aspect ratio blades. A program has been initiated with the aim of obtaining a better physical understanding of the real secondary flow phenomenon. The total program will cover a period of three years. It includes very detailed low speed tests with measurements inside the blade passage, cross checking of the low speed tests in a high speed cascade and the investigation of the effect of film cooling on secondary flows. Vol I, which reports on the first year efforts, presents mainly low speed test results and a limited amount of high speed data.

Vol. II reports on the first year efforts on the measurement of effectiveness of a film cooling system for a small turbine by injection through inclined holes. A short duration facility was used to provide isothermal wall data at flow conditions carefully selected to simulate those expected in an advanced turbine. Appropriate heat and mass transfer equations have been developed to illustrate the interpretation and usefulness of data obtained in this as yet relatively unconventional method. The measurements showed: that there are small increases in effectiveness for injection on convex surfaces compared to flat surfaces; a change in flow Reynolds number only slightly changes effectiveness; a lowering of the mainstream Mach number from 0.6 to 0.3 causes a sizable decrease in effectiveness; a pressure gradient, typical of that seen on a turbine also decreases considerably the effectiveness.

ACCESSION for	
NTIS	White Section <input checked="" type="checkbox"/>
DDC	Buff Section <input type="checkbox"/>
UNANNOUNCED	<input type="checkbox"/>
JUSTIFICATION.....	
BY.....	
DISTRIBUTION/AVAILABILITY CODES	
Dist.	AVAIL. and/or SPECIAL
A	

FOREWORD

The overall study concerns an investigation on the cooling and aerodynamic problems associated with a high speed turbine cascade of small blade height for use on small gas turbines. The cooling aspects are presented in vol.2 of this report.

The present report vol.1 is confined to the study of small aspect ratio blades. The program has been initiated with the aim of obtaining a better physical understanding of the real secondary flow phenomenon. The program was layed out for a period of three years. It includes very detailed low speed tests with measurements inside the blade passage, cross checking of the low speed tests in a high speed cascade and the investigation of the effect of film cooling on secondary flows. This report presents mainly low speed test results and a limited amount of high speed data.

TABLE OF CONTENTS

FOREWORD

LIST OF FIGURES

LIST OF SYMBOLS

1. INTRODUCTION	1
2. LOW SPEED TESTS	3
2.1 Test program	3
2.2 The wind tunnel	3
2.3 Blades and instrumentation	4
2.4 Inlet and outlet flow field - overall performance test results	5
2.4.1 Test description	6
2.4.2 Measurements uncertainties	6
2.4.3 Discussion of test results	10
2.5 Comparison with a simplified theoretical model	17
2.5.1 Flow angle distribution	17
2.5.2 Profile losses	18
2.5.3 End wall losses	18
2.6 Channel flow	19
2.6.1 Flow visualizations	19
2.6.2 Blade velocity distributions	21
2.6.3 Channel flow measurements	23
2.7 Leading edge flow field	29
2.7.1 Test set-up and experimental procedure	29
2.7.2 Test results	29
2.8 Conclusions - Low speed tests	33
3. HIGH SPEED TESTS	36
3.1 Test facility and instrumentation	36
3.1.1 Test facility	36
3.1.2 Test section	36
3.1.3 Tunnel and test section instrumentation	37
3.2 Blade and cascade geometry	37
3.3 Test conditions	39
3.3.1 Variation of outlet Mach number and Reynolds number	39

3.3.2 Downstream periodicity	39
3.3.3 Flow unsteadiness	40
3.3.4 Stagnation temperature	41
3.3.5 Measuring uncertainties	41
3.4 General flow pattern - flow visualizations	42
3.4.1 Oil flow visualizations	42
3.4.2 Shadowgraphs	42
3.5 Overall performance test results	43
3.5.1 Profile losses	43
3.5.2 Outlet flow angle	45
3.6 Conclusions - High speed tests	47
REFERENCES	48
APPENDIX A - Blade coordinates and cascade configuration	51
APPENDIX B - Secondary flows in plane cascades .	53
APPENDIX C	57
TABLE 1 - Summary of overall tests parameters ..	58
TABLE 2 - Summary of test results	59

LIST OF FIGURES

- 1 Schematic diagram of the C1 wind tunnel
- 2 Inlet and blade passage probes
- 3 Outlet probe
- 4 Mechanical arrangement of the blade designed for measurements near the leading edge
- 5 Spanwise distribution of pitchwise, mass-averaged loss coefficient. Test N°2
- 6 Spanwise distribution of pitchwise, mass-averaged
 $\Delta\beta_2 = \beta_{2MS} - \beta_2(y)$. Test N°2
- 7 Spanwise distribution of pitchwise, mass-averaged
secondary velocity V_z . Test N°2
- 8 Contour plot of loss coefficient in exit plane. Test N°2
- 9 Mass-averaged total loss versus downstream distance for 3 aspect ratios
- 10a Spanwise loss distribution for 3 downstream positions.
AR = 0.42
- 10b Spanwise $\overline{\Delta\beta_2}$ distribution for 3 downstream positions.
AR = 0.42
- 11a Spanwise loss distribution for 3 downstream positions.
AR = 0.67
- 11b Spanwise $\overline{\Delta\beta_2}$ distribution for 3 downstream positions.
AR = 0.67
- 12a Spanwise loss distribution for 3 downstream positions.
AR = 0.98
- 12b Spanwise $\overline{\Delta\beta_2}$ distribution for 3 downstream positions.
AR = 0.98
- 13 Mass averaged total loss versus aspect ratio for 3 downstream distances
- 14a Spanwise loss distribution for 3 aspect ratios.
Measuring plane located at a distance of 1/3 chord length from trailing edge plane in streamwise direction
(DX/ C = 1/3)
- 14b Spanwise distribution of the outlet flow angle deviation
 $\Delta\beta_2 = \beta_{2MS} - \beta_2(y)$, for three aspect ratios (DX/ C = 1/3)
- 15a Spanwise loss distribution for 3 aspect ratios (DX/ C = 2/3)
- 15b Spanwise $\overline{\Delta\beta_2}$ distribution for 3 aspect ratios (DX/ C = 2/3)
- 16a Spanwise loss distribution for 3 aspect ratios (DX/ C = 1)
- 16b Spanwise $\overline{\Delta\beta_2}$ distribution for 3 aspect ratios (DX/ C = 1.0)

- 17 Comparison of measured losses with losses computed from various loss correlations
- 18 Beliks solution for kinetic energy of secondary flow
- 19 Dependence of endwall losses on inlet boundary layer thickness
- 20 Contour plot of loss coefficient ω for AR = 0.42
- 21a Comparison of measured and computed $\overline{\Delta\beta_2}$ distributions :
AR = 0.42
- 21b id., AR = 0.67
- 21c id., AR = 0.98
- 22 Blade suction surface flow visualisation
- 23 End wall flow visualisation
- 24 Representation of the "separation vortex", following Ref. [3]
- 25a Blade surface velocity distributions, AR = .42
- 25b Blade surface velocity distribution at mid-span, AR = .42 and .98
- 26a End wall probe assembly
- 26b View of end wall plate and probe installed
- 27 Location of experimental traverses
- 28a Growth through the turbine passage of the mass averaged loss coefficient ω_M
- 28b Growth through the turbine passage of the reduced mass averaged loss coefficient
$$= \omega_M \cdot \left(\frac{AR}{AR=.42} \right)$$
- 29a Pitchwise averaged, mass averaged loss coefficient vs blade height. AR = .98, plane 1, test NP1
- 29b Pitchwise averaged, mass averaged deviation angle
 $\Delta\beta = \beta_{MS} - \beta(y)$ vs blade height. AR = .98, plane 1 test NP1
- 29c Loss coefficient contour plot, AR = .98, plane 1, test NP1
- 30 id., AR = .98, plane 2, test NP2
- 31 id., AR = .98, plane 3, test NP3
- 32 id., AR = .98, plane 4, test NP4
- 33 id., AR = .98, plane 5, test NP5
- 34 id., AR = .98, plane 6, test NP6
- 35 id., AR = .98, plane 7, test NP7
- 36 id., AR = .42, plane 3, test NP14
- 37 id., AR = .42, plane 4, test NP13
- 38 id., AR = .42, plane 5, test NP12
- 39 id., AR = .42, plane 6, test NP11

- 40 id., AR = .42, plane 7, test NP10
- 41 id., AR = .42, plane 8, test NP9
- 42 id., AR = .67, plane 3, test NP15
- 43 id., AR = .67, plane 4, test NP16
- 44 id., AR = .67, plane 5, test NP17
- 45 id., AR = .67, plane 7, test NP18
- 46a Comparison of the results obtained with the 5-hole probe and with the 3-hole probe : loss distribution
- 46b id., deviation angle distribution
- 46c id., losses contour plot
- 47 Secondary velocities chart in plane 7, AR = .98
- 48a End wall "boundary layer" velocity profile
- 48b End wall "boundary layer" total pressure profile - traverse 1
- 49a The movable leading edge instrumented with the 5-hole probe
- 49b Close up view of the 5-hole probe mounted on the leading edge
- 50 The C1 wind tunnel instrumented for the leading edge flow field investigations
- 51 to 54 Flow angle distribution along the blade height, for the leading edge flow field tests traverses
- 55 Secondary velocities chart in a plane located 5mm upstream of the leading edge
- 56 VKI high-speed cascade facility C-2
- 57 Downstream traverse probe for high speed tests
- 58 Variation of Reynolds number with outlet Mach number
- 59 Oil flow visualizations at $M_2 = 0.5$
- 60 Shadowgraphs of cascade flow at transonic outlet Mach numbers ($M_2 = 0.9$ to 1.0)
- 61 Profile losses versus outlet Mach numbers. Comparison of measured and predicted profile losses
- 62 Predicted profile loss variation in function of inlet flow angle at $M_2 = 0.8$ (based on Craig-Cox correlation [6])
- 63 Outlet flow angle versus outlet Mach number. Comparison of measured and predicted flow angles

LIST OF SYMBOLS

AR	aspect ratio h/c
B	proportionality factor between inlet vorticity and the streamwise component of vorticity at exit
c	chord
CA	axial chord
DX	distance in the streamwise direction
DA	distance in the axial direction
H_{12}	momentum form factor, δ_x^x / θ_x
H_{32}	energy form factor δ_x^{xx} / θ_x
h	blade height
KE_s	kinetic energy of secondary flow, $\frac{1}{2h s \cos\beta_2} \int_0^h \int_0^s \cos\beta_2 (v_y^2 + v_z^2) dz dy$
M	Mach number
P	pressure
q	dynamic head
R	radius of curvature
RE	Reynolds number
s	blade spacing, or arc length
T	temperature
T_u	turbulence level
V	magnitude of absolute velocity
x	coordinate in the direction of the free stream flow
y	coordinate normal to the wall
z	coordinate normal to the direction of the free stream flow and parallel to the wall

β	flow angle with respect to axial direction
γ	blade stagger angle with respect to axial direction
δ	boundary layer thickness
δ_x^*	$\int_0^{h/2} \left(1 - \frac{V_x}{V_{FS}}\right) dy$
δ_z^*	$\int_0^{h/2} \frac{V_z}{V_{FS}} dy$
ϵ	non-periodicity factor
θ	flow turning $\beta_1 - \beta_2$
θ_x	$\int_0^{h/2} \left(1 - \frac{V_x}{V_{FS}}\right) \frac{V_x}{V_{FS}} dy$
θ_z	$\int_0^{h/2} \left(\frac{V_z}{V_{FS}}\right)^2 dy$
ν	kinematic viscosity
ξ	loss coefficient $- 1 - \frac{V_2^2}{V_{2,IS}^2}$
ρ	density
σ	cascade solidity, c/s
ω	total pressure loss coefficient
	$\frac{\overline{P_{01}}_{MS} - P_{02}}{(\overline{P_{01}} - \overline{P_2})_{MS}}$
ω'	total pressure loss coefficient
	$\frac{P_{01} - P_{02}}{(\overline{P_{01}} - \overline{P_2})_{MS}}$
ω_{kin}	secondary flow kinetic energy loss coefficient
	$\frac{KE_s}{(\overline{P_{01}} - \overline{P_2})_{MS}}$

SUBSCRIPTS

0	total or stagnation conditions
1	upstream conditions
2	downstream conditions
a	axial component
A	area averaged value
FS	free stream
LE	leading edge
l	local value
M	mass averaged value
MS	mid span
ref	reference
s	secondary
TE	trailing edge
x	denotes a component in the direction of the free-stream flow
y	denotes a component normal to the wall
z	denotes a component normal to the direction of the free-stream flow and parallel to the wall.

SUPERSCRIPTS

(-)	a pitchwise average value at a given spanwise station
(=)	an average over the entire measuring plane

1. INTRODUCTION

The design and operation of a high performance, film cooled gas turbine of small blade height with respect to chord represents a difficult problem in view of the small dimensions of the flow passages. The flow is dominated by interference effects between blade and wall boundary layers which influence strongly the blade performance. It has been recognized that the lack of reliable secondary flow prediction methods are one of the major obstacles for a further improvement of small gas turbines. Conventional secondary loss correlations have proved to be insufficient and unreliable. A new approach providing a better physical understanding of the flow is needed. A research program is underway at VKI to help to fill this gap. The work carried out under contract for the US Army is part of this program.

The main part of the experimental work during the first year of the contract was conducted in the low speed cascade tunnel of the von Karman Institute. These tests aim at a better understanding of the real 3-dimensional character of the flow in turbine nozzle vanes. Detailed investigations of the flow field upstream and downstream of the cascade as well as inside the blade passage provide information on the development of secondary flows and the growth of the endwall boundary layer.

The low speed tests are performed using three different blade heights at constant chord length in order to study the influence of aspect ratio. The Reynolds number and the inlet side wall boundary layer are kept constant during the whole test series.

The 3-years program foresees to extend the secondary flow investigations also to the high speed flow range. These tests are to be carried out in the VKI-high speed cascade tunnel

C-2. Up to now the high speed test program has been limited to mid-span performance measurements in the outlet Mach number range $0.4 < M_2 < 0.9$ for the inlet angles $\beta_1 = 75^\circ, 90^\circ$ and 105° .

2. LOW SPEED TESTS

2.1 Test program

The experiments are carried out on a typical subsonic nozzle blade with a thick trailing edge for cooling purposes. As already mentioned before the tests will be carried out for 3-different aspect ratios at constant RE-number and constant inlet endwall boundary layer thickness.

The test program may be divided into three phases :

The first phase deals with the investigation of the flow field downstream of the trailing edge, at several streamwise distances from the trailing edge plane, in order to study the flow pattern evolution downstream of the cascade.

The second phase is concerned with the measurements of flow parameters inside of the blade passage.

In the third phase of the test program special attention is given to the investigation of the leading edge stagnation vortex ("horseshoe vortex") which is likely to influence the flow field in this region.

2.2 The wind tunnel

The C-1 low speed cascade wind tunnel of the von Karman Institute turbomachinery laboratory is used in the present investigations. A schematic diagram of this facility is shown in Fig.1. Air is driven from the atmosphere by a centrifugal blower powered by a 25 HP DC motor. The speed of the blower is controlled by a rehostat, the maximum air speed in the rectangular air section (approx. dimensions 11.7 x 50cm) is about 40m/s.

The tunnel has a non-return arrangement, discharging into the atmosphere.

The cascade inlet wall boundary layer is the result of natural development between the settling chamber and the cascade. The variation of the aspect ratio being obtained by a variation of the blade height, a movable side wall was required; this movable wall extends upstream up to the settling chamber in order to maintain the same boundary layer thickness on both side walls.

2.3 Blades and instrumentation

Blade section coordinates and cascade description are given in Appendix A. The blade profile corresponds to the stator hub section of a small high temperature gas turbine (see Ref. |1|).

A 3-hole (2-directional) probe is used for the inlet flow field and the main bulk of the measurements within the blade passages (Fig.2a). Some of the blade passage measurements are repeated by a 5-hole (3-directional) probe (Fig.2b) in order to estimate eventual measuring errors incurred by the use of the 3-hole probe in a 3-d flow. The dynamic head is evaluated from the difference between the total pressure and the average pressure sensed by the 2 (4) directional tubes. Probe calibration leads then to the determination of the true dynamic pressure.

The probe used in the downstream flow investigations is shown in Fig.3. It is of the fork-type. One of the two stems is a Kiel probe that proved under calibration to yield the true total pressure over an angular range of $\pm 25^\circ$; the second stem has two tubes cut at 90° angle at the tip for purpose of sensing the local flow direction. The dynamic head is obtained in the same manner as for the other probe. The fact that the two stems are separated by 10mm is taken into account by the data reduction program.

The pressures measured by the probes are sensed by strain gauge transducers. The signals from these transducers are processed through a digital voltmeter, and the output of the digital voltmeter is punched on paper tape which is processed on a MITRA 15 computer. The data acquisition program includes correction due to instrumentation system and probe calibration.

The investigation of the leading edge flow field presents a particular problem because of the unavoidable distortion of the leading edge flow by any probe placed near the leading edge. This problem was mastered by designing a blade with a hollow movable nose, allowing to put the probe inside the blade nose, the spanwise traverses being done by moving the blade nose*. The mechanical arrangement is shown in Fig.4. The probe used for these tests is the miniaturized 5-hole probe of Fig.2b.

Hot wire anemometry was used to check in some cases the pressure probe measurements.

Blades instrumented with pressure tapings at various spanwise positions allow the measurement of span and chordwise blade pressure distributions, through an alcohol multimanometer.

2.4 Inlet and outlet flow field - overall performance test results

This section deals with the detailed tests performed downstream of the cascade by difference with the far upstream conditions.

* see also first periodic report, June-November 1975.

2.4.1 Test description

The flow quantities to be measured are : the flow direction, the total pressure and the dynamic pressure. The upstream measurements are performed at a distance of 1 chord length with respect to the leading edge plane, while the downstream measurements are made in 3 different planes positioned at 1/3, 2/3 and 1 chord length in flow direction behind the trailing edge plane. These tests are repeated for each of the three selected aspect ratios : $h/c = 0.42, 0.67$ and 0.98 .

At the upstream station, three traverses perpendicular to the wall with 16 positions of measurements each and separated from each other by 1/2 pitch provide a good picture of the inlet flow and inlet boundary layer parameters.

The downstream station measuring plane is covered by 13 to 15 spanwise traverses, each containing 35 measuring points (every 2.5mm in the pitchwise direction).

A summary of tests parameters for the nine overall tests (3 aspect ratios and 3 downstream measuring planes) is given in Table 1.

2.4.2 Measurements uncertainties

The uncertainty of a variable R is defined herein in the following way : if a variable R is a function of x_i ($i=1,k$) variables, then the uncertainty of R , U_R , is given by

$$U_R^2 = \sum_{i=1}^k \left(\frac{\partial R}{\partial x_i} \cdot U_{x_i} \right)^2$$

In Ref. [2], Salvage made a detailed study of measurement uncertainty related to secondary flow investigations. In this section, Salvage results are briefly summarized and the uncertainties associated with the present tests are derived.

2.4.2.1 Flow angle uncertainty

An important contribution to flow angle uncertainty is the uncertainty of setting the probe in a well defined reference direction. This is estimated to be $\pm .4^\circ$.

Random errors due to measurements system noise and fluctuating flow in the tunnel account for approximately $\pm .2^\circ$ uncertainty.

Pitchwise velocity gradients may severely affect the local measurements of flow angle, but pitchwise averaged values of β are not directly affected as the blade wake is nearly symmetrical.

The total uncertainty estimation is then $\pm .5^\circ$ for pitchwise averaged values.

2.4.2.2 Dynamic head uncertainty

The true dynamic head may be written in the form :

$$q_{\text{true}} = a + m \frac{q_p}{1 + C_{q(\beta_p)}}$$

The uncertainty of q_{true} is then given approximately by :

$$U_{q_{true}}^2 = U_a^2 + \left[\frac{m}{1 + C_q(\beta_p)} U_{qp} \right]^2 + \left[\frac{mq_p}{(1 + C_q)^2} U_{C_q} \right]^2 + \left[\frac{mq_p}{(1 + C_q)^2} \cdot \frac{\partial C_q}{\partial \beta} \cdot U_{\beta p} \right]^2$$

choosing typical average values :

$$\begin{aligned} C_q &= .08 \\ m &= 2 \\ q_p &= 30 \text{ mm H}_2\text{O} \\ \partial C_q / \partial \beta &= .02/\text{degree} \end{aligned}$$

and with

$$\begin{aligned} U_a &= .5 \text{ mm H}_2\text{O} \\ U_{qp} &= .3 \text{ mm H}_2\text{O} \\ U_{\beta} &= .5^\circ \\ U_{C_q}^p &= .01 \end{aligned}$$

The uncertainty of q_{true} is estimated to be $\pm 1 \text{ mm H}_2\text{O}$.

2.4.2.3 Total pressure uncertainty

The total pressure sensed by the Kiel probe used at the downstream station is the true total pressure within the uncertainty of the measurement system and tunnel driving pressure fluctuation over a wide range of β_p ($\pm 25^\circ$). Those fluctuations being estimated to .3 mm H₂O, the total pressure uncertainty is .3 mm H₂O.

The same conclusion applies to the inlet probe because of the very small difference between the probe setting angle and the inlet flow direction (Max. $\pm 3^\circ$). The inlet total pressure

uncertainty is estimated to .2 mm H₂O.

Additional uncertainties are due to displacement effects occurring in wakes and end wall boundary layer but it has been shown in Ref. [2] that those effects on integrated values are negligible.

2.4.2.4 Loss coefficient uncertainty

The loss coefficient ω is defined as

$$\bar{\omega} = \frac{\bar{p}_{01} - \bar{p}_{02}}{q_{\text{ref}}}$$

$$q_{\text{ref}} = (\bar{p}_{01} - \bar{p}_2)_{\text{MS}}$$

$$U_w^2 = \left(\frac{U_{p01}}{q_{\text{ref}}} \right)^2 - \left(\frac{U_{p02}}{q_{\text{ref}}} \right)^2 + \left(\frac{\omega}{q_{\text{ref}}} \cdot U_{q_{\text{ref}}} \right)^2$$

with

$$U_{p01} = .2 \text{ mm H}_2\text{O}$$

$$U_{p02} = .3 \text{ mm H}_2\text{O}$$

$$U_{q_{\text{ref}}} = .4 \text{ mm H}_2\text{O}$$

$$q_{\text{ref}} = 70 \text{ mm H}_2\text{O}$$

we obtain

$$U_w = \pm .006$$

2.4.2.5 Summary

VARIABLE	UNCERTAINTY
β	.5°
q	1 mm H ₂ O
P ₀	.3 mm H ₂ O
ω	.006

2.4.3 Discussion of test results

2.4.3.1 General flow pattern

A typical test result is presented in Figs 5 to 8. In Fig.5, the pitchwise averaged, mass averaged loss coefficient ω is plotted against the blade height. ($2Y/H=0$ corresponds to the wall, $2Y/H=1$ to mid-span). When considering the loss evolution from wall to mid-span, it appears that, after a region of high losses near the wall (due to end wall boundary layer), there is a decrease followed by a peak at approximately $2Y/H=.30$; that peak corresponds to the zone of high losses localized in the end wall-blade suction side corner, which can be seen on the contour plot of Fig.8, and which is associated with the corner vortex (see Appendix B for a description of secondary flow phenomena in cascades). It is interesting to note that, after the minimum of loss coefficient succeeding to the corner vortex peak, losses are slightly rising till mid-span. This is due either - to the transportation of low energy material from end wall or corner region to mid span by means of the passage vortex, or - to a thickening of the blade suction boundary layer near mid span due to the spanwise component of velocity resulting from secondary flows.

Fig. 6 presents the outlet distribution of $\overline{\Delta\beta_2} = \overline{\beta_{2MS}} - \overline{\beta_2}(y)$ against the blade height, $\Delta\beta_2 > 0$ indicating an overturning of the flow. This is seen to be the case near the

wall. This region is followed by an underturning zone, closer to mid-span. This outlet flow angle pattern is consistent with the passage vortex model developed in Appendix B.

The spanwise distribution of tangential velocity $\overline{V_z}/V_{MS}$ corresponding to the outlet flow angle distribution of Fig.6 is shown in Fig.7.

2.4.3.2 Evolution of cascade flow characteristics with increasing downstream distance

From Fig. 9, it can be seen that the increase of losses with increasing downstream distance is much more important between stations 1 and 2 (1/3 and 2/3 of a chord from trailing edge in the streamwise direction, respectively) than between stations 2 and 3 (1 chord in the streamwise direction). This is in agreement with the statement of Wolf (Ref.4) that global losses increase between the trailing edge plane and a plane located approximately at 1 chord of it in the streamwise direction, and remains constant further downstream. This increase in losses is attributed to the mixing losses, end wall boundary layer thickening and secondary vortices decay. It seems that most of the cascade secondary flow data available in the literature were obtained from measurements made at 1 to 1,5 chord in the streamwise direction, downstream of the cascade and represent a quasiasymptotic state, and not what a next row of blade would "see".

Figs 10 to 12 illustrate the influence of downstream station position on the spanwise distribution of losses and outlet angle.

From those figures, we can conclude that with increasing distance from the cascade trailing edge :

- losses near the wall increase
- the peak losses associated with the corner vortex are shifted towards the mid span
- mid-span losses show a definite trend to increase
- the minimum turning point is shifted towards the mid-span and its magnitude is reduced

A reliable model for secondary flows should allow to describe those effects. In particular, we can see from Fig. 11b a, d 12b that a shift of minimum turning point towards mid span occurs between the measuring plane located at $1/3$ and 1 chord downstream of the cascade. This should not occur if secondary flows were only a small perturbation of the main flow, and indicates that there is a need to take into account the effect of secondary flows upon the main one.

2.4.3.3 Influence of aspect ratio

The influence of aspect ratio on global losses

$$\epsilon_M = \frac{\overline{P_{01MS}} - \overline{P_{02M}}}{(\overline{P_{01}} - \overline{P_2})_{MS}}$$

and the spanwise loss distribution is illustrated in Fig. 13 and Fig. 14-16. It shows the usual rapid increase in loss with decreasing aspect ratio; the integrated losses occurring at an aspect ratio of .42 are 1.3 times those occurring at the aspect ratio of .98 (measured at station 3; $DX/C=1$).

The measured losses at station $DX/C=1$ were compared with those predicted by three correlations, namely Soderberg [5], Craig and Cox [6] and Baljé-Binsley [7]. The results are presented in Fig. 17 and are summarized in the following table :

AR	$\omega_{\text{Soderberg}}$	$\omega_{\text{Baljé-Binsley}}$	$\omega_{\text{Craig-Cox}}$	$\omega_{\text{M}}^{\text{exp.}}$	$\omega_{\text{A}}^{\text{exp.}}$
.98	.096	.049	.089	.059	.085
.67	.122	.067	.107	.068	.106
.42	.168	.0101	.139	.081	.140

It can be seen that the area averaged measured losses fit surprisingly well the Craig and Cox correlation. Soderberg's correlation is on the upper side, but indicates the same trend. Baljé-Binsley's correlation is on the lower side.

However, it is very important to note that the variations in aspect ratio were achieved by reducing the blade height, and that in doing this, two other non-dimensional parameters of importance in the study of secondary flows are changed as well : the pitch to blade height ratio s/h and the inlet boundary layer thickness to blade height ratio δ_1/h .

a) effect of parameter s/h *

Simple secondary flow theory assumes that all cascades which produce the same mean deflection θ also produce the same secondary vorticity. The magnitude of the secondary velocities induced by that secondary vorticity is then dependend on $\frac{s}{h} \cdot \cos \beta_2$ and on δ_1/h . Since it seems to be a reasonable assumption that that part of secondary losses associated with the secondary flows, often called the "interaction losses" depend on the magnitude of secondary velocities, it is interesting to examin more closely

* The ratio s/h is often used in the literature under the form

$$\frac{1}{\sigma \cdot \text{AR}}$$

the evolution of those velocities, represented by the kinetic energy of secondary flow KE_s . In Ref. [8], Belik computed the secondary flow kinetic energy resulting from a particular class of fully-developed boundary layers. His results are sketched in Fig. 18. Although fully developed boundary layers are not of general interest in turbomachinery, the form which the curves exhibit are . We can observe, in particular, that for a given δ_1^*/h , the kinetic energy of secondary flows does increase with increasing s/h . (note that instead of s/h , the equivalent expression $\frac{1}{\sigma \cdot h/c}$ has been used in Fig. 18).

In order to check the general trend indicated by Belik, theoretical calculations were performed with the computer program described in Appendix C. It was found that for our particular cascade, a variation of the ratio s/h from .87 to 2.2 results in an increase of ω_{kin} from .0044 to .0054 .

b) Effect of parameter δ_1/h

From an inviscid point of view, the results of Belik show an increase in secondary kinetic energy with an increase in δ_1^*/h . This trend is again confirmed by our calculation ($\omega_{kinetic} = .0044$ for $\delta_1 = .08$, rising to $\omega_{kinetic} = .0055$ for $\delta_1/h = .16$).

Considering the existing correlations, two of them, those of Dunham-Came and Baljé - Binsley, take explicitly into account the effect of inlet boundary layer. They state (see Fig. 19) that secondary losses are increasing with increasing δ_1 until an asymptotic stage is reached ($\delta_1/h \approx 1/3$). But Salvage pointed out in his thesis that, for compressor cascades, the dependance of mass averaged secondary losses on δ_1^* comes from the fact that in the balance of total pressure across the blading, the deficit of inlet total pressure due to the inlet boundary layer is considered as part of the blading loss. So he proposed

to use the loss coefficient $\omega'_M = \frac{\overline{p_{01M}} - \overline{p_{02M}}}{q_{ref}}$ instead of $\omega_M = \frac{\overline{p_{01MS}} - \overline{p_{02M}}}{q_{ref}}$.

Following [10] we can write :

$$\omega'_M = \omega_M - \frac{2\delta_1^*}{h - 2\delta_1^*} \cdot \frac{H_{32}}{H_{12}} \cdot \left(\frac{\cos\beta_2}{\cos\beta_1} \right)^2 = \omega_M - \omega_1$$

A least mean square fitting of the inlet boundary layer data points by a Lefoll profile gives $\delta_1^* = 1.098$ mm and $H_{32}/H_{12} = 1.19$, leading to the following values of ω'_M :

AR	ω_1	ω'_M
.98	.003	.056
.67	.005	.063
.42	.008	.073

The correction due to inlet boundary layer is seen to be of little importance in our case, and certainly not enough to explain the effect reported by Baljé in Ref. [9] and based on the results of Wolf [4] (see Fig.19). This is due to the small value taken by the ratio $(\cos\beta_2/\cos\beta_1)^2 = .14$ in the present case, and one must notice that this correction due to inlet boundary layer would be much more important for an impulse blading, where the factor $(\cos\beta_2/\cos\beta_1)^2$ is equal to 1.

Salvage [10] also pointed out that, for a given cascade, there exists a value of δ_1/h leading to the beginning of "low aspect ratio effects", that can be defined as disturbance of the mid span flow by secondary flows, especially by the corner

vortices. Due to Salvage mid-span losses start to rise at the same rate as secondary losses as soon as the critical ratio δ_1/h is reached. This author found that, for his compressor cascade tests, this limit value of δ_1/h is given by

$$\frac{\delta_1}{h} = 0.5 - 0.496 \theta \frac{c}{h}$$

If we compare the mid-span losses to the global losses for our measurements (see table 2), we find that mid span losses have the same evolution than global losses, indicating the occurrence of "low aspect ratio effects". This is obvious in the tests performed with the smallest aspect ratio ($AR = .42$), where the peak losses do occur at mid span, as it can be seen on the contour plot of Fig.20.

Finally, a last remark must be done about the effect of a blade height reduction on end-wall losses. Considering a pseudo-tri-dimensional end wall boundary layer characterized at the exit plane by its integral parameters δ_x^* , θ_x and θ_z , the area averaged end wall loss factor is given by

$$\bar{\omega}_{EW,A} = \frac{2}{h} (\delta_x^* + \theta_x - \theta_z),$$

leading to our hyperbolic dependence of end wall losses on the blade height, as exhibited by the classical secondary losses correlations. However, it seems more questionable to assume that the same effect will be obtained by keeping the blade height constant and varying the blade chord in order to obtain the same aspect ratio variation. This emphasises the fact that great care must be taken when forming non-dimensional quantities.

In conclusion, we can say that a reduction of blade height, keeping all the other parameters constant, leads to an increase of losses roughly proportionnal to $1/h$ even if we neglect

any aspect ratio effect (i.e. if we suppose that the end-wall boundary layer development is independent of the blade height). Moreover, a reduction of the blade height acts on the ratios s/h and δ_1/h in a sense favourable to higher losses. It would however, be dangerous to interpret our tests in terms of non-dimensional quantities, since the effect of an increase of c , s or δ_1 was not investigated.

2.5 Comparison with a simplified theoretical model

2.5.1 Flow angle distribution

The flow angle distribution was computed, using the simplified secondary flow model for the pitchwise secondary velocities v_z described in Appendix C. For each aspect ratio, the measured $\Delta\beta_2 (= \beta_{2MS} - \beta_2(y))$ distribution at the station $DX/C = 1/3$ is compared with the one calculated* :

- using Horlock's formula for V'_z
- using a finite element program resolving the equation $\Delta\psi = \xi$
(see Appendix C)

The two methods are seen (Fig.21) to give very similar results, the only differences occurring between the wall and the minimum turning point. This last point is seen to be predicted to occur at a distance from the wall equal to the inlet boundary layer thickness. This is a general trend observed by many authors

* "The station closest to the trailing edge plane was chosen because of the increasing influence of secondary flows upon the primary flow with increasing downstream distance"

(see [10] and [12] for example).

The agreement with experience is only qualitative, the magnitude of secondary flows being overestimated and the predicted minimum turning point being too close to the wall. A more refined model will be necessary to obtain quantitative results, in particular, it is necessary to take into account the effect of viscosity, Bernoulli surface rotation and spanwise displacement effect [13],[14].

2.5.2 Profile losses

Profile losses can be estimated as soon as the trailing edge geometry and the blade boundary layers integral parameters at trailing edge are known. A boundary layer calculation based on the Martensen velocity distribution leads to the following parameters :

$$\delta_{ss}^* = .401 \text{ mm}$$

$$\delta_{ps}^* = .106 \text{ mm}$$

$$\theta_{ss} = .238 \text{ mm}$$

$$\theta_{ps} = .070 \text{ mm}$$

Using the expression from Appendix C to approximate the mass averaged loss at 1 chord of the blade trailing edge in streamwise direction (momentum flow averaging = mass flow averaging = area averaging), we obtain $\bar{\omega}_{prof} = .0242$, which is very close to the profile losses derived from the Baljé-Binsley correlation ($\bar{\omega}_{prof} = .0236$).

2.5.3 End wall losses

Salvage [10] proposed to compute the end-wall losses by assuming that the streamwise component of the end-wall boundary layer is well represented by a 2-D boundary layer submitted to the average cross-channel pressure gradient. Together with the cross flow integral parameters that can be derived from

Horlock's expression for secondary velocities, this allows then an estimation of the end wall losses to be made (see Appendix C).

The numerical results of this calculation in our case are summarized as follows :

$$\begin{aligned} \delta_x^x &= .650 & \theta_{z_2} &= .195 \quad (\text{AR} = .42) \\ \theta_{x_2} &= .450 & \theta_{z_2} &= .193 \quad (\text{AR} = .67 \text{ and } .98) \end{aligned}$$

leading to the following area averaged losses :

AR	$\bar{\omega}_{EW,A}$	$\bar{\omega}_A$	$\bar{\omega}_{Aexp.}$
.42	.036	.060	.140
.67	.023	.047	.106
.98	.016	.040	.085

These values are well under the measured ones indicating the failure of the model in our case, where high flow acceleration and aspect ratio effects do occur.

2.6 Channel flow

The development of secondary flows within the blade channel was studied by means of flow visualizations, blade pressure distributions and detailed boundary layer traverses.

2.6.1 Flow visualizations

Blade surface and wall flow patterns are obtained by oil flow visualizations and ink traces. While in the case of oil flow visualizations the mixture of medium grade oil and titanium dioxide is uniformly applied to the surfaces, the ink is either

injected through discrete wall tapings or it is applied in discrete dots to the endwall and blade surfaces.

A photograph of a blade suction side flow visualization obtained with the ink trace technique is shown in Fig.22. It is apparent from this figure that

a) a bi-dimensional separation does occur on the blade suction surface at a distance of approximately 20% of the chord length from the trailing edge. This separation is likely to be laminar, a boundary layer calculation indicating that the boundary layer remains laminar over the whole suction surface. From oil film visualizations and from the loss contour plots (compare Figs 35 and 40), it appears that the separation line is moving upstream with decreasing blade height. This is attributed to the fact that the boundary layer convergence on the blade suction side is more severe for the small blade height.

b) a tri-dimensional separation does occur near the end wall-blade suction side corner; the limiting streamlines leave the blade surface at the separation line ss' (See Ref. [18] for 3-dimensional separation analysis).

The flow over the pressure side was found to be two-dimensional over most of the surface.

End wall flow visualisations obtained during preliminary^x investigations at VKI, through the use of the oil film technique indicated the existence of a "separation vortex" (or horseshoe vortex, or stagnation vortex), that wrapped around the blade leading edge (Fig.23). Such a vortex does occur when a boundary layer flow is forced to pass around a blunt obstacle. A study of this phenomena can be found in Belik [19], in the case of a boundary layer flow around a circular cylinder. In the case of a turbine cascade, this "stagnation vortex" is submitted

^x The variation of the aspect ratio was initially done with sliding intermediate sidewalls. For the final tests 1 full set of blades was manufactured for each aspect ratio.

to a transverse pressure gradient, and will no more be symmetric; the vortex leg formed along the suction side of the blade is rapidly pressed down on the blade surface, while the pressure side leg crosses the blade passage and finally hits the suction side of the next blade. Similar trends are observed by Stanbrook [20] in his experimental study of the horseshoe vortices that develop at wing-body junctions. Fig.24 presents Stanbrooks interpretation of the flow phenomenon.

One question to be asked at this stage is, does the stagnation vortex have a determining influence on the rest of the flow field ? It will be tried to answer this, at least partially, in the section 2.6.3 and 2.7.2.

2.6.2 Blade velocity distributions

The blade velocity distribution is computed by use of the following formula :

$$\frac{V}{V_1} = \sqrt{\frac{(\overline{p_{01}} - p_A) + 10 \rho_{alc} (l - l_{ref})}{\overline{q_1}}} = \sqrt{F}$$

pressures in mm H₂O

$l - l_{ref}$ in cm of alcool

The uncertainty of V/V_1 is then approximately

$$U^2_{V/V_1} = \frac{1}{4q_1 F} \left[U^2_{(\overline{p_{01}} - p_A)} + 100 \rho_{alc}^2 U^2_{(l - l_{ref})} + F^2 \cdot U^2_{q_1} \right]$$

Choosing average values for F and q_1 :

$$F = 4$$

$$q_1 = 10 \text{ mm H}_2\text{O}$$

and with

$$U_{(P_0 - P_A)} = .3 \text{ mm H}_2\text{O}$$

$$U_{(l - l_{ref})} = .05 \text{ cm alcohol}$$

$$U_{q_1} = 1 \text{ mm H}_2\text{O}$$

the uncertainty of $\frac{V}{V_1}$ = amounts to 0.1.

The blade surface velocity distributions at two spanwise positions ($y = 5 \text{ mm}$ from the wall and $y = \text{mid-span}$) are presented in Fig. 25 for the two extreme aspect ratios used in this investigation, together with the potential velocity distribution computed with a program based on the methods of Martensen [11].

It can be seen that there is a good agreement between the predicted and the measured distributions, except on the pressure side, in the vicinity of the blade leading edge, where a laminar separation is likely to occur due to a velocity peak.

There is no sensible effect of spanwise position to be observed in our case, yet such effects have been noticed with more cambered blades [16].

2.6.3 Channel flow measurements

2.6.3.1 Measuring uncertainties

3-hole probe (2-directional probe)

As already mentioned before (Chapter 2.3) the bulk of the measurements is done with the same 3-hole probe (Fig.2a) which is also used for the inlet flow traverses. However, contrary to the inlet flow, the channel flow is characterized by strong pitch-wise velocity gradients as well as by non-negligible span-wise cross flow components. Both add some additional terms to the measuring accuracy which was already evaluated for this probe in Chapter 2.4.2 for the particular condition of a uniform flow far upstream of the cascade :

- The choice of a non-balancing mode for the probe in a non-uniform flow field requires the use of calibration curves for the correct derivation of the total pressure, the flow angle and the dynamic pressure.
- Due to the distance between the directional tubes of the probe, flow parameters are derived from measurements taken on stream surfaces with different flow properties. The flow parameter, which is most affected by the pitch wise velocity gradients is the local flow angle. Contrary to downstream wake traverses, pitch-wise averaging does not compensate these errors.
- The 3-hole probe does not take into account spanwise cross flow components.

Choosing average values for a typical traverse plane located about $1/2$ axial chord from the leading edge inside the blade passage, one obtains the following estimation for the measuring uncertainty :

$$\begin{aligned}U_{\beta} &= 1^{\circ} \\U_q &= 1.2 \text{ mm H}_2\text{O} \\U_{po} &= 0.5 \text{ mm H}_2\text{O} \\U_{\omega} &= 0.008\end{aligned}$$

where U_x is the uncertainty of the variable X.

5-hole probe (3-directional probe)

The measuring uncertainties associated with the use of the 5-hole probe (Fig.2.b) can be summarized as follows :

$$\begin{aligned}U_{\beta} &= 1^{\circ} \\U_{\gamma} &= 1^{\circ} \\U_q &= 1 \text{ mm H}_2\text{O} \\U_{po} &= 0.5 \text{ mm H}_2\text{O} \\U_{\omega} &= 0.008\end{aligned}$$

Hot wire anemometer

A VKI hot wire constant temperature linearized anemometer was used to perform some endwall boundary layer traverses. The uncertainty of the ratio V/V_{MS} is 0.007.

2.6.3.2 Experimental procedure

The channel flow measurements required certain modifications of the test section. One of the side walls was equipped with rectangular steel plate inserts. These plates are designed with slots parallel to the cascade front and positioned at various axial distances. The seven plates allow to make traverses in 14 different axial stations. An example of a plate is shown in Fig.26a along with some of the other pieces required. These additional pieces include the probe carriage holder and T-shaped slot-fillers which allow to place the probe shaft anywhere within a 300 mm tangential range with an accuracy of ± 0.5 mm. A photograph with the probe carriage mounted on the wind

tunnel is presented in Fig. 26b. The probe carriage allowed translation of the probe perpendicular to the end wall plate and rotation of the probe about its shaft.

Eight measuring planes were selected for the present investigation; they are defined in Fig.27. In each plane, eleven equally spaced spanwise traverses were performed. In each traverse, 14 to 18 (depending on the aspect ratio) measuring points were taken, from .5 mm from the wall to mid-span.

2.6.3.3 The integrated mass averaged loss coefficient $\bar{\omega}_M$

Fig. 28 presents the growth through the turbine passage of the mass averaged loss coefficient integrated over the whole measuring plane, $\bar{\omega}_M$.

In Fig.28a, the loss coefficient $\bar{\omega}_M$ is plotted for the three aspect ratios with respect to the axial distance measured from the trailing edge plane. Three regions can be distinguished. The first one, extending from the inlet measuring plane till about -50% of the axial chord from the trailing edge, shows only a slight increase of loss. The second region extends from -50% of the axial chord up to the trailing edge, and reveals a steeper increase of loss. This region is separated from the third one, the downstream region, by a jump of losses, due to the sudden area expansion at the trailing edge and due to wake mixing.

Fig.28b presents the growth of a reduced loss coefficient $\bar{\omega}_M \times (\frac{AR}{.42})$. This corresponds to referring the loss coefficient to the smallest blade height. The fact that these reduced coefficients collect on a single curve (within the measurements uncertainties) indicates that the possible interference effects due to the small aspect ratio have a negligible effect on the aerodynamic loss inside the turbine passage, at least for the blade loading

distribution and inlet boundary layer thickness used in the present investigation. It should, however, be insisted on the fact that contrary to the integrated loss coefficient, the spanwise loss distribution is quite different between the smallest and highest aspect ratio.

2.6.3.4 Loss coefficient and flow angle distribution

The results of the detailed passage survey performed with the 3-holes probe are shown in Fig.29 to 45. In each of these figures, Fig.a presents the pitchwise averaged-mass averaged loss coefficient plotted against the blade height, Fig. b presents the distribution of $\overline{\Delta\beta_2}(y) = \bar{\beta}_{2MS} - \bar{\beta}_2(y)$ against the blade height, and Fig. C is a loss coefficient contour plot.

A detailed discussion of each of those tests will not be given here; we just want to point out what appears to us as being the most characteristic features of the flow patterns.

Looking at the results associated with the largest aspect ratio (AR = .98), we can say that :

- the end wall boundary layer in plane 1 (situated at a distance equal to 40% of the axial chord upstream of the blade leading edge) is still nearly collateral. The boundary layer thickness corresponding to the 1% iso-loss line is approximately 10 mm.
- the end wall boundary layer thickness near the pressure side is decreasing when proceeding downstream through the turbine passage.
- the corner losses remain localised in the end wall-suction surface corner till very near the cascade outlet (see Fig.35, test NP7, DA/CA = -.14).

- No marked influence from the horseshoe vortex on the flow pattern can be seen, except in plane 2 (leading edge plane) where some deformation of the iso-losses lines does appear near the suction side, indicating a stream line shift.

With respect to the results associated with the smallest aspect ratio ($AR = .42$), the following two features are of interest :

- the corner losses seem to develop somewhat earlier in the blade passage (compare Fig.35c with Fig.40c), but it is likely that this has to be related to the fact that the laminar separation on the blade suction side appears earlier too.

The displacement of the region of maximum losses towards mid-span, which was the main feature observed in the overall performance tests, becomes only apparent in the rear portion of the blade passage ($\approx 30\%$ of the axial chord upstream of TE).

2.6.3.5 3-directional probe measurements

Test NP7 ($AR = 98$, plane N°7, $.14 \times$ axial chord from TE) was repeated using the 5-hole probe in Fig.2b. Figs 46a and 46b present the comparison between the loss coefficient and the flow angle distribution obtained with

- a) 3-hole probe (2-directional probes)
- b) 5-hole probe (3-directional probe).

Bearing in mind the measurement uncertainties discussed earlier and the fact that the 3-holes probe is a bi-dimensional probe used in a 3-D flow field, the agreement between the two tests is satisfactory. Fig. 46c shows the loss coefficient-contour plot, which is again comparable to the isoloss plot obtained with the 3-hole probe. Fig.47 is a secondary velocity chart obtained

by vectorially subtracting the pitch wise mid-span velocity component from the measured in-plane velocity vector at the same spanwise traverse. The most striking feature is that the center of the main vortex motion is located at about mid-pitch, and is not shifted towards the blade suction side as one first might suppose. Looking at the isolosses plot, we see that no loss production is associated with the core of this vortex, but merely a simple deformation of the isolosses lines, which can be looked at as a "transportation" effect.

Whether the location and strength of this "passage vortex" is influenced by the stagnation vortex cannot be answered at this stage of the study.

2.6.3.6 Hot-wire boundary layer traverses

Four spanwise traverses were made with a VKI hot-wire anemometer to measure end wall boundary layer velocity profiles. These traverses extended from mid-span to .3mm from the wall; their locations are given in Fig.27. The measured velocity profiles, non-dimensionalised by the mid-span velocity, are given in Fig.48a. All three traverses accomplished inside of the blade passage have in common this striking feature, that velocity remains constant over the whole range of measurements. However, if we compare, for example, the velocity profile of the hot wire traverse 1 to the total pressure profile of the same traverse (Fig.48b), we see they are incompatible with the boundary layer theory assumption of a constant static pressure through the layer.

A two-dimensional boundary layer velocity profile seems thus unable to describe the end-wall flow pattern.

2.7. Leading edge flow field

2.7.1. Test set-up and experimental procedure

This part of the investigation was performed using the blade with the hollow movable leading edge which was already mentioned in chapter 2.3. (See also Fig.4). Of course, the zone which can be explored in this way is rather limited : up to 15mm ahead of the leading edge and 10 mm across the leading edge (pitch wise direction).

Photographs showing the leading edge instrumented with the 5 hole probe are shown in Fig.49a. Fig.49b presents a close up view of the probe sticking out of the nose.

New wind tunnel end plates were fabricated, allowing for the passage of the movable leading edge. Any leakage was prevented by using a rubber joint between the blade nose and the endwall plates. A photograph of the modified wind tunnel is given in Fig.50.

Twelve spanwise traverses were performed, the location of which is given in Fig.27.

2.7.2. Test results

The variations of β and γ along the blade height, for each traverse, are represented in Fig.51 to 54. β is the flow angle from axial direction, in a plane parallel to the end walls. The angle β is defined as negative if the circumferential component of the inlet flow points into the same direction as the circumferential component of the outlet flow. The angle γ presents the flow angle with respect to the end wall. $\gamma > 0$ corresponds to a flow component directed from mid-span towards the end wall.

Looking at Fig.51 to 54, we can see that at proximity of the wall :

- the flow is directed towards the end-wall ($\gamma > 0$)
- in most cases, the angle β near the wall has the same sign but a greater absolute value than the angle β at mid-span at the same spanwise traverse. The flow near the end-wall is thus "pushed away" from the leading edge. This flow pattern corresponds to the classical image of the stagnation vortex as a roll-up of the boundary layer around the blade nose.

From the measured data points, the secondary velocities in a plane located 5mm in front of the leading edge were computed and the corresponding chart is presented in Fig.55.

As far as the influence zone of the leading edge vortex is concerned, it is noted that :

- except for the traverses closest to the leading edge, the measured angle variations are always less than 5°
- the spanwise extension of the vortex influenced region is approximately 2 inlet boundary layer thickness from the wall (choosing $\gamma - \gamma_{ms} = 1^\circ$ as a criterium). Its upstream extension, based on the endwall flow visualizations, is approximately 2 times the blade leading edge radius.

Moreover, if we remember that the blade passage tests did not indicate any serious loss penalty associated with the horse shoe vortex, we could conclude that this vortex does not have a determining influence on the flow pattern.

At this point, however, two remarks must be done :

- 1) Due to the blade-to-blade pressure gradient, the separation vortex leg forming along the pressure surface crosses the

blade passage and ends on the suction surface of the following blade. The authors of Ref. {16} suggest that the whole inlet boundary layer is involved in this vortex motion, and that a new boundary layer begins after the separation line. This would explain the extreme thinness of the passage end-wall boundary layer obtained both in their tests and in those of Senoo {21}. Sjolander {22} proposes a similar model for the influence of the horse-shoe **vortex**, but suggests that only the inner part of the boundary layer could be involved in the vortex motion, the outer part reattaching downstream of the separation line.

- 2) Many factors do influence the location, and hence probably the strength of the separation. Belik {19} showed, in the case of a symmetrical flow field about a cylinder, that the separation location depends on the state of the boundary layer (laminar or turbulent), the Reynolds number based on the boundary layer thickness and on the cylinder diameter. Langston and al {16} showed in addition that the pressure distribution has an important influence too, in the case of an asymmetrical flow field.

Comparing now the cascades tested by Langston and al and by Senoo, we see that Langston's cascade has a very strong transverse pressure gradient at the blade channel inlet, while Senoo's cascade acts merely like a straight nozzle at the beginning of the passage, but it has a very large blade leading edge radius ($R/s \approx .20$). So, while being of very different conceptions, those two blades have both a characteristic feature suspected to lead to a severe three-dimensional leading edge separation (large transverse pressure gradient - large leading edge radius), and the mechanism proposed by Langston and al would then be effective, leading to a very thin end-wall viscous layer.

In our cascade, in which the transverse pressure gradient is moderate (compared to Langston's cascade) and the leading edge radius is relatively small compared to Senno's

cascade), the separation vortex is likely to be much weaker, and one might assume that the inlet boundary layer is only partially involved in the leading edge vortex. This would explain the fact that, while finding a reduction of end-wall viscous losses inside of the passage, near the pressure surface, no drastic reduction is found. On the other hand, we might recall here that the peculiar shapes of the end-wall velocity profiles lead us to the conclusion that the viscous layer developing on the passage end-wall seems not to be a conventional boundary layer : this is a possible effect of the three-dimensional separation (the "horse-shoe vortex") to which the inlet boundary layer is submitted.

So, from the presently available data, we can conclude that :

- A separation vortex (also called "horse-shoe vortex", "stagnation vortex", saddle point separation" following various authors) does occur about the blade leading edge, due to the rolling up of the inlet boundary layer.
- No serious loss penalty seems to be associated to it.
- In our test case, this vortex is of limited extension and strength.
- The main effect of the separation vortex is to remove the inlet wall boundary layer from the end-wall, at least partially. This mechanism is greatly influenced by the blade-to-blade pressure gradient and the leading edge radius. In our test case, this effect is of limited importance; however, some features of the flow pattern are likely to be dependent on the separation vortex :
 - the reduction of end-wall viscous losses in the blade passage, near the pressure surface.
 - the structure of the end-wall viscous layer.

2.8 CONCLUSIONS - LOW SPEED TESTS

So far we can draw the following conclusions :

Leading edge flow

A separation vortex does develop about the blade leading edge, due to the rolling up of the inlet boundary layer. No serious loss penalty seems to be associated to it, and our tests indicated that it is of limited extension and strength. This separation vortex seems, however, to play a significant role in removing the end-wall inlet boundary layer, at least partially, and in doing this, to control the subsequent evolution of the end-wall viscous layer in the turbine passage. While in our tests the effect of the separation vortex is rather limited, a drastic influence was found by other investigators. This suggests that the cascade geometry is of determining importance on the separation vortex mechanism. Two parameters at least are of interest : the blade to blade pressure gradient and the leading edge radius.

Channel flow

- The end wall viscous layer near the pressure side is thinner than the endwall boundary layer upstream of the cascade. This is likely to be an effect of the separation vortex. End wall "boundary layer" velocity traverses indicated that the resultant velocity profile is nearly constant till very near of the wall (.3mm). Coupled with the fact that the total pressure profile at the same position is not constant, it implies that a 2-D boundary velocity profile is unable to represent the local end wall flow conditions.
- The corner losses remain localised in the end wall-suction surface corner till very near of the cascade outlet ($\pm .15$ axial chord upstream of trailing edge).

- From tests results obtained in a plane located at .14 axial chord upstream of the trailing edge, it appears that the main secondary vortex motion does not coincide with the region of corner losses. No noticeable loss production is associated with this vortex, but merely a skewing of the flow field.

- The integrated mass averaged aerodynamic losses are seen to be slightly increasing, up to approximately 50% of the axial chord upstream of the blade TE. From that point, losses are increasing at a higher rate.

No measurable interference effect is noticed when decreasing the aspect ratio from .98 to .42.

Outlet flow field - Overall performance

- Measured losses increase with the distance between the outlet measuring plane and the blade trailing edge plane until an asymptotic state is reached (at ≈ 1 chord in the streamwise direction). The form of the spanwise distribution is altered too : the losses near the wall increase and the peak losses are shifted towards mid-span.

The minimum turning point is shifted towards mid-span and its magnitude is reduced.

- Total losses are rapidly increasing with decreasing blade height. Area averaged losses are found to be well predicted by the Craig and Cox correlation.

It has been shown that a decrease of blade height leads to an increase of area averaged losses roughly proportional to $1/h$, and that it acts on the ratios s/h and δ_1/h in a sense favourable for higher losses.

It would, however, be dangerous to interpret our tests in terms of non-dimensional quantities, since the effect of an increase of c , s and δ was not investigated.

- A simple small shear-small disturbance type secondary flow model is seen to produce only qualitative agreement with experiments. Quantitative agreement would require at least the allowance for large disturbances.

A simple model for viscous losses, where the streamwise component of the end-wall boundary layer is represented by a 2-D boundary layer submitted to the average mass-channel pressure gradient, fails to produce realistic results.

3. HIGH SPEED TESTS

3.1 Test facility and instrumentation

3.1.1 Test facility

The test facility (Figs 56) used for the investigation of various transonic turbine cascades is the VKI high speed cascade tunnel C-2. This tunnel is of the blow down type (exhaust to atmosphere) and is supplied with dry air from high pressure reservoirs. 120 m³ are available at 40 atm. at the inlet to the settling chamber. The throttling system consists of a general shut off valve, a pneumatic regulated quarter revolution valve and a manually controlled needle throttle valve. This system allows a rapid pressure rise and fine regulation of the required settling chamber pressure.

The air enters the settling chamber through a backwards bent, perforated pipe to suppress the inlet swirl. The inlet to the nozzle has a contoured upper part which is interchangeable for subsonic and supersonic cascade inlet Mach numbers. The lower nozzle block is straight. Both nozzle blocks are adjustable.

The test section outlet is formed by a diffuser equipped with a backpressure valve. The outlet can be rotated between a horizontal and a vertical position.

3.1.2 Test section

The test section is formed by 2 Perspex side walls (19 mm thick) in which the blades are fixed and by the wooden cascade section end walls. The end passages of the cascade are full passages. The boundaries are either the suction side or the pressure side of a normal blade. Behind the trailing edge plane

a sudden area enlargement in pitchwise direction is foreseen. The dimensions of the test section are 50 mm (\approx blade height) x 200 mm. A change of the incidence angle is obtained by rotating the cascade.

3.1.3 Tunnel and test section instrumentation

The settling chamber pressure is measured with a mercury filled U-tube manometer. The pressure can be kept constant within ± 1 mm Hg. The static pressure on the blades and the wall pressure distributions in pitchwise direction at the cascade inlet and outlet are measured with a mercury multimanometer. A blocking device allows the readings to be made after each blow down.

Midspan traverses are performed in the inlet and outlet plane of the cascade at axial distances of about 60% of the chord at the inlet and 40% of the chord at the outlet. (The axial downstream distance of 40% of the chord corresponds to 1 chord length in flow direction). The probes used are a pitot-directional probe for the inlet, and for the outlet a pitot directional probe combined with a single needle static pressure probe (Fig. 57). The probes are displaced tangentially in a fixed axial position by a remote controlled carriage. Strain gauge pressure transducers, with a linearity of better than 0,1% full scale, are used to record on a paper recorder the required flow parameters.

The facility is also equipped with a standard Schlieren system for flow observation in continuous operation and for pictures by using a short duration 15,000 V electric discharge.

3.2 Blade and cascade geometry

The relative small test section of the high speed wind tunnel requires the use of blades with rather small chord length. In the present case the choice of the chord length was dictated by the limited test section height (200 mm) on one side and the

wish to work with a maximum of blade passages on the other side, as the number of blade passages plays an important role in establishing periodic outlet flow conditions in the high subsonic outlet Mach number range. Eight passages are considered to be a suitable compromise. This leaves 25 mm per blade space, which results for a space to chord ratio of $s/c = 0.72$ in a chord length of 35 mm. Hence, with a blade height of 50 mm (\approx test section width) the aspect ratio becomes $h/c = 1.4$. This is considerably higher than the highest aspect ratio in the low speed test ($h/c_{\max} = 0.98$). However, the present test series aims only at the 2-dimensional blade performance at high speed and it is considered that for this purpose a high number of blades is highly desirable.

The final blade and cascade characteristics are summarized below :

blade height	h	50 mm	
chord length	c	35 mm	
blade spacing	s	25.27 mm	
throat	ϕ	10,0 mm	
stagger angle	γ	41.35°	[with respect to axial direction
nominal inlet flow angle	β_1	0°	
number of blades		9	

Due to a manufacturing error the stagger angle for the high speed set up is higher by 1° compared to the low speed tests. This difference has to be accounted for when comparing the low and high speed tests. The effect on the losses can consider being negligible.

3.3 Test conditions

3.3.1 Variation of outlet Mach number and Reynolds number

The outlet Mach number M_2 is varied by a change of the upstream total pressure p_{01} . The relation between p_{01} and M_2 is almost linear. The tests cover an outlet Mach number range from $M_2 = 0.5$ to 0.9 .

A characteristic feature of a blow down type cascade tunnel with exhaust to atmospheric pressure is that the Reynolds number can not be kept constant when the outlet Mach number is varied. In fact the Re-number (based on chord length and outlet velocity) varies in this test series from 400.000 at $M_2 = 0.5$ to 720.000 at $M_2 = 0.9$ (Fig.58). However, in all cases the Re-number is well above the critical Reynolds number of 2 to 3×10^5 which is often quoted in the literature.

3.3.2 Downstream periodicity

The downstream Mach number is derived from side wall static pressure tapings positioned at an axial distance from the trailing edge equal to 0.40% of the chord length (\approx to 1 chord length in streamwise direction), and the total upstream pressure.

Great care is taken to obtain a good outlet periodicity. The quality was judged on the basis of a comparison of the integrated outlet Mach numbers (over 1 pitch) for the three central pitches. The non-periodicity coefficient ϵ , defined as

$$\epsilon = \frac{\bar{M}_2(1 \text{ pitch}) - \bar{M}_2(3 \text{ pitches})}{\bar{M}_2(3 \text{ pitches})}$$

does never exceed a value of $\epsilon = 1$ to 2%.

3.3.3 Flow unsteadiness

The turbulence level measured upstream of the cascade is of the order of $Tu = 0.5\%$ to 1% where

$$Tu = \frac{\overline{u^2}}{U}$$

This turbulence level is of course not at all representative for the turbulence levels existing in real machines. It is possible to increase moderately the turbulence level in cascade tunnels by the use of perforated plates which are placed at some distance upstream of the cascade. However, if the turbulence level is increased in this way beyond 3 to 4%, then the flow loses its isentropic character. It was therefore decided to do the tests at the natural turbulence level of the tunnel.

Besides the above mentioned turbulence, there exists two other types of unsteady flow phenomenon in cascades. The first one is a low frequency unsteadiness of some hundred hertz which has its origin in the free shear layer at the extremities of the cascade. This unsteadiness is particularly strong in the transonic and low supersonic outlet Mach number range, where it produces fairly big variations of the shock positions and outlet flow angles. Preliminary measurements with fast response pressure transducers indicate, however, that the time averaged pressures correspond closely to the pressure recorded with standard low frequency measuring equipment.

The second type of unsteady flow phenomenon is of very high frequency, 10.000 s^{-1} to 30.000 s^{-1} and is linked to the existence of the von Karman vortex streets at the trailing edges of the blades. Again, the maximum unsteadiness occurs in the transonic outlet Mach number range. However, the amplitudes of the flow variations caused by the von Karman vortices are significantly smaller than those of the low frequency unsteadiness.

The effect on the accuracy of the downstream measurements should be negligible.

3.3.4 Stagnation temperature

The stagnation temperature T_{01} measured in the settling chamber is of the order of 0° to 15°C . The variation of T_{01} during 1 test run (a downstream traverse over 3 pitches takes 2 to 3 minutes) stays within 2° to 5°C . The high pressure air is dried such that inspite of the low static temperatures downstream of the cascade, no condensation shocks occur.

3.3.5 Measuring uncertainties

There are two distinct different classes of measuring uncertainties. The first class represents all those uncertainties which imply certain imperfections in the measuring and data recording system like probe calibration errors, probe alignment errors, non-linearity and zero shift due to temperature effects of transducers and recording instruments, reading errors, etc.

The second class of measuring uncertainties is not due to some measuring errors but, due to effective differences in the blade performance from blade to blade. These blade to blade performance variations can be caused by slight differences in blade shape, blade spacing or stagger angle which might influence the point of transition on the blade suction side. Another possible source is to look for in non-periodic outlet flow conditions which have their origin in an incorrect setting of the end walls at the cascade extremities.

In the present case the blade loss variation from blade to blade amounts to 0.3 points. The total error for the blade loss coefficient is about 0.5 points. As far as the outlet angle is concerned the blade to blade variation amounts to 0.2° and the total uncertainty is estimated to 0.5° .

3.4 General flow pattern - flow visualisations

3.4.1 Oil flow visualisations

Surface flow visualisations, using medium grade oil and titan dioxyde powder, are made for an outlet Mach number $M_2 = 0.5$. The photographs in Fig.59 show the flow traces on both the side wall and the blade surfaces. The flow visualisations indicate clearly the main flow pattern i.e. :

- the influence zone of the leading edge vortex
- the flowing of the stream lines from the pressure side to the suction side under the influence of the cross channel gradient
- the interference of the side wall stream lines with the suction side flow (beginning of corner vortex)
- the dividing line on the blade suction side between the blade boundary layer and the side wall boundary layer (see strong white paint trace)
- the slight streamline divergence on the blade pressure side
- the leading edge stagnation point line
- the wake direction on the side walls.

Based on the photographs the influence zone of the secondary losses covers about 15% of the blade height on each side. The flow at mid-span seems not to be affected.

3.4.2 Shadowgraphs

Shadowgraphs (Fig.60) are made for outlet Mach numbers between $M_{2,is} = 0.9$ and 1.0 (the isentropic Mach number $M_{2,is}$ is derived from downstream wall static pressures and the total upstream pressure).

The pictures show that the first shocks appear on the rear blade suction surface at $M_{2,is} = 0.9$. A close study of the photographs indicates also a different boundary layer behaviour

at the trailing edge of the blades. In fact, for the blades 5 and 7 (Fig. 60) the boundary layer separates under the influence of a normal shock while this does not happen (or to a much lesser extend) on blades 4 and 6. This suggests that for blades 4 and 6 the blade boundary layer has undergone a transition with the effect that the turbulent boundary layer resists better to the adverse pressure gradient imposed by the rear blade suction side shock. As far as the blades 5 and 7 are concerned, it seems that either the boundary layer has not undergone a transition or the transition has been followed by a relaminarization.

The different boundary layer behaviour is also picked up by the downstream traverses. The phenomenon is Mach number dependent. Between $M_2 = 0.5$ and 0.9 the losses do not differ by more than 0.3 points, however, beyond $M_2 = 0.9$ the differences increase rapidly and can reach 1 to 1.5 points around $M_2 = 1.0$. The test results presented in this report are therefore limited to $M_2 \approx 0.9$.

3.5 Overall performance test results

3.5.1 Profile losses

The losses are presented in Fig. 61 under the form

$$\xi = \frac{w_{2,is}^2 - w_2^2}{w_{2,is}^2} = 1 - \frac{1 - \left(\frac{P_{s,2}}{P_{0,2}}\right)^{\frac{K-1}{K}}}{1 - \left(\frac{P_{s,2}}{P_{0,1}}\right)^{\frac{K-1}{K}}}$$

The pressures used to calculate ξ are mass averaged values in the measuring plane. In subsonic flow there is no noticeable difference between these values and the completely mixed out values.

The losses are outlet Mach number dependent. From $M_2 = 0.5$ to $M_2 = 0.75$ the losses decrease from 3% to 2.5%. This minimum is followed by a rapid increase and at $M_2 = 0.9$ a value of $\xi = 4\%$ is recorded. The sudden deterioration of the blade performance must be related to the appearance of supersonic pockets on the blade suction surface.

A variation of $\pm 15^\circ$ of the inlet flow angle has no significant effect on the loss level. This can be attributed to the thick nose which is little sensitive to incidence variations.

An analysis of the losses with the Craig-Cox correlation [6] results in the following repartition of the individual loss terms :

	$M_2 = 0.5$ $RE = 4 \times 10^5$	$M_2 = 0.8$ $RE = 6.4 \times 10^5$
Basic loss term ξ	3.42%	3.42%
Correction factors : TE	1.15	1.15
RE	0.96	0.84
TOTAL PROF. LOSSES AFTER CRAIG & COX	3.05%	2.69%
MEASURED PROF. LOSS	2.95%	2.6%

The agreement between measured and calculated losses is satisfactory. The table indicates also that the drop in losses between $M_2 = 0.5$ and 0.8 is apparently a RE-number effect.

The Craig-Cox correlation allows also to calculate the profile losses in function of the inlet angle. Fig.62 presents the performance curve for the incidence range $\Delta\beta_1 = \pm 25^\circ$. Contrary to the experiments which did not show any incidence angle effect

for $\pm 15^\circ$; the loss correlation suggests an increase of $\Delta\xi = 0.5\%$ for the same range.

3.5.2 Outlet flow angle

The variation of the outlet flow angle β_2 in function of the outlet Mach number is very similar to the one of the losses (Fig.63). A certain relation between the blade loss variation and outlet angle variation is evident because of their coupling via the suction side boundary layer. It is, however, reasonable to suppose that in view of the small loss variation between $M_2 = 0.5$ and 0.8 the effect on the outlet angle should be very limited.

The prediction of the outlet flow angle is often made in a first approximation with the cos-rule :

$$\beta_2^* = \cos^{-1} \cdot \theta/s$$

0 - throat
s - spacing

The application of this equation is restricted to straight-backed blades with thin trailing edges at $M_2 = 1$.

For Mach numbers away from $M_2 = 1$, Traupel [19] proposes to calculate the outlet angle

$$\operatorname{ctg} \beta_2 = \frac{\theta}{s} \frac{1}{\sin \beta_0} \left\{ 1 - M_2^2 \cdot \frac{\kappa - 1}{2} \left[\left(\frac{\sin \beta_2^2}{\sin \beta_0} \right) - 1 \right] \right\}^{\frac{1}{\kappa - 1}}$$

β_0 = flow angle in the throat

This equation has to be solved iteratively.

The influence of the suction side curvature downstream of the throat on β_2 is taken into account due to Ainley [24] by

$$\Delta\beta_2 = \beta_2 - \beta_2^* = 4 \cdot (s/\theta)$$

where β_2^* represents the outlet angle predicted by the simple cos-rule.

The influence of the trailing edge thickness on β_2 can be evaluated after Bammert and Sonnenschein [25] with the equation

$$\cos\beta_2 = K_1 \left(\frac{\theta}{s} + K_2 \cdot \frac{d}{2 \cdot s} \right)$$

d - trailing edge thickness

K_1 - correction factor given in Ref. 20

$$K_1 = f \left(\frac{\theta}{s} + K_2 \cdot \frac{d}{2 \cdot s} \right)$$

$$K_2 = 0.8$$

The correction factors due to the rear suction side curvature and the trailing edge thickness are supposed to be constant in the whole subsonic Mach number range. The calculation procedure to be followed is :

1. calculate β_2 with the simple COS-rule;
2. add the corrections for the trailing edge thickness and the suction side curvature;
3. add the Mach number correction due to the difference of M_2 with respect to $M_2=1.0$.

The result is plotted in Fig.30. The variation of the outlet with M_2 is well predicted except for $M_2 > 0.8$, however, the predicted angles in this range are too high by 0.6° . The curves cross over at $M_2 \approx 0.9$.

3.6 Conclusions - High Speed Tests

The aim of the high speed tests was to measure the two-dimensional blade performance over a wide range of Mach numbers and inlet flow angles.

The tests included surface flow visualisations, shadowgraphs and mid-span probe traverses :

- the oil flow visualisation established undisturbed flow conditions at blade mid-span
- the two-dimensional blade performance could be correctly predicted for the outlet Mach number range $M_2 = 0.4$ to 0.8 by using the Craig & Cox loss correlation method and a modified cos-rule for the outlet angle
- beyond $M_2 = 0.8$ the shock boundary layer interactions are predominant and more refined prediction methods have to be used
- the shadowgraphs indicate in the transonic region a high sensitivity of the blade boundary layer to small variations in cascade and blade geometry.

REFERENCES

1. WHITNEY W.J., SZANCA E.M., MOFFIT T.P. and MONROE D.E. : Cold air investigation of a turbine for high-temperature engine application. Part I : turbine design and overall stator performance.
NASA TN D-3751, Jan. 1967.
2. SALVAGE J.W. : Measurement techniques for a secondary flow investigation.
von Karman Institute, in preparation.
3. PAPAILIOU K. : The calibration of one-directional probes.
von Karman Institute Internal Note 7A, Rhode-Saint-Genèse, Belgium, April 1969.
4. WOLF H. : Die Randverluste in geraden Schaufelgittern.
Wissenschaftliche Zeitschrift der Technischen Hochschule Dresden, 10, 1961, Heft 2.
5. HORLOCK J.H. : Axial flow turbines.
Butterworths, 1960.
6. CRAIG H.R.M. and COX H.J.A. : Performance estimation of axial flow turbines.
Proc. Inst. Mech. Engrs, 1970-71, Vol.185, 32/71, pp. 407-424.
7. BALJE O.E. and BINSLEY R.L. : Axial turbine performance evolution. Part A : Loss-geometry relationship.
ASME Journal of Engineering for Power, October 1968.
8. BELIK L. : An approximate solution for kinetic energy of secondary flow in blade cascades.
Int. J. Mech. Sci., Vol.10, 1968, pp.765-782.
9. BALJE O.E. : Axial cascade technology and application to flow path design. Part I : Axial cascade technology.
ASME Journ. of Eng. for Power, pp. 309-328, October 1968.
10. SALVAGE J.W. : Investigation of secondary flow behaviour and the end-wall boundary development through compressor cascades.
VKI TN 107, June 1974.
11. VAN DEN BRAEMBUSSCHE R. : Martensen's method for calculation of incompressible potential flow in cascade.
VKI CN 80, October 1970.

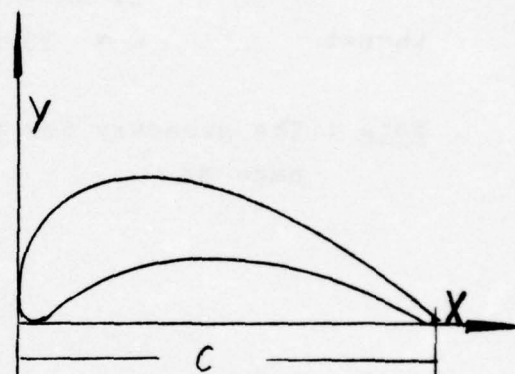
12. BARDON M.F., MOFFAT W.C. and RANDALL J.L. : Secondary flow effects on gas exit angle on rectilinear cascades.
ASME Paper 74-GT-69, April 1974.
13. LAKSHMINARAYANA B. and HORLOCK J.H. : Effect of shear flows on the outlet angle in axial compressor cascades.
Methods of prediction and correlation with experiments.
Journal of Basic Engineering, March 1967, pp.991-200.
14. HAWTHORNE W.R. and ARMSTRONG W.D. : Shear flow through a cascade.
The Aeronautical Quarterly, Vol.VII, November 1956.
15. SALVAGE J.W. : A review of the current concept of cascade secondary flow effects.
VKI TN 95, March 1974.
16. LANGSTON L.S., NICE M.L., HOOPER R.M. : Three-dimensional flow within a turbine cascade passage.
ASME Paper 76-GT-50.
17. HORLOCK J.H. : Cross-flows in bounded three-dimensional turbulent boundary layers.
Cambridge U., CUED/A - Turbo/TR 28, 1971.
18. MASKELL E.C. : Flow separation in three dimensions.
Royal Aircraft Establishment, Report No.Aero. 2565, Nov. 1955.
19. BELIK L. : The secondary flow about circular cylinders mounted normal to or flat plate.
Aeronautical Quarterly, Feb. 1973, pp.47-54.
20. STANBROOK A. : Experimental observation of vortices in wing-body junctions.
Royal Aircraft Establishment, Report No. Aero 2589, March 1957.
21. SENOO Y. : The boundary layer on the end wall of a turbine nozzle cascade
Trans. ASME, Vol. 80, Nov. 1958, pp. 1711-1720.
22. SJOLANDER S.A. : The endwall boundary layer in an annular cascade of turbine nozzle guide vanes.
Department of Mechanical and Aeronautical Engineering, Carleton University, Ottawa, Canada. Technical Report No. ME/A 75-4, Dec. 1975.
23. TRAUPEL W. : Thermische Turbomaschinen.
Springer Verlag Berlin, 1960.
24. AINLEY D.G., MATTHIESON G.C.R. : A method of performance estimation for axial flow turbines.
ARC R&M 2974, 1957.

25. BMMERT K. and SONNENSCHIN H. : Der Einfluss verdickter und verdünnter Turbinenschaufeln auf die Gittereigenschaften. Archiv für das Eisenhüttenwesen, 38 Jahrgang Heft, 1974.

APPENDIX A : BLADE COORDINATES AND CASCADE
CONFIGURATION

1. Blade coordinates

$\frac{x}{c}$	$(\frac{y}{c})$ suction surface	$(\frac{y}{c})$ pressure surface
0.0000	.0683	.0683
.0455	---	.1707
.0910	---	.2212
.1365	.0273	.2540
.1821	.0478	.2745
.2276	.0651	.2868
.2731	.0792	.2927
.3186	.0897	.2927
.3641	.0974	.2890
.4096	.1029	.2813
.4552	.1047	.2708
.5007	.1038	.2594
.5462	.1015	.2462
.5917	.0965	.2312
.6372	.0892	.2153
.6827	.0797	.1971
.7283	.0696	.1780
.7738	.0583	.1570
.8193	.0469	.1343
.8648	.0341	.1102
.9103	.0209	.0833
.9558	.0073	.0551
1.000	.0159	.0159



Leading edge radius
to chord ratio

$$\left(\frac{R}{C}\right)_{LE} = .066$$

Trailing edge radius
to chord ratio

$$\left(\frac{R}{C}\right)_{TE} = .015$$

2. Cascade geometry for low speed cascade

chord	$c = 120 \text{ mm}$
pitch	$s = 87 \text{ mm}$
stagger angle	$\gamma = -42.5^\circ$
solidity	$\sigma = 1.38$
aspect ratio	1. AR = .42
	2. AR = .67
	3. AR = .98
throat	$O = 33 \text{ mm}$

Note : The geometry for the high speed cascade is listed on
page 38.

APPENDIX B : SECONDARY FLOWS IN PLANE CASCADES

This section summarizes briefly the main features of cascade secondary flows. A detailed literature review on the subject can be found in Ref. [15].

Let us consider a plane cascade of blades. The inlet end wall boundary layer is supposed to be colateral. The inlet flow will be deflected by the blade row, and through application of the equilibrium equations it is noted that this deflection must be associated with cross-channel pressure gradients in the inviscid flow. As a result of the boundary layer flow assumption that the inviscid flow impresses its gradients on the boundary layer, a balance of the equilibrium equations with the boundary layer shows a required movement of boundary layer material from the high pressure side of the channel, producing a "cross flow" component of velocity perpendicular to the "streamwise" velocity component. This will initiate a vortex-like motion of the flow within the passage, the flow being overturned near the wall : it is the so-called "passage vortex". Moreover, the end-wall BL streamlines are likely to roll up into a vortex type motion near the corner of the blade suction surface and the end wall : it is the so-called "corner vortex".

Another secondary motion of interest is the one occurring when a non-uniform flow (the inlet wall boundary flow is forced to pass round an obstacle (the blade leading edge) : this leads to the formation of a so-called "horse-shoe" or "stagnation vortex" which is wrapped around the leading edge.

Finally, we must note that there are still two additional components of vorticity which may influence the flow in the blade end region.

- the "trailing shed circulation", attributed to changes in blade circulation along the blade span as the blade end is approached.
- the "trailing filament circulation", due to the stretching of approach flow vortex filaments.

A simple model for the passage vortex
(small shear - small disturbance theory)

Assuming an isentropic evolution of the flow through the passage and representing the inlet boundary layer by a vorticity distribution $\xi_1 = -dV_1/dy$, it is shown in [15] that the streamwise outlet vorticity can be written $\xi_2 = -B dV_1/dy$. Neglecting the influence of secondary velocity on the main flow, B can be written

$$B = 2 V_1 V_2 \int_{\beta_1}^{\beta_2} \frac{1}{V^2} d\beta,$$

leading to the well-known result of Squire and Winter $B = -2(\beta_1 - \beta_2)$ if the velocity V is constant.

Assuming that $\frac{\partial V}{\partial x} \approx 0$ locally in the vicinity of the outlet station and defining ξ a secondary flow stream function ψ , we can write

$$\frac{\partial^2 \psi}{\partial y^2} + \frac{\partial^2 \psi}{\partial z^2} = -\xi_2 = B \frac{dV_1}{dz} \quad (1)$$

$$\text{with } v_y = \frac{\partial \psi}{\partial z}$$

$$v_z = -\frac{\partial \psi}{\partial y}$$

Solutions of the equation must be found satisfying the boundary conditions that no flow passes through the physical end wall or through the (hypothetical) surfaces that separate

the flow in one passage from that of the neighbouring passages. The symmetrical nature of cascade flows about mid-span allows one of those boundary conditions to be modified to imply that there can be no component of velocity normal to the end wall at the cascade mid-span position.

A solution of equation (1) being obtained, the resulting velocity component V_2 can be averaged in order to determine the influence of secondary flow on the spanwise distribution of outlet flow angle.

Two methods of solution will be outlined in the following. The first one is a simple integral method providing directly the average outlet cross flow velocity. The second method involves the numerical solution of equation (1).

a) Horlock's solution

Introducing an empirical parametric solution for V_g and V_2 in the secondary flow equations (continuity + vorticity), Horlock [17] arrives at the following solution

$$\frac{V_z(y)}{V_{1MS}} = B \left(1 - \frac{\bar{V}_{x1}(y)}{\bar{V}_{1MS}} - k \delta_{x1}^* e^{-ky} \right)$$

under the assumption that

- V_x is a function of y only
- B is constant
- $\frac{h}{s \cos \beta_2} \gg 1$
- $k = \frac{\sqrt{12}}{s \cos \beta_2} \ll 1$

Salvage [10,15] proposed to use this result in order to predict the spanwise variation of the outlet flow angle. This leads to the following first approximation formula :

$$\Delta\beta_2(y) = \beta_{2MS} - \beta_2(y) = \tan^{-1} \left[\frac{\cos\beta_1}{\cos\beta_2} B \left(1 - \frac{V_{x1}(y)}{V_{1MS}} - k\delta_{x1}^* (e^{-ky} - e^{-k\frac{h}{2}}) \right) \right]$$

$$\text{where } k = \frac{\sqrt{12}}{s \cos\beta_{2MS}}$$

b) Numerical solutions

This method involves the solution of Eq.(1) (with the relevant boundary conditions).

A finite element method was chosen, using linear triangular elements (TRIM3). The computing plane is located downstream of the cascade, normally to the streamlines and covers half a blade passage (the flow being symmetrical about mid-span, only half of a blade height has to be considered).

This computing plane is covered by approximately 450 nodes. The inversion of the stiffness matrix is performed by a fast direct method (Choleski method), leading to an execution time of the program of approximately 4 CP seconds on a CDC 6500 computer.

The secondary velocities can then be calculated by numerical derivations. The average velocity \bar{V}_z is then used to predict the outlet flow angle variation in the same way as in point a).

The knowledge of secondary velocities allows us also to compute the kinetic energy of secondary flow, KE_s

APPENDIX C

1. Profile loss related to blade boundary layer parameters
(momentum flow averaging)

$$\bar{\omega}_p = 1 - \cos^2 \beta_2 (2A - B^2) - \sin^2 \beta_2 \cdot \left(\frac{A}{B}\right)^2$$

$$A = 1 - \delta_e^* - \theta_e$$

$$B = 1 - \delta_e^*$$

$$\delta_e^* = \frac{\delta_{ss}^* + \delta_{ps}^* + t_e}{s \cdot \cos \beta_2}$$

$$\theta_e = \frac{\theta_{ss} + \theta_{ps}}{s \cdot \cos \beta_2}$$

ss : suction side

ps : pressure side

t_e : trailing edge thickness

2. Cross flow momentum thickness (derived from Horlock's expression for secondary velocity)

$$\theta_{z2} = B^2 \left(\frac{\bar{V}_1}{\bar{V}_2} \right)_{MS} \left\{ \delta_x^* - \theta_{x1} + k \delta_x^{*2} \left[\frac{3}{4} (e^{-kh} - 1) + \frac{kh}{2} e^{-kh} \right] \right\}^2$$

3. End-wall area averaged loss coefficient :

$$\bar{\omega}_{EW,A} = \frac{2}{h} (\delta_{x2}^* + \theta_{x2} - \theta_{z2})$$

TABLE 1 : SUMMARY OF OVERALL TESTS PARAMETERS

Test	AR	DX/C ⁽¹⁾	N2 ⁽²⁾	N1 ⁽³⁾
1	.98	1	15	17
2	.98	2/3	15	17
3	.98	1/3	15	17
4	.42	1/3	13	14
5	.42	2/3	13	14
6	.42	1	13	14
7	.67	1	13	17
8	.67	2/3	13	17
9	.67	1/3	13	17

- (1) DX/C : distance between the outlet measuring plane and the trailing edge plane, in the streamwise direction.
- (2) N2 : number of pitchwise outlet traverses. Each outlet traverse contains 35 points separated by 2.5mm in the pitchwise direction.
- (3) N1 : number of points in each spanwise inlet traverse. There are three inlet traverses separated by 1/2 of a pitch in the pitchwise direction.

Mean flow conditions :

$$\bar{P}_{01MS} - P_{at} = 70 \text{ mm H}_2\text{O}$$

$$\bar{P}_2 = P_{at}$$

$$\beta_1 = 90^\circ$$

$$\beta_2 = 24^\circ$$

$$V_1 = 12 \text{ m s}^{-1}$$

$$V_2 = 32 \text{ m s}^{-1}$$

$$R_e = V_2 \cdot C/S_2 = 250.000$$

$$\text{Inlet wall boundary layer thickness } \delta_1 = 6,75 \text{ mm}$$

TABLE 2 : SUMMARY OF TEST RESULTS

Test	AR	DX/C	$\bar{\omega}_{MS,M}$	$\bar{\omega}_{MS,A}$	$\bar{\omega}_M$	$\bar{\omega}_A$	$\bar{\beta}_{2MS,M}$	$\bar{\beta}_{2MS,A}$
1	.98	1	.060	.062	.059	.085	- 66.0	- 66.0
2	.98	2/3	.063	.063	.058	.083	- 65.3	- 65.3
3	.98	1/3	.049	.052	.056	.086	- 65.5	- 65.7
4	.42	1/3	.071	.079	.069	.130	- 64.4	- 64.5
5	.42	2/3	.089	.095	.077	.134	- 64.4	- 64.4
6	.42	1	.099	.105	.081	.140	- 64.1	- 64.1
7	.67	1	.067	.068	.068	.106	- 66.4	- 66.4
8	.67	2/3	.066	.068	.068	.105	- 66.6	- 66.6
9	.67	1/3	.061	.061	.061	.098	- 66.9	- 67.0

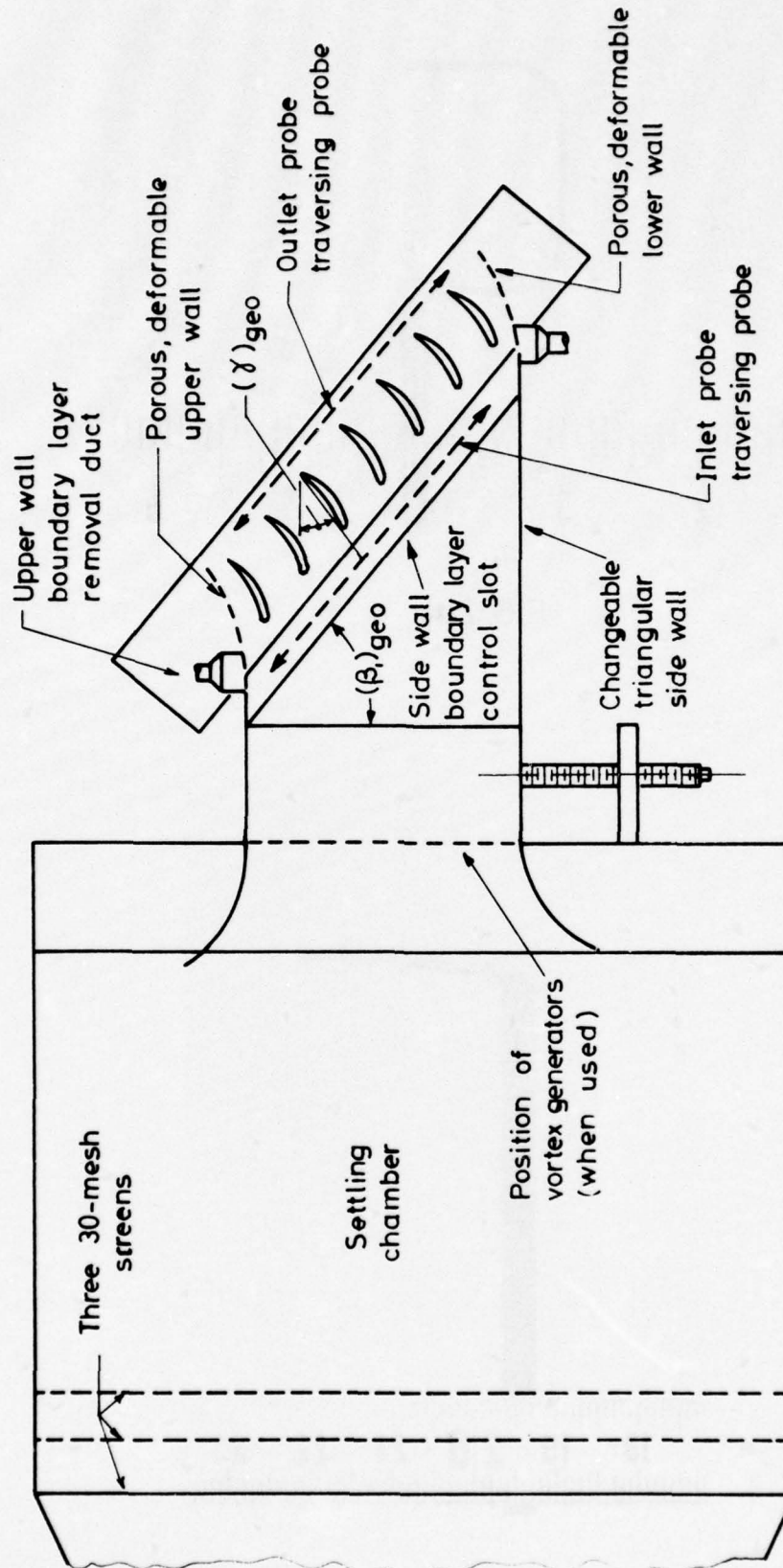


Figure 1. Vertical cross section of C-1 cascade tunnel.

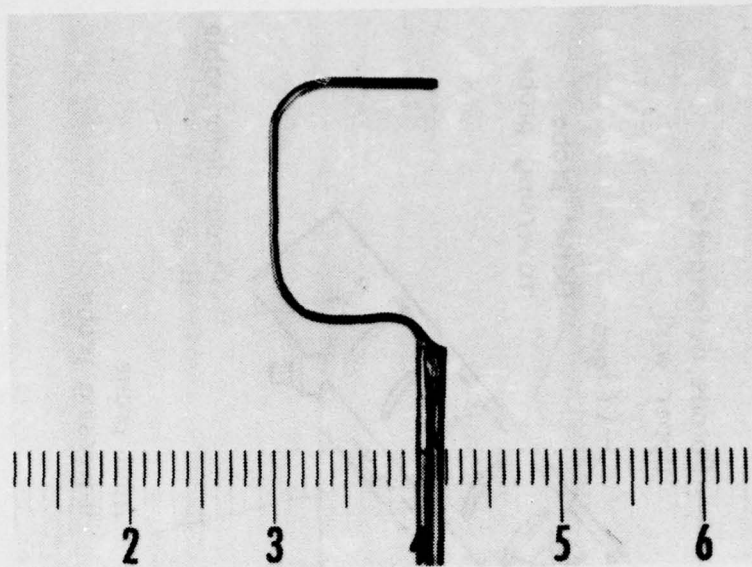


FIG. 2a)

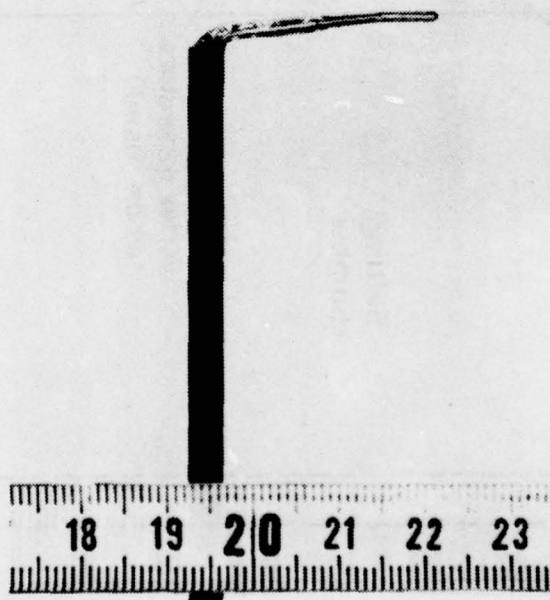


FIG 2 b)

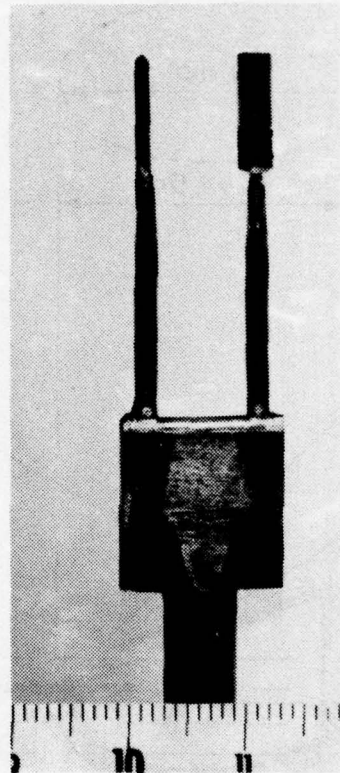


FIG. 3

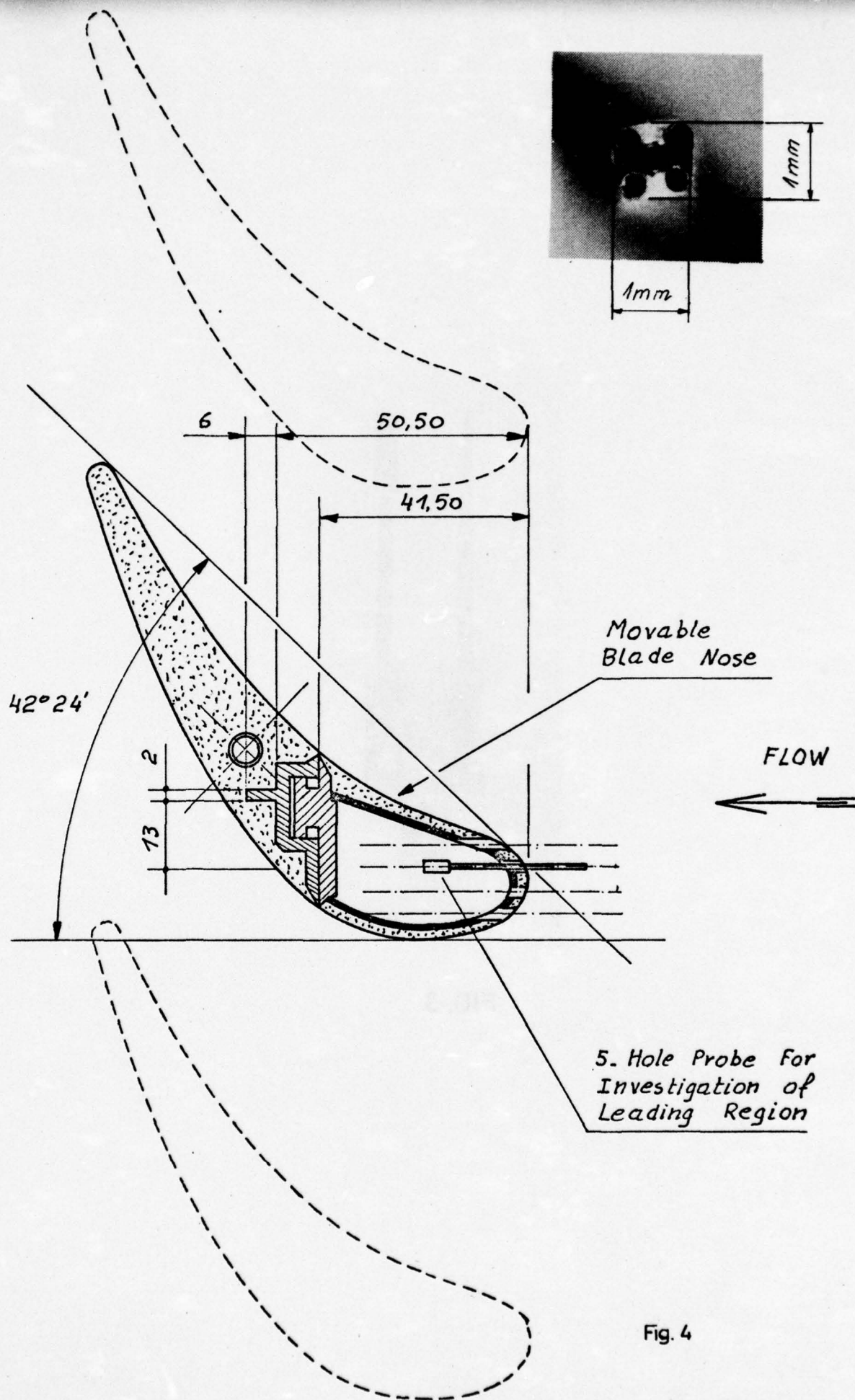


Fig. 4

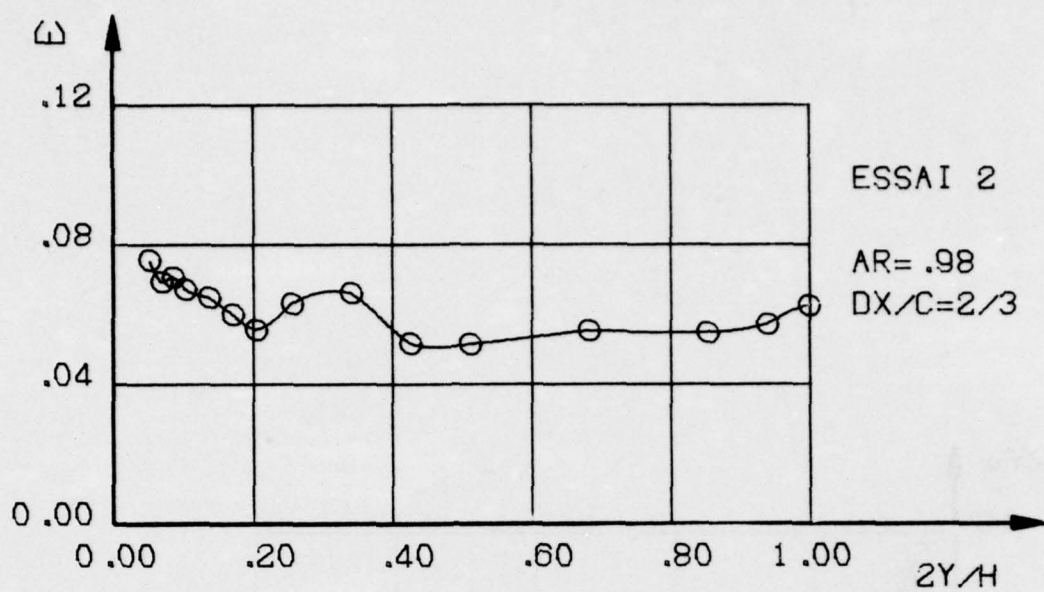


Fig. 5

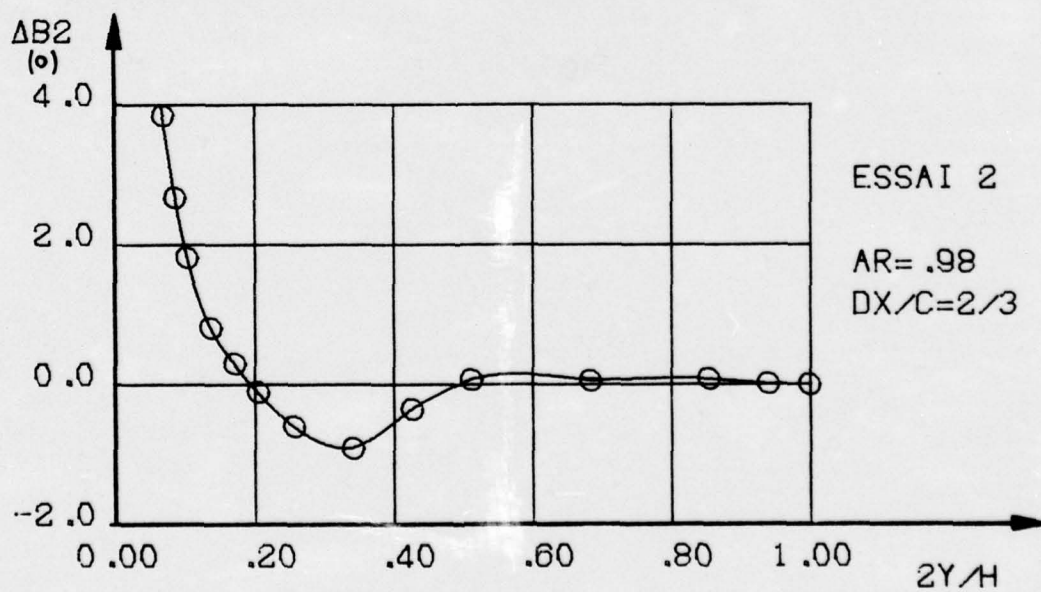


Fig. 6

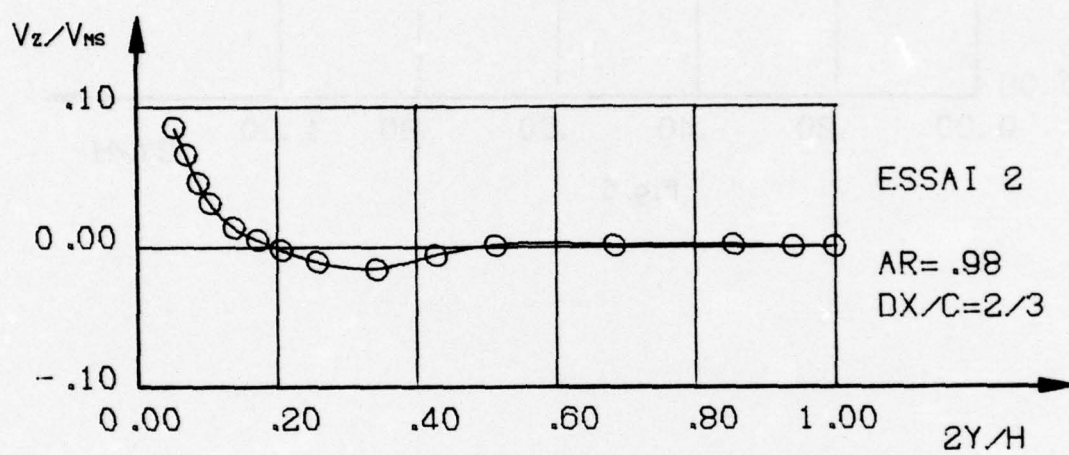


Fig.7

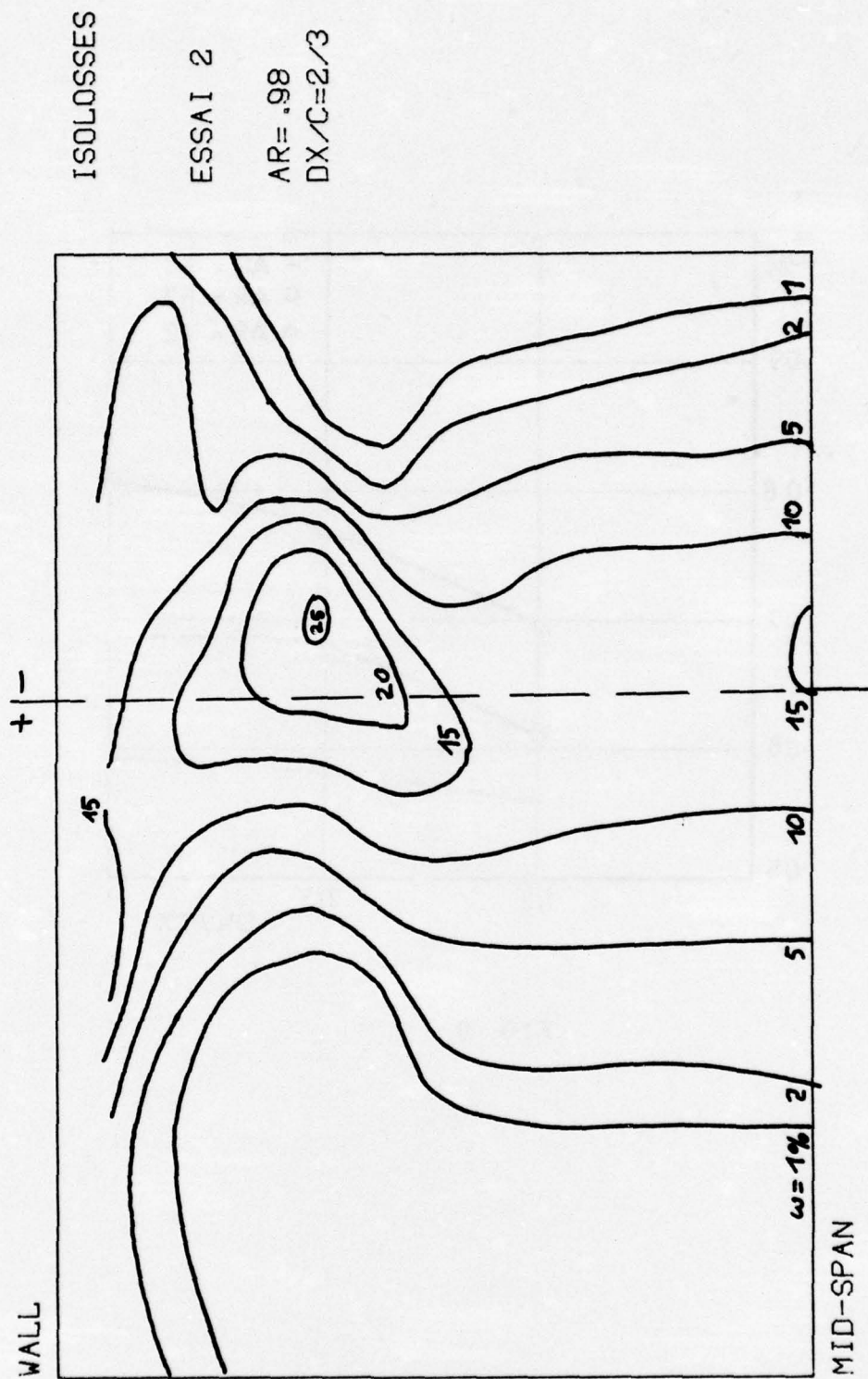


Fig. 8

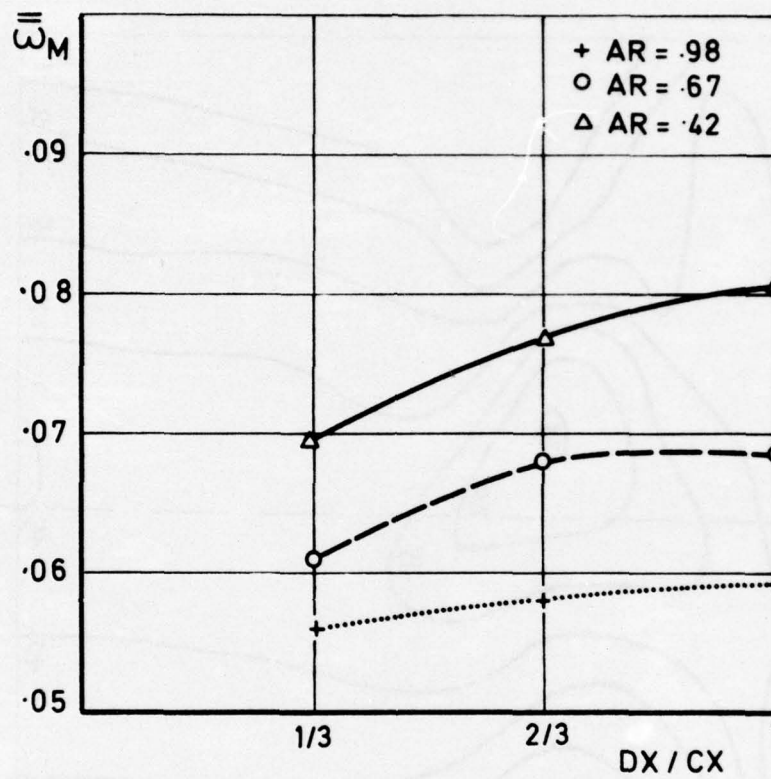


FIG. 9

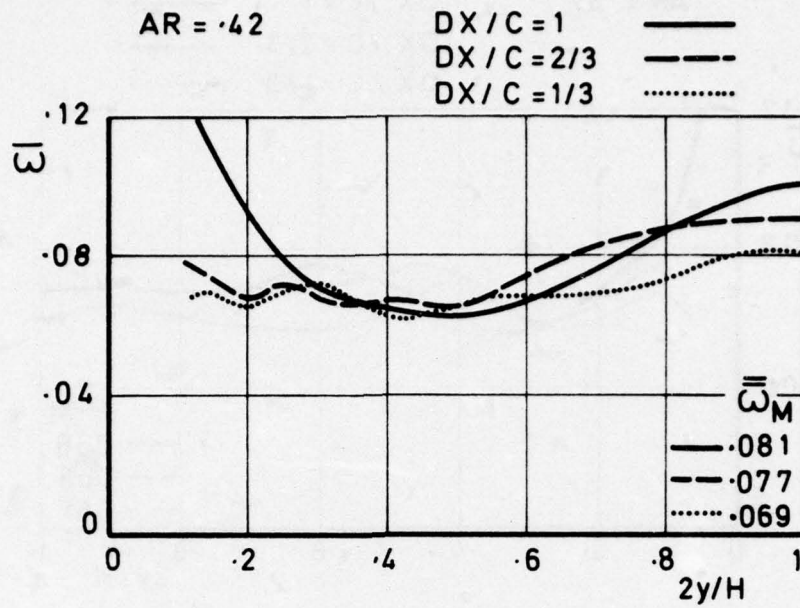


FIG. 10 a)

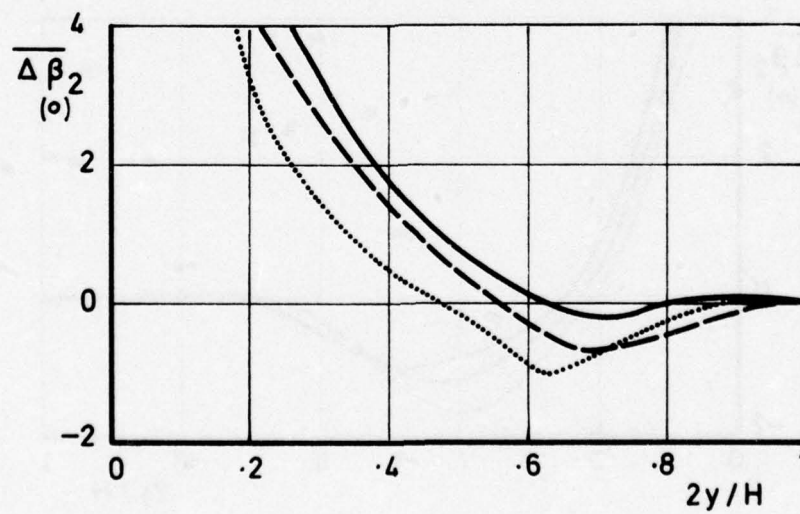


FIG. 10 b)

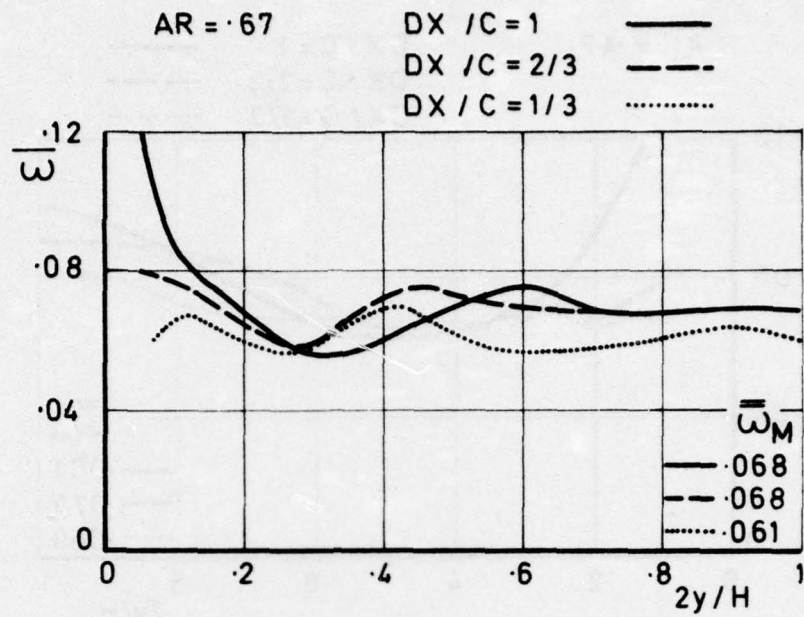


FIG. 11 a)

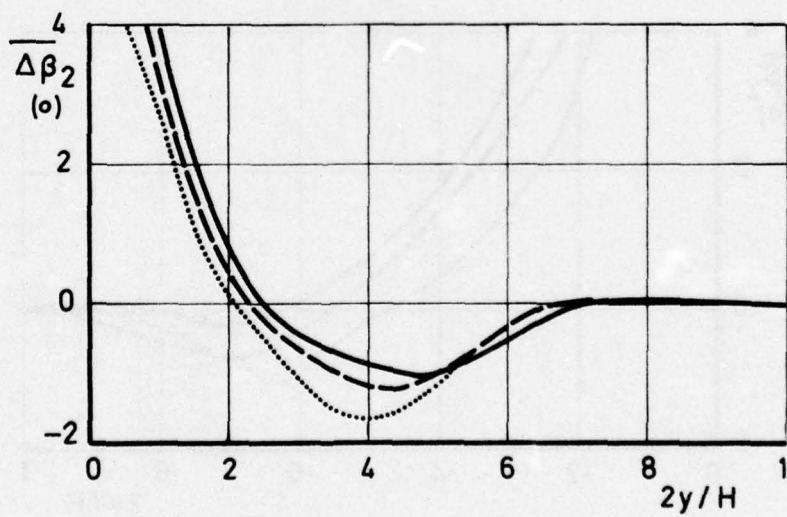


FIG. 11 b)

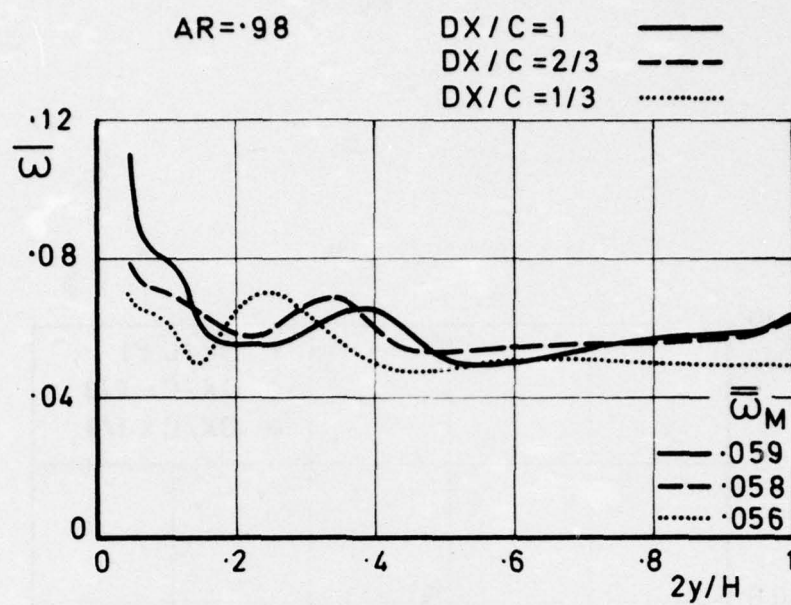


FIG. 12 a)

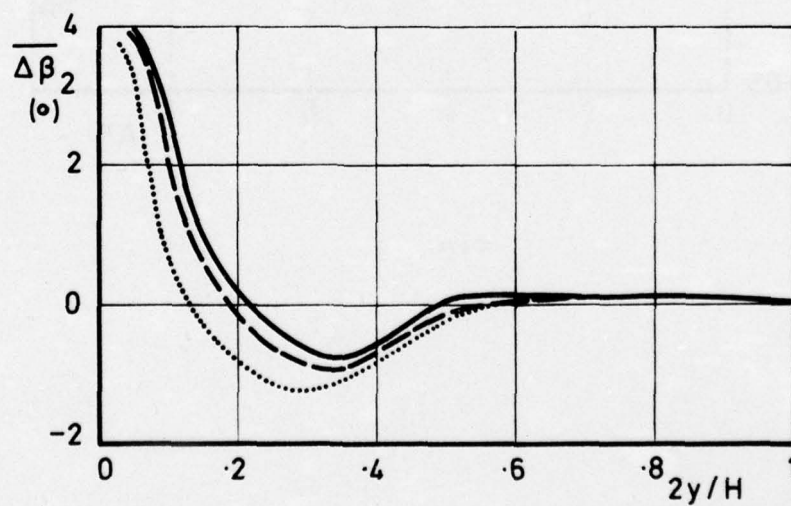


FIG. 12 b)

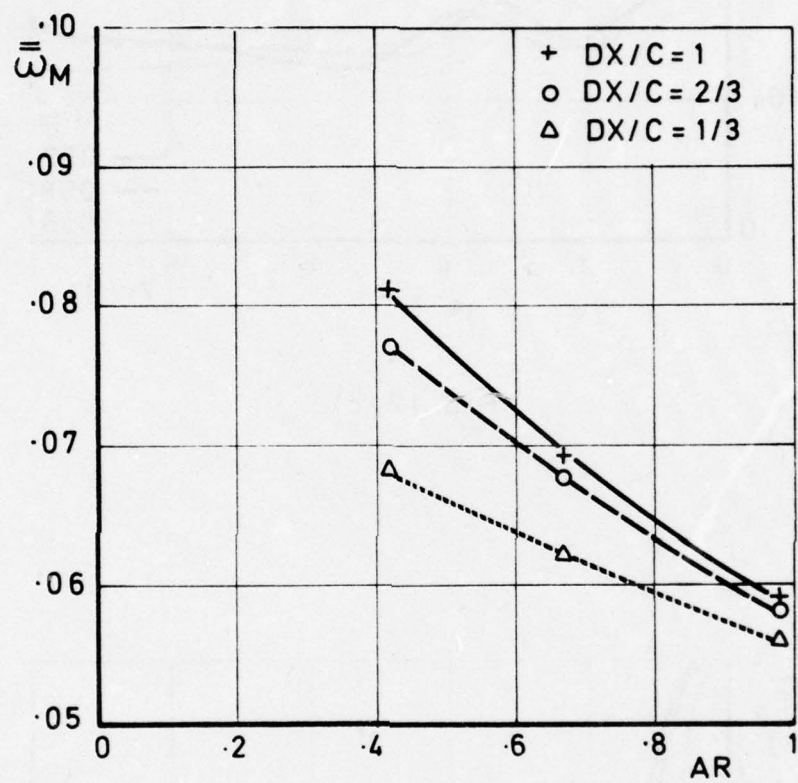


FIG. 13

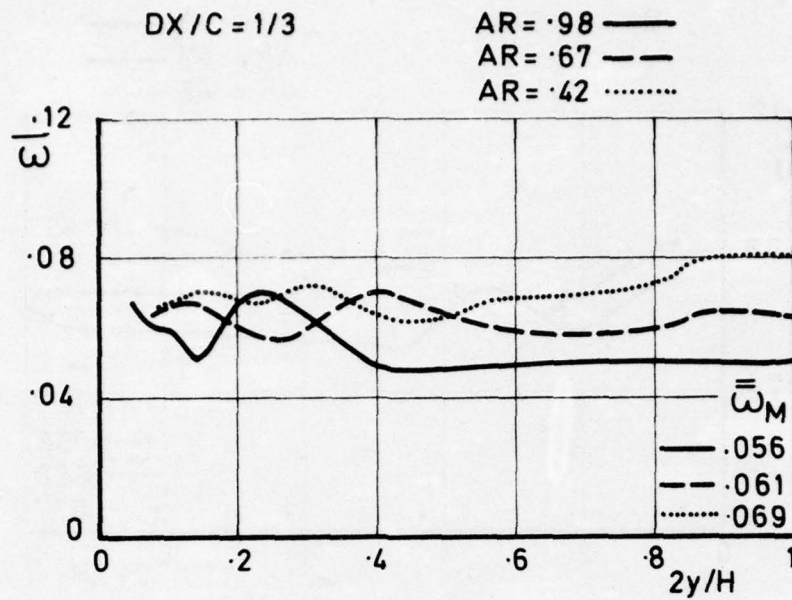


FIG. 14 a)

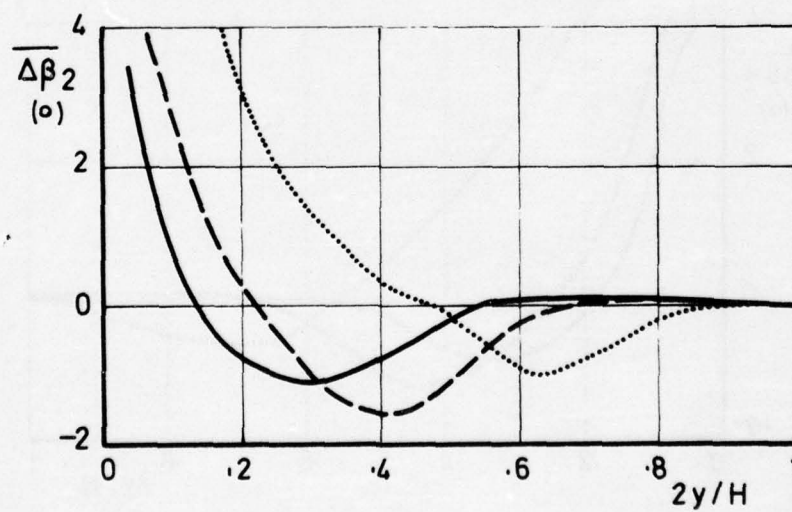


FIG. 14 b)

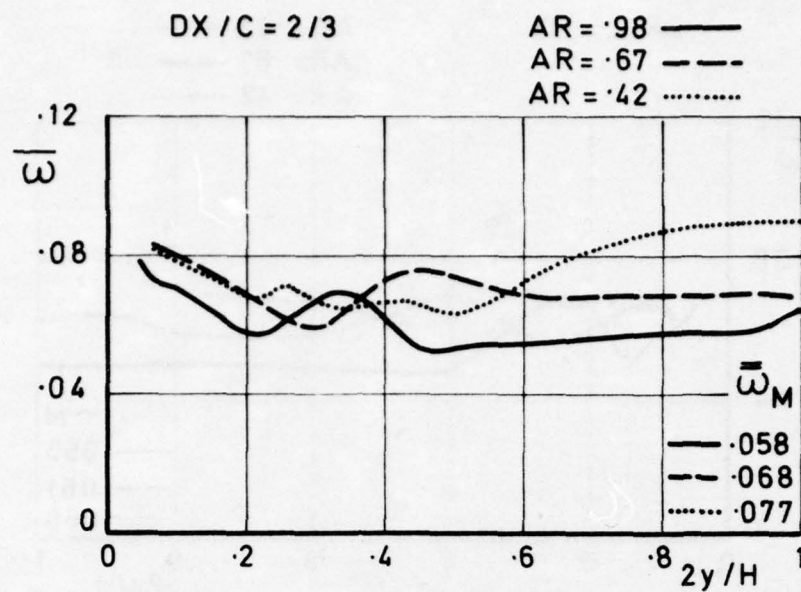


FIG. 15 a)

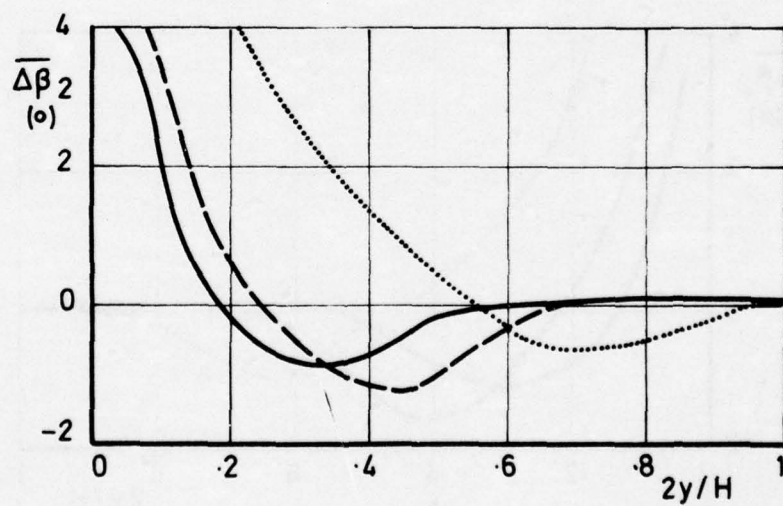


FIG. 15 b)

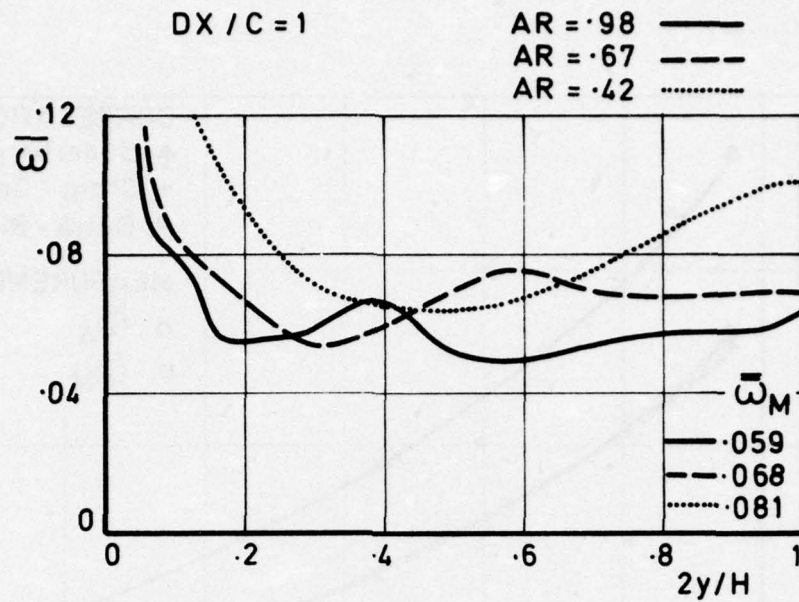


FIG. 16 a)

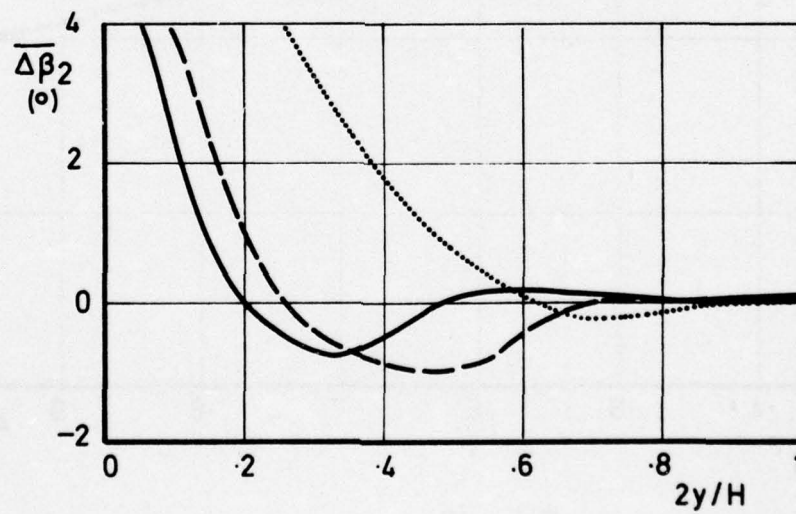


FIG. 16 b)

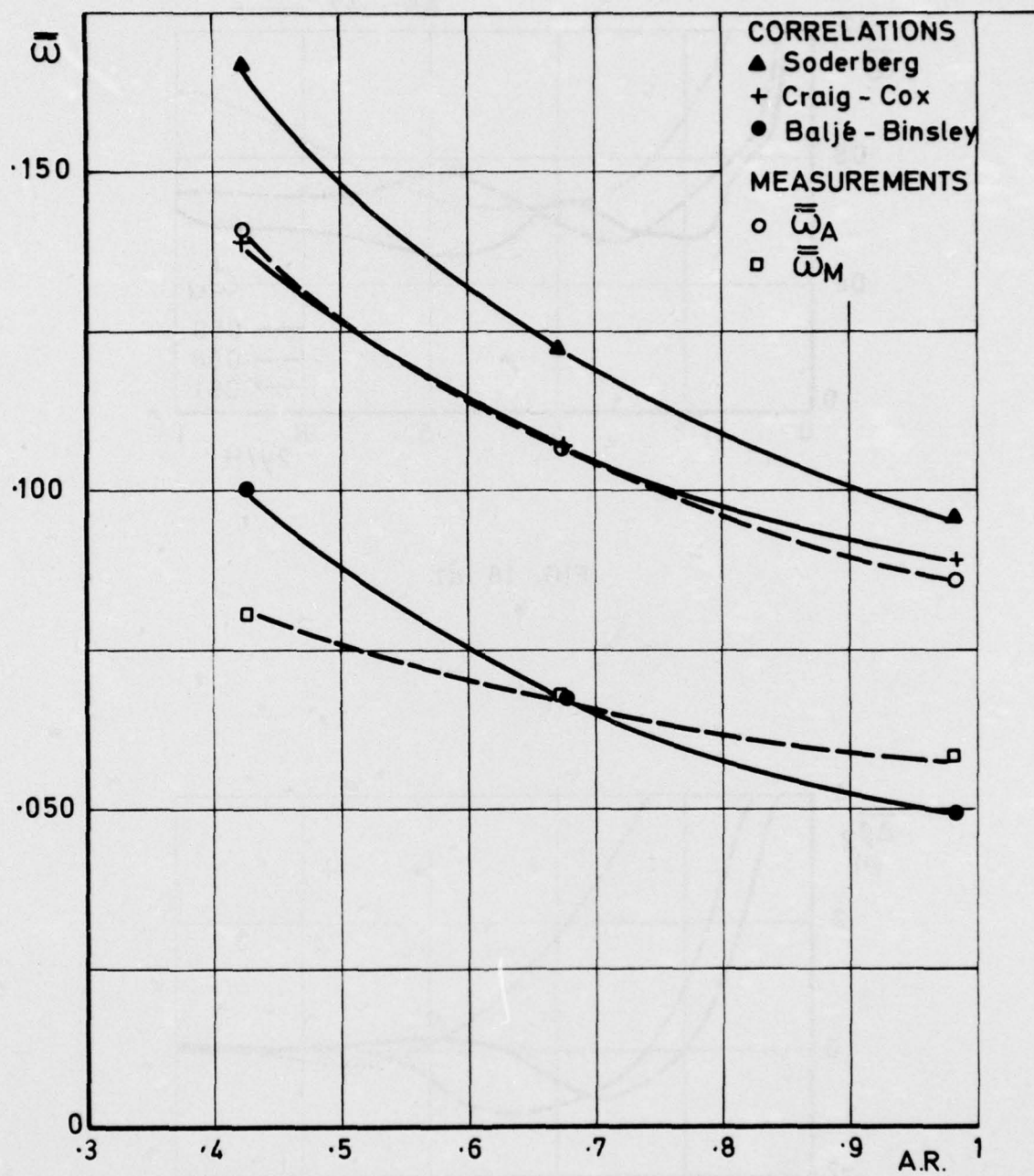


FIG. 17

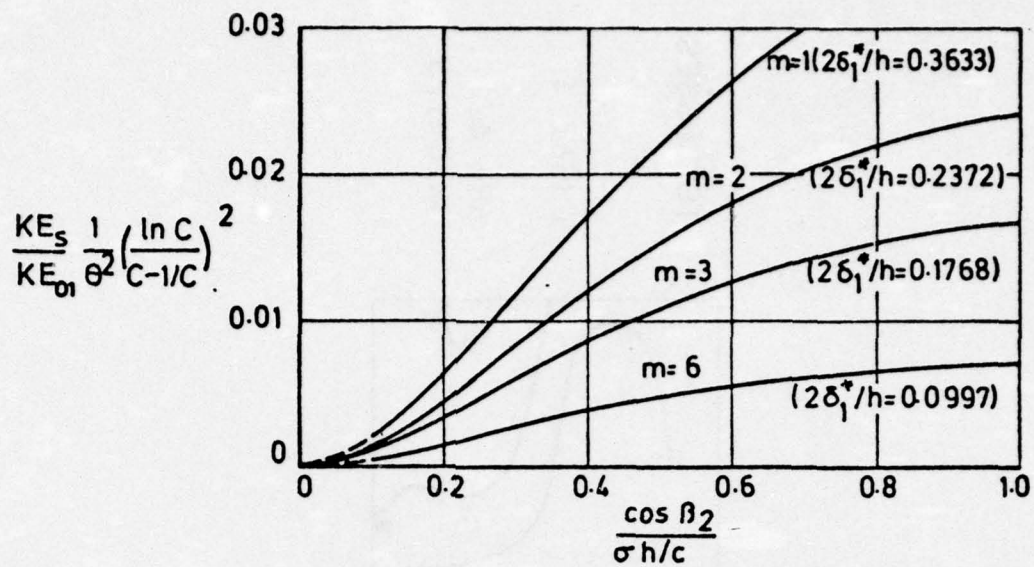


FIG. 18
BELIK'S SOLUTION FOR SECONDARY FLOW KINETIC ENERGY

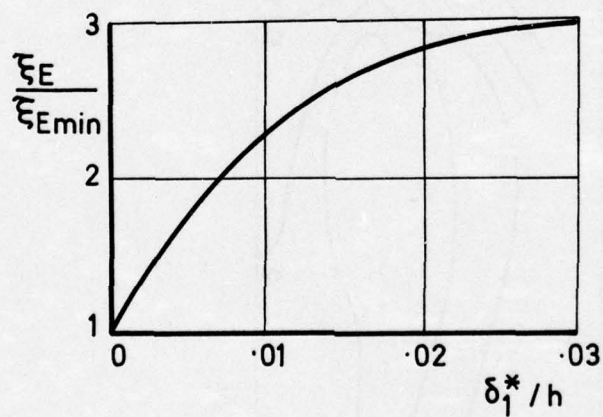


FIG. 19
DEPENDANCE OF END-WALL LOSSES ON INLET
BOUNDARY LAYER (9)

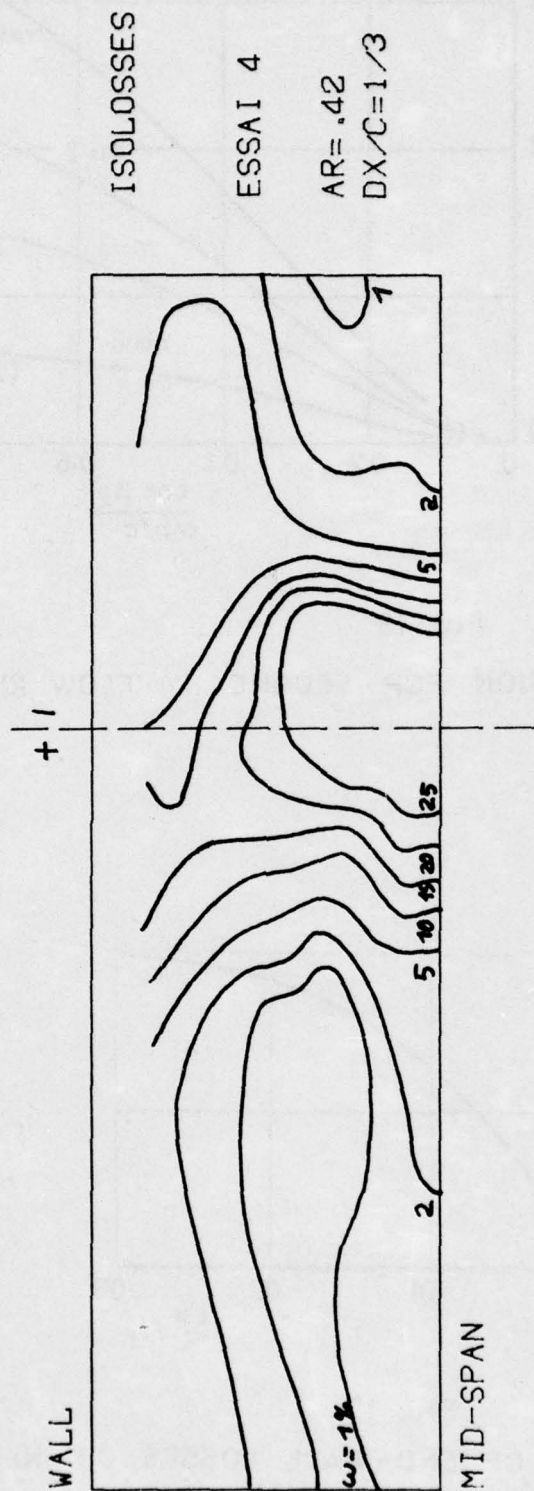


FIG. 20

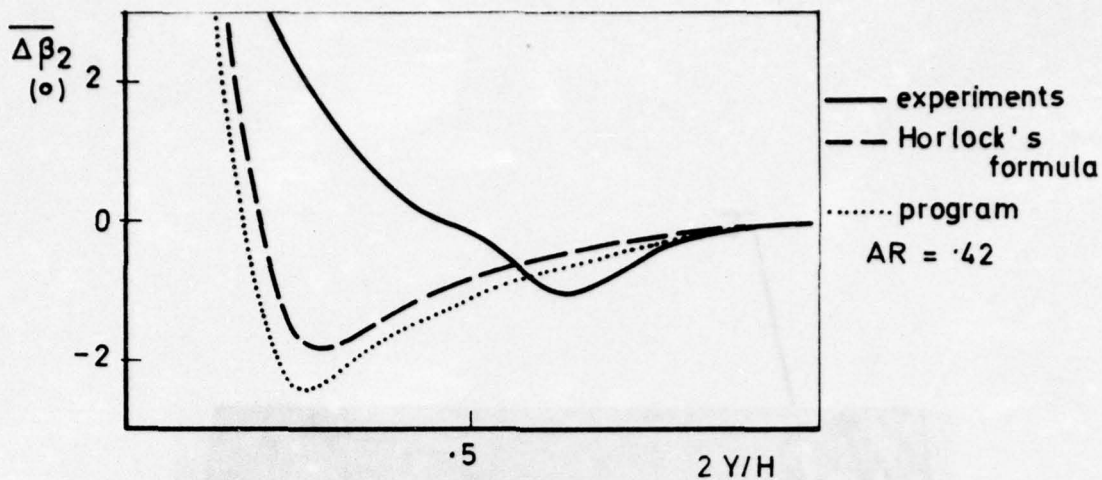


FIG. 21 a)

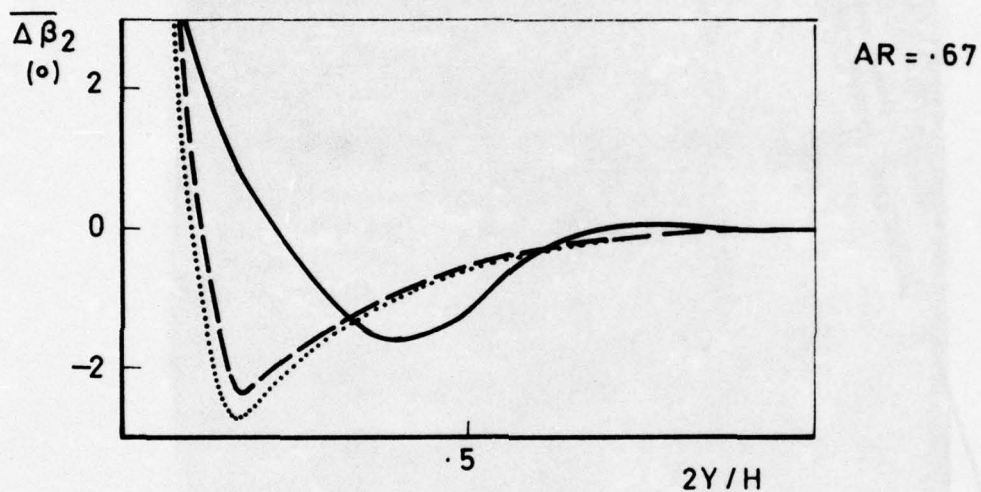


FIG. 21 b)

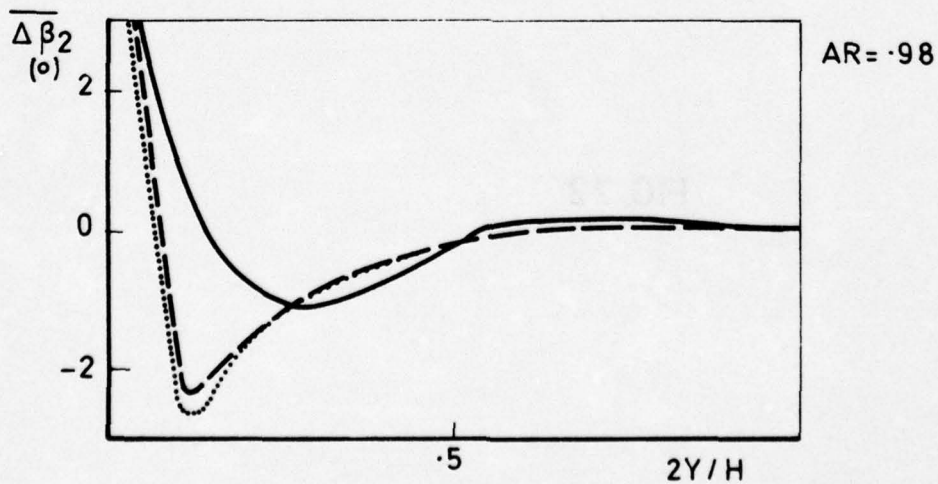


FIG. 21 c)

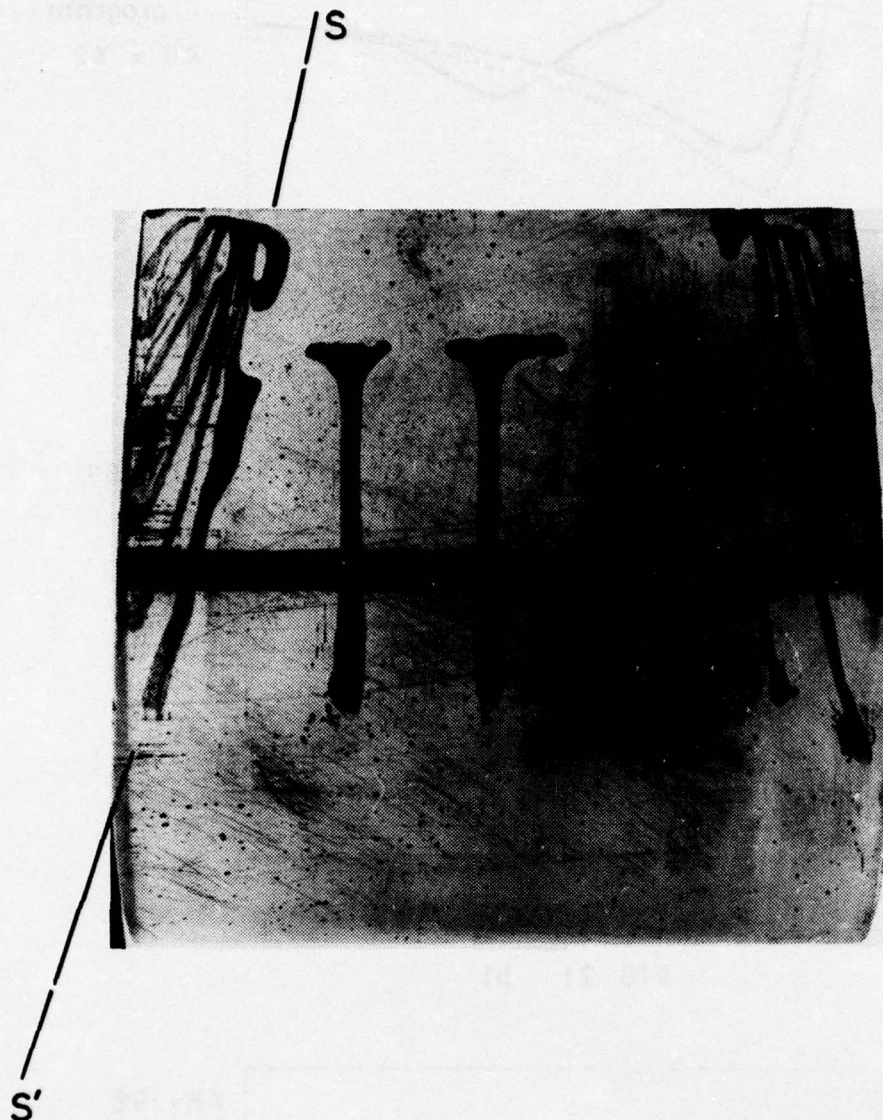


FIG. 22



FIG. 23

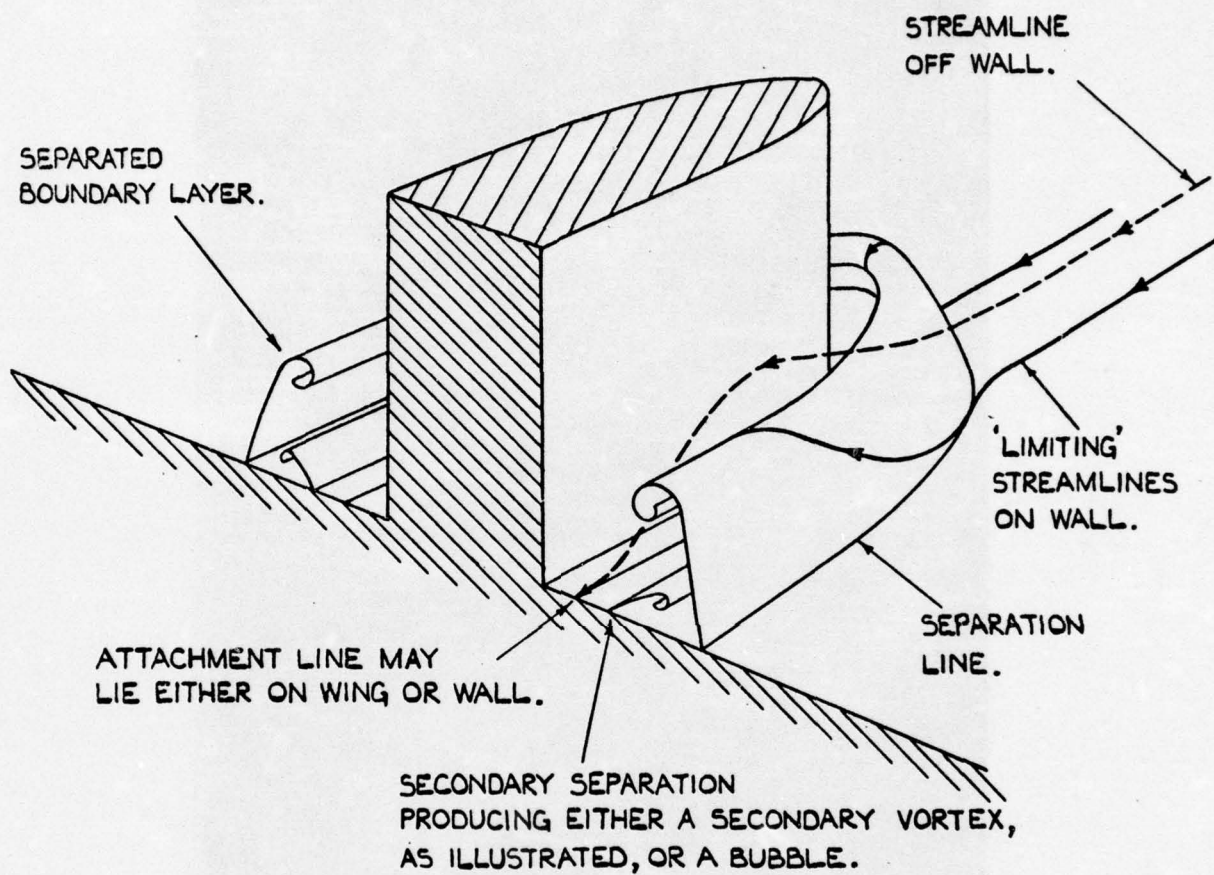


FIG. 24

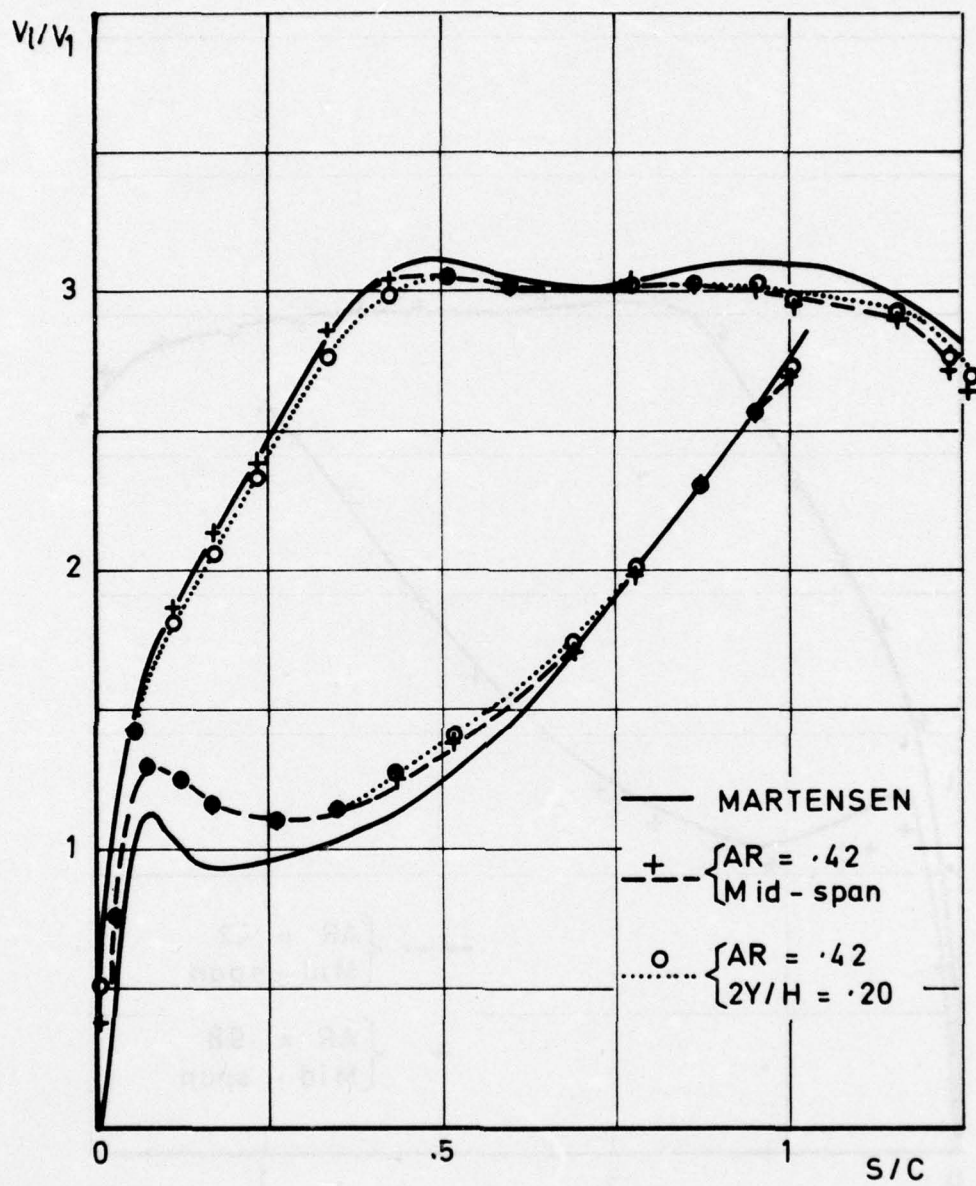


FIG 25 a)

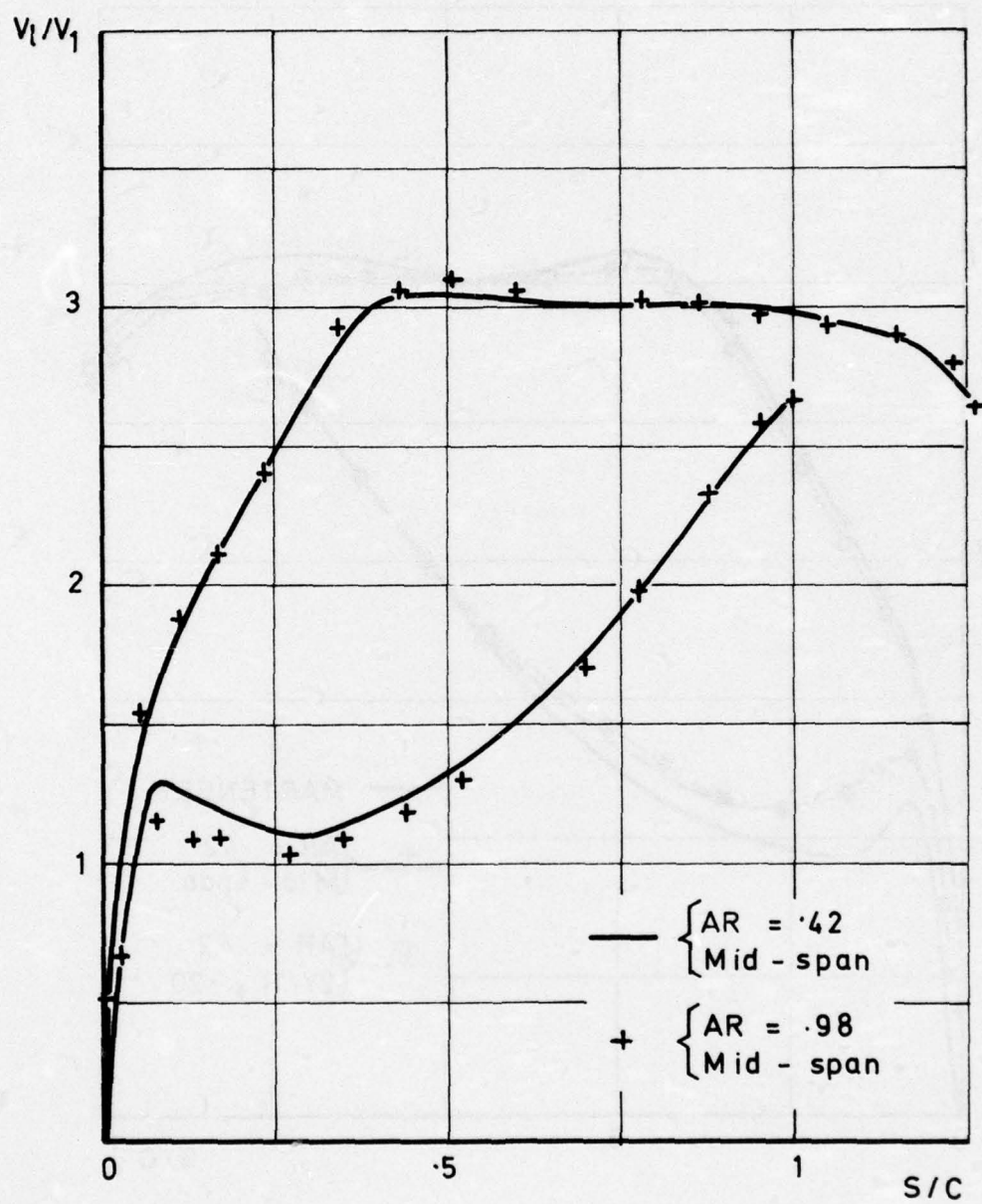


FIG. 25 b)

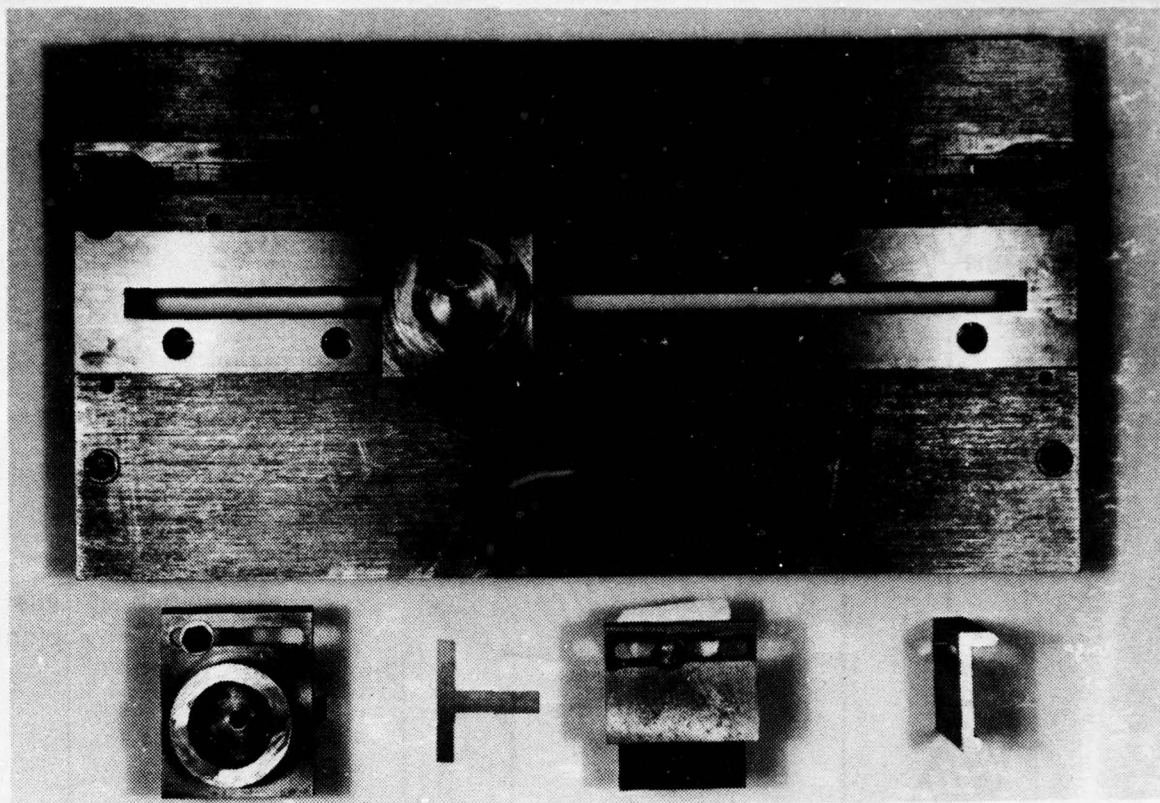


FIG. 26 a)

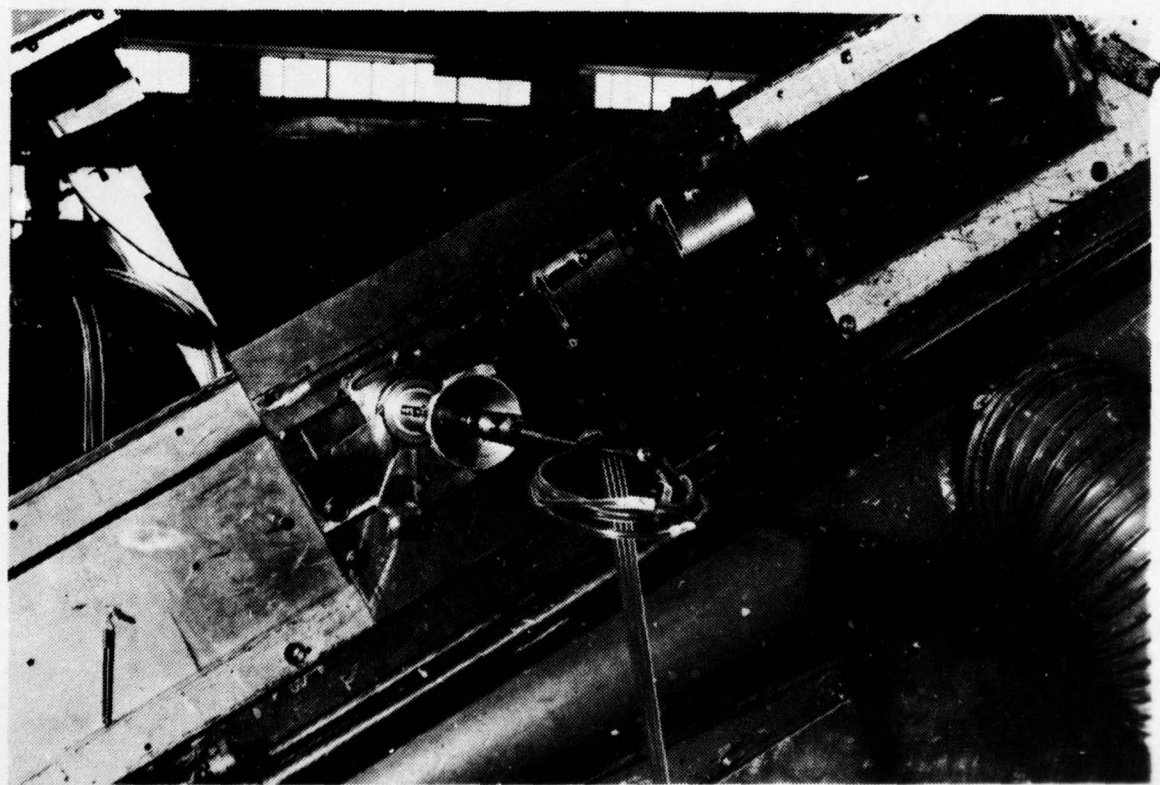


FIG. 26 b)

AD-A032 262

VON KARMAN INST FOR FLUID DYNAMICS RHODE-SAINT-GENESE--ETC F/G 20/4
FILM COOLED SMALL TURBINE BLADE RESEARCH. VOLUME I. AERODYNAMIC--ETC(U)
JUN 76 C SIEVERDING, P MARCHAL

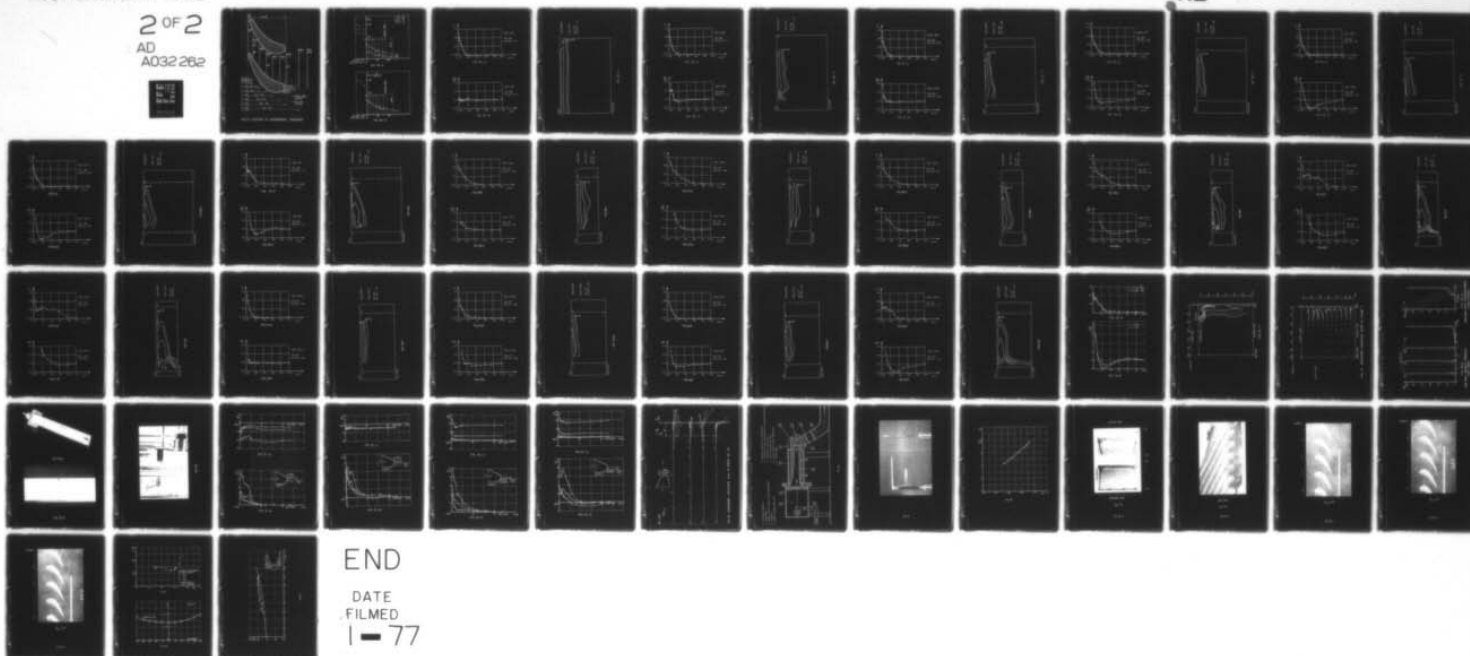
DA-ERO-75-G-074

NL

UNCLASSIFIED

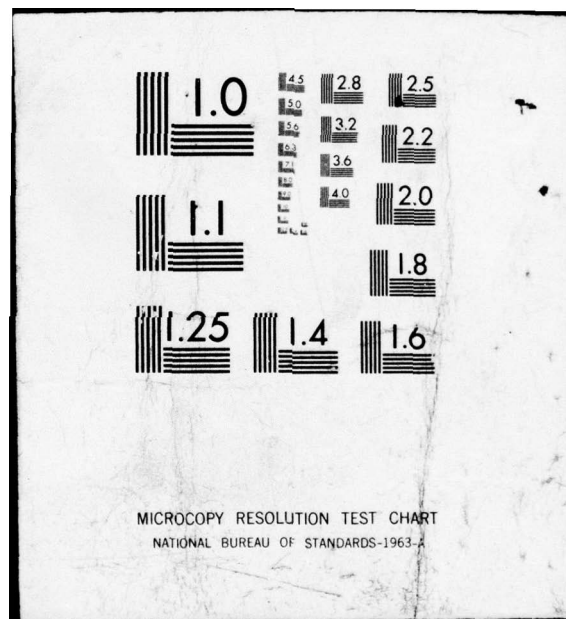
2 OF 2

AD
A032 262



END

DATE
FILMED
1-77



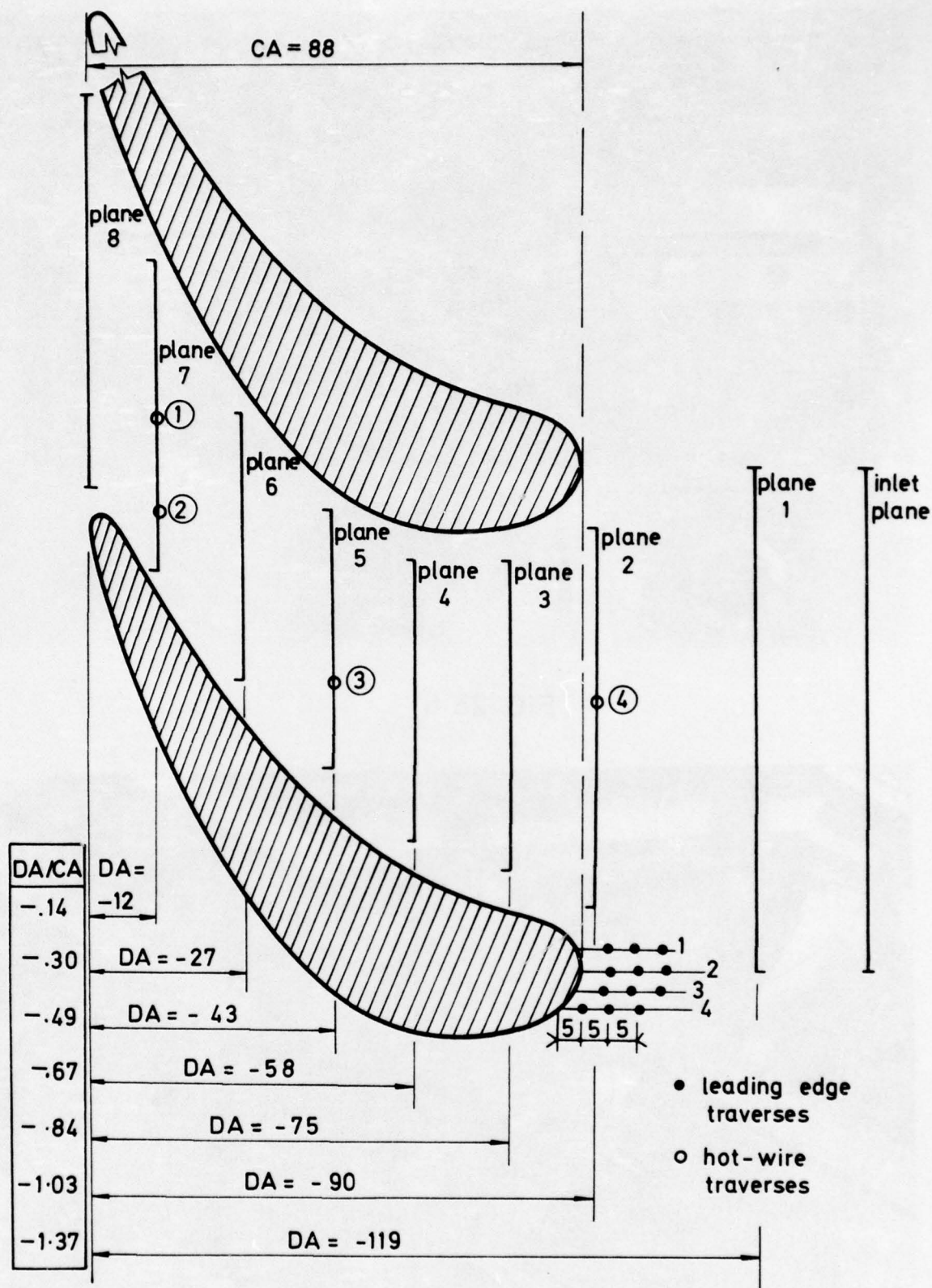


FIG. 27 LOCATION OF EXPERIMENTAL TRAVERSES

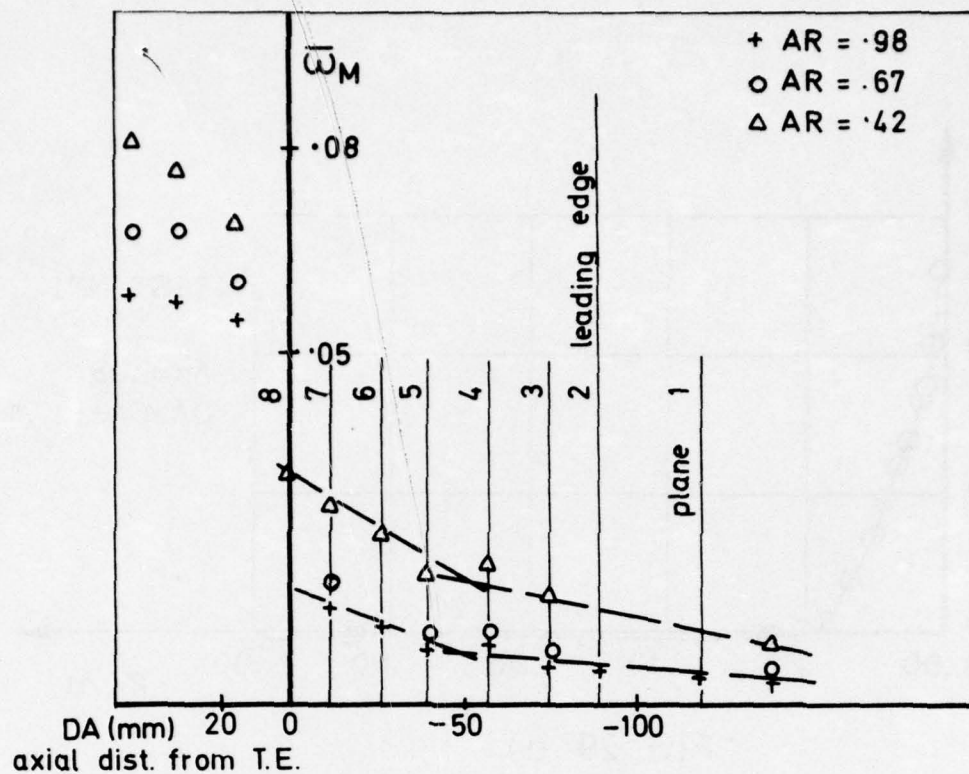


FIG. 28 a)

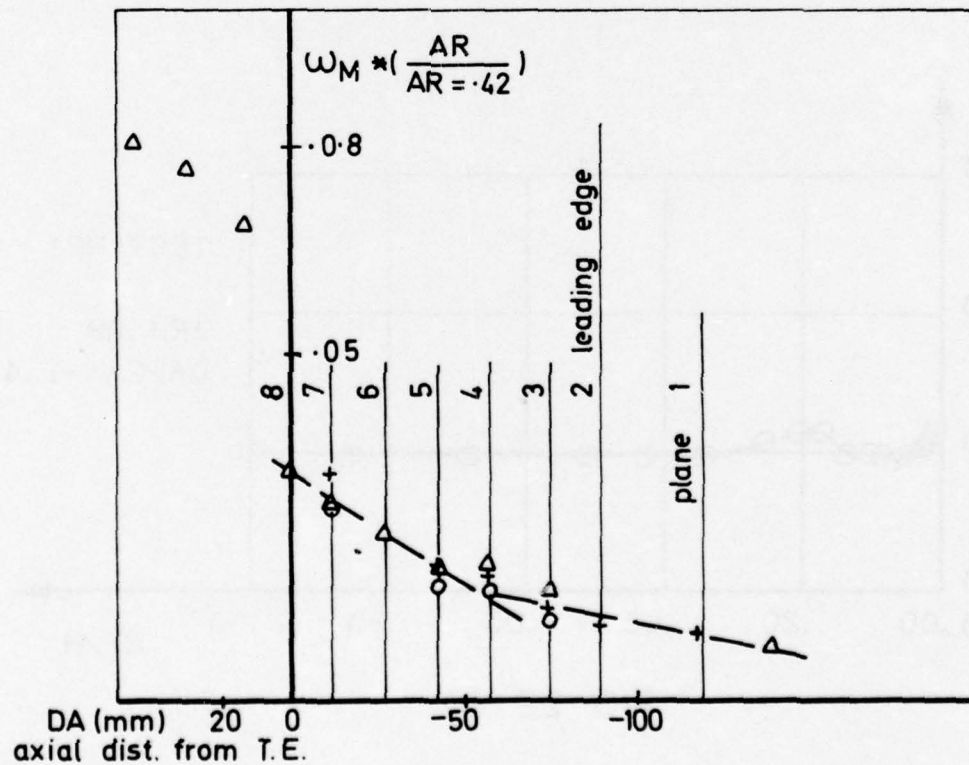


FIG. 28 b)

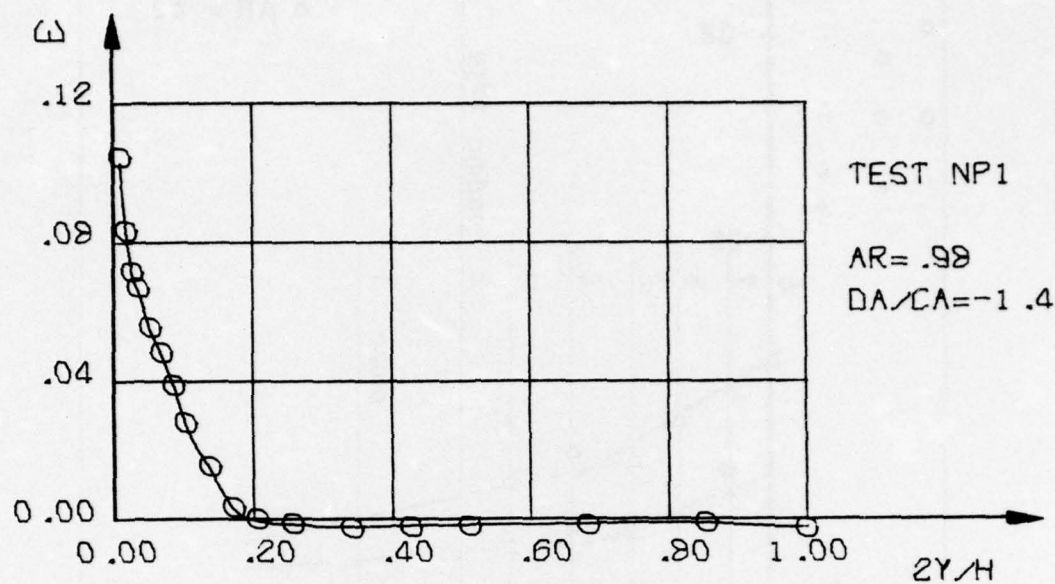


FIG. 29 a)

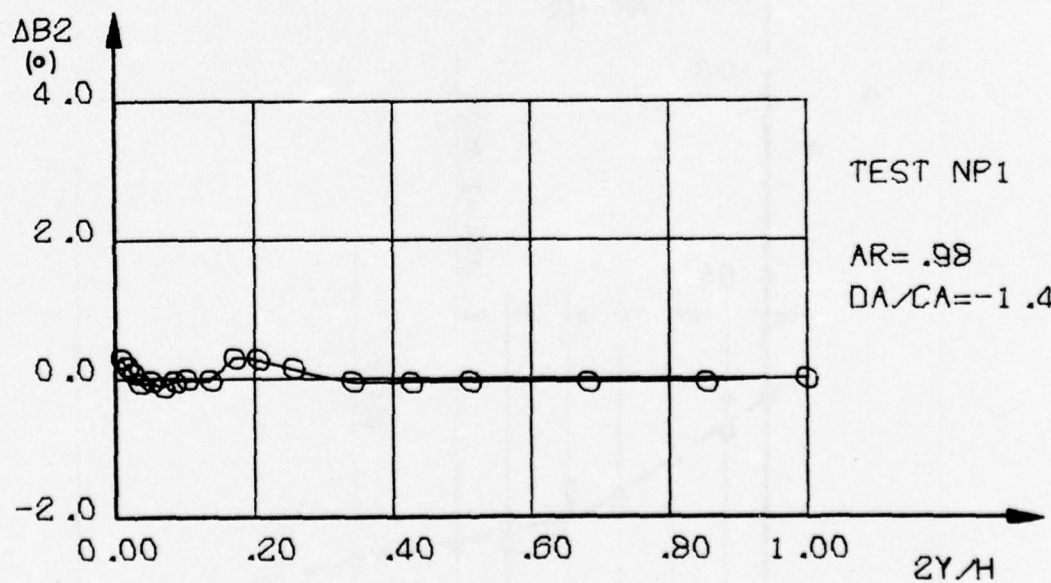


FIG. 29 b)

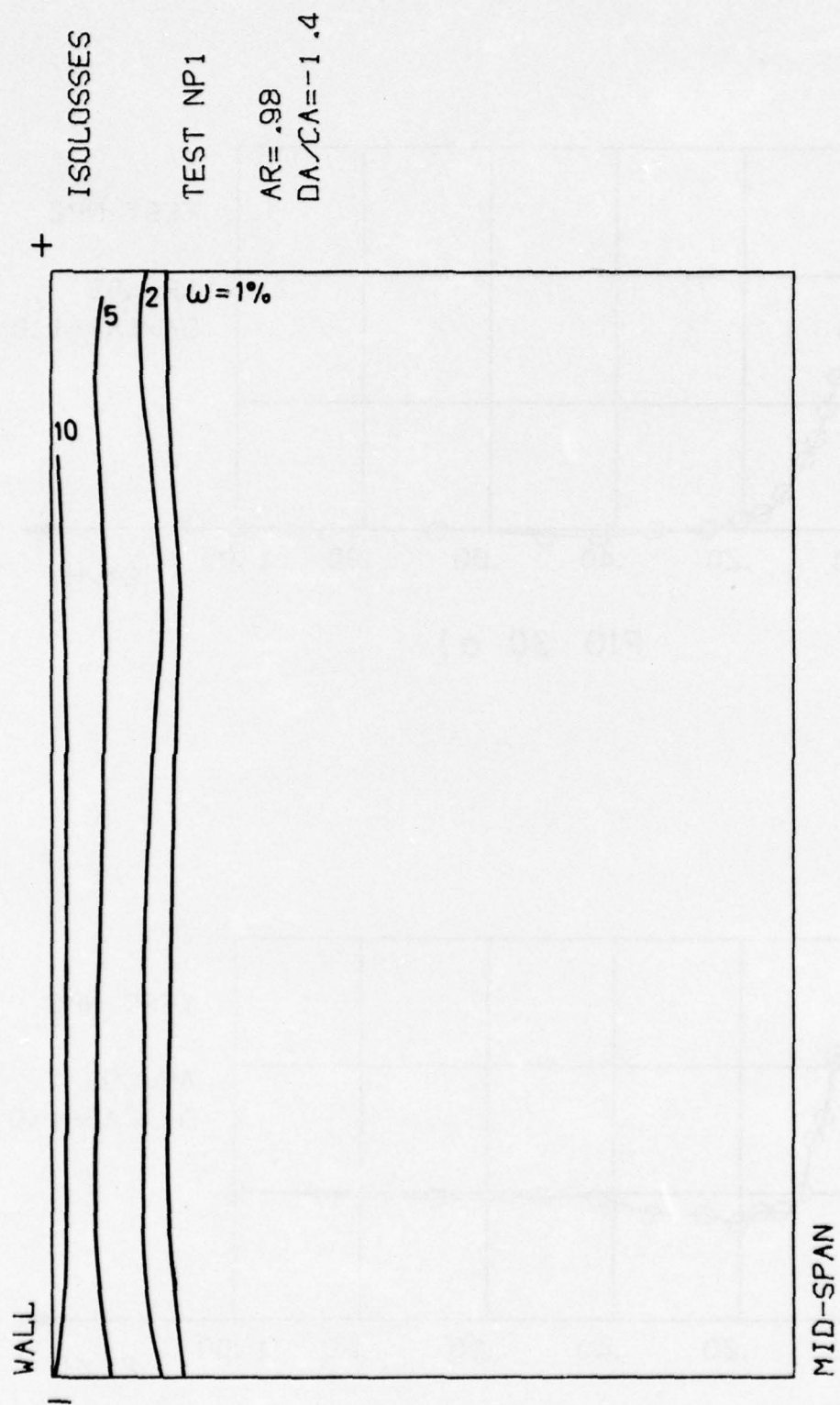


FIG. 29 c)

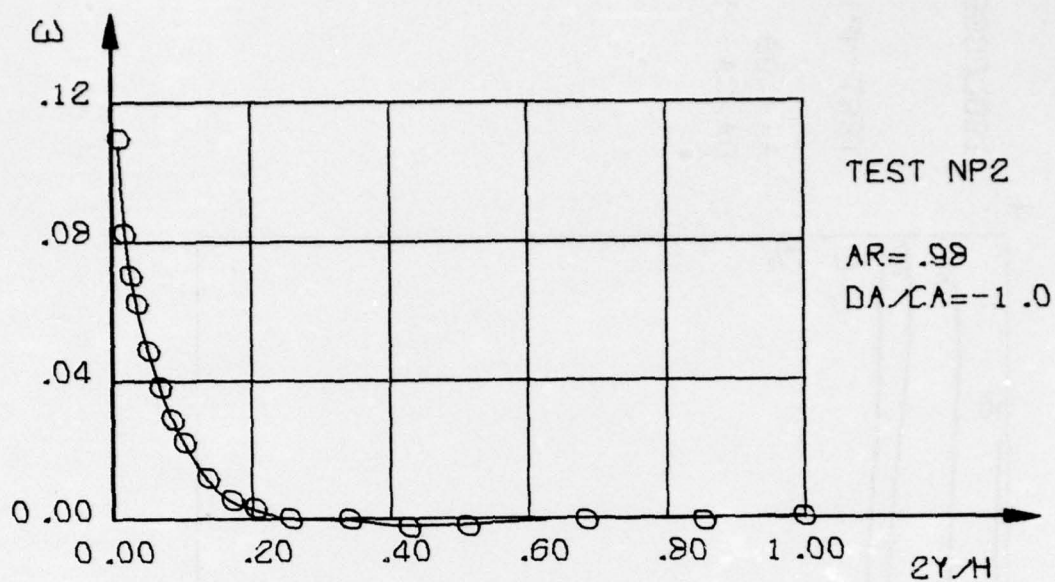


FIG. 30 a)

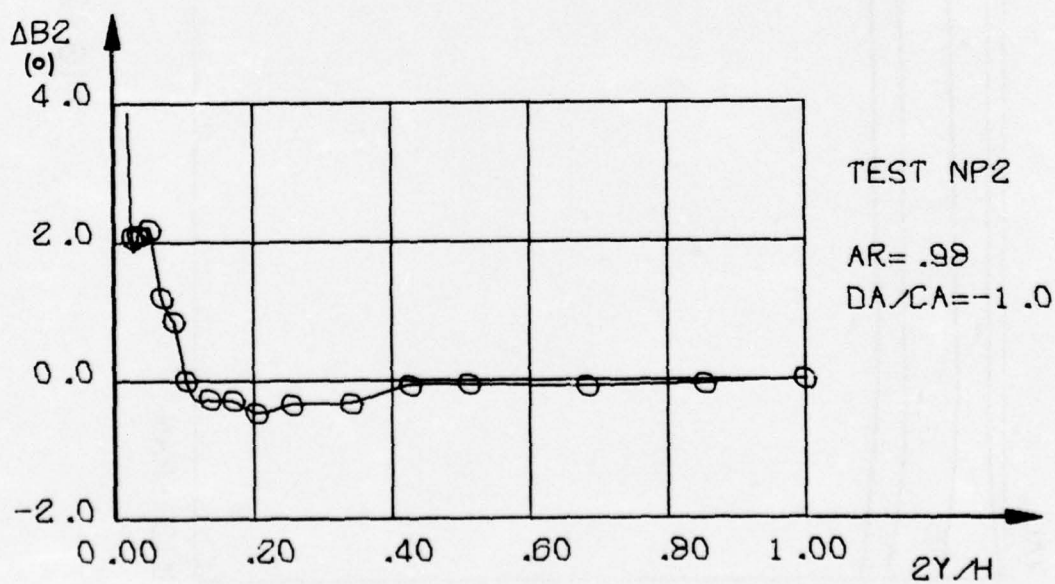


FIG. 30 b)

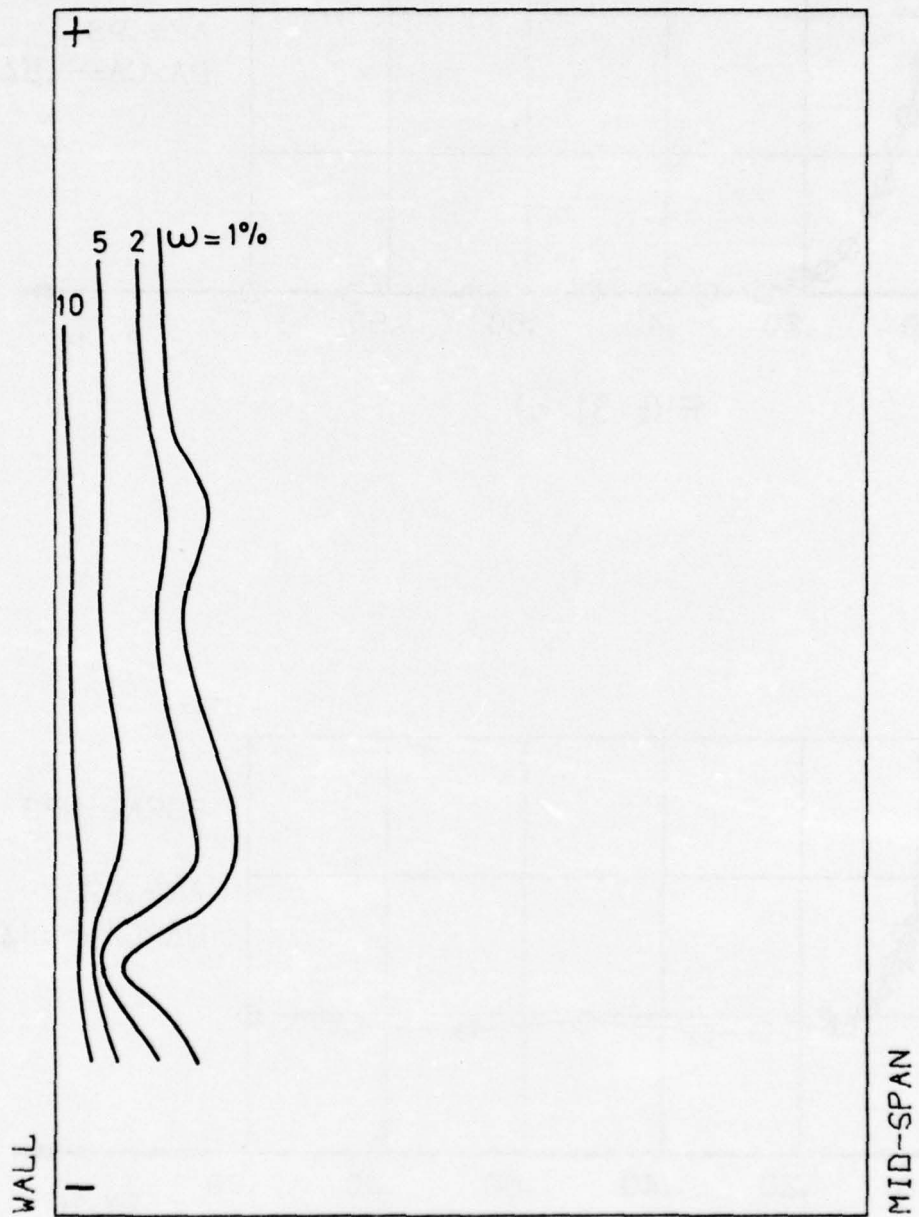


FIG. 30 c)

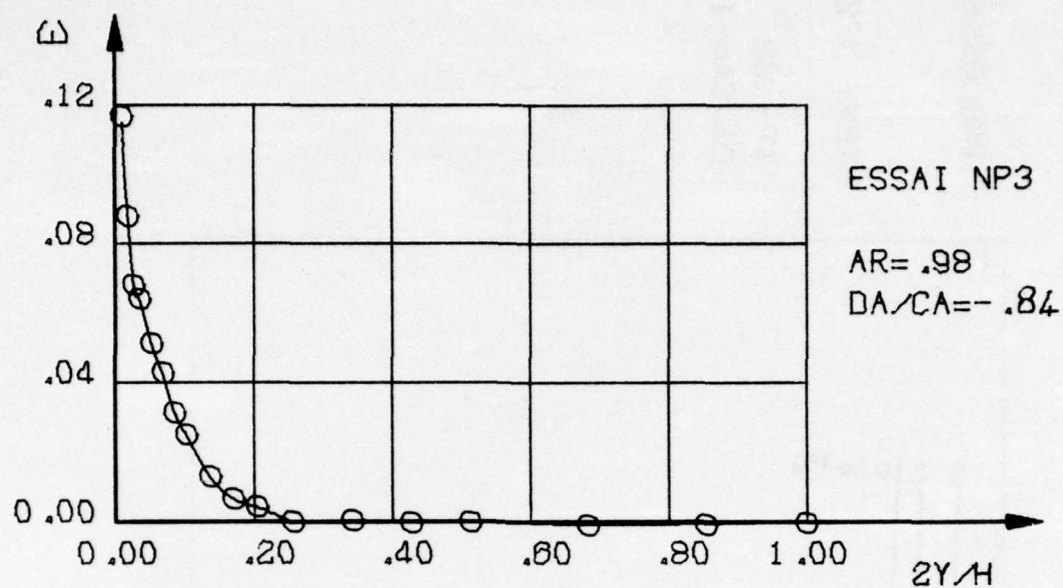


FIG 31 a)

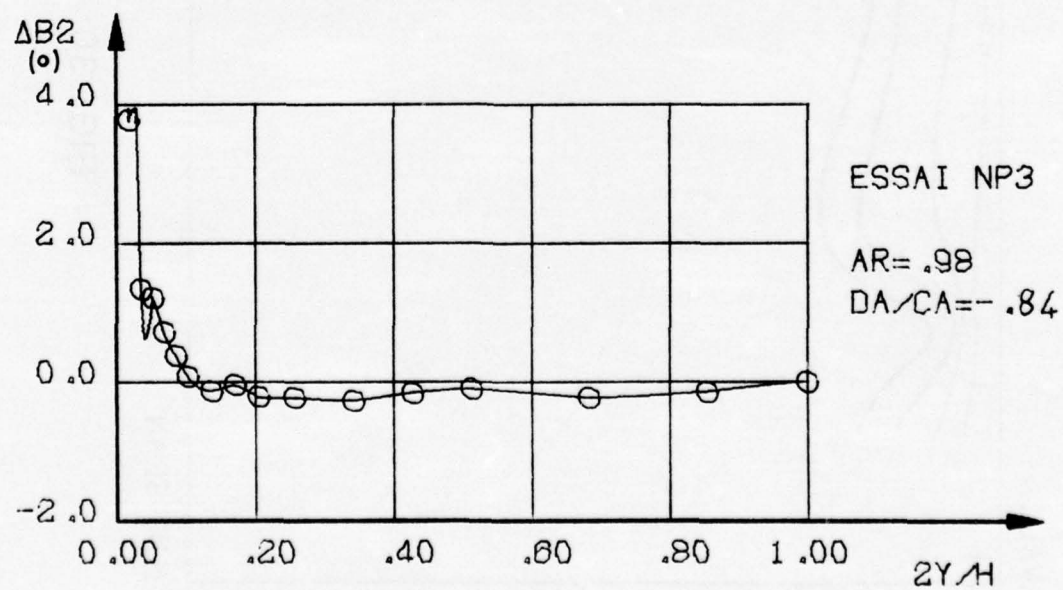


FIG 31 b)

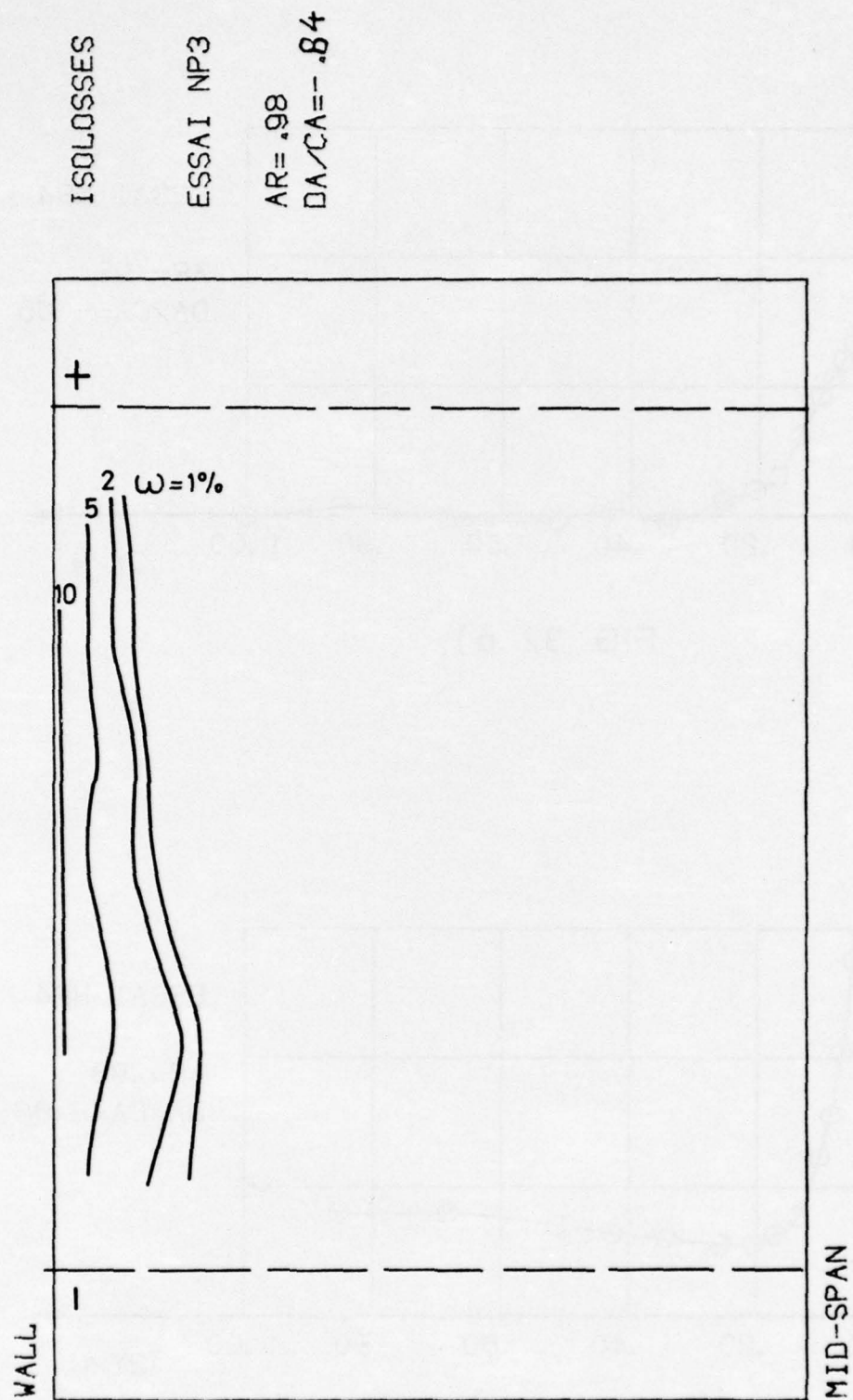


FIG. 31 c)

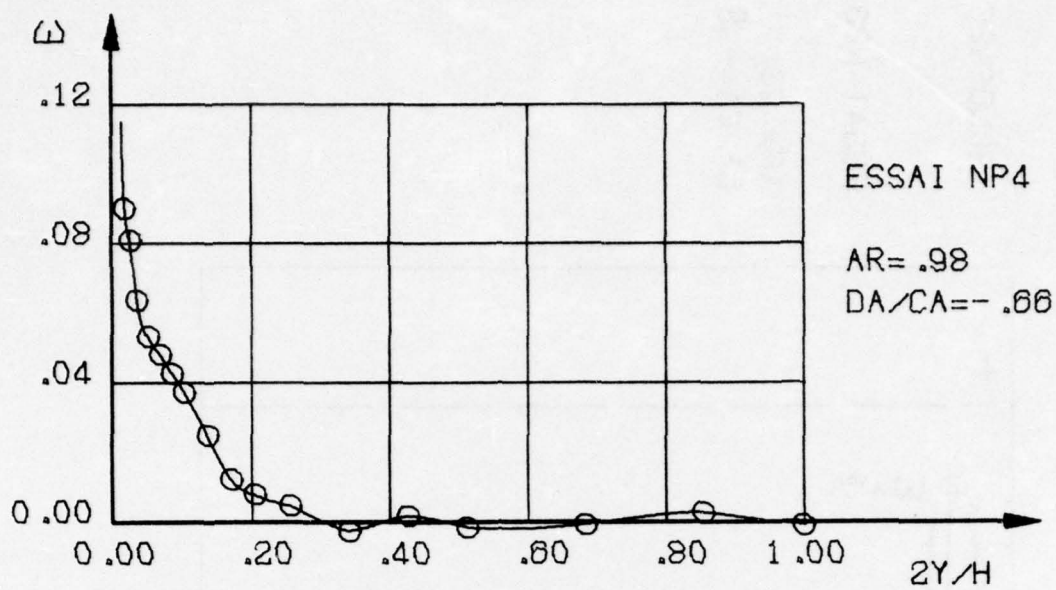


FIG. 32 a)

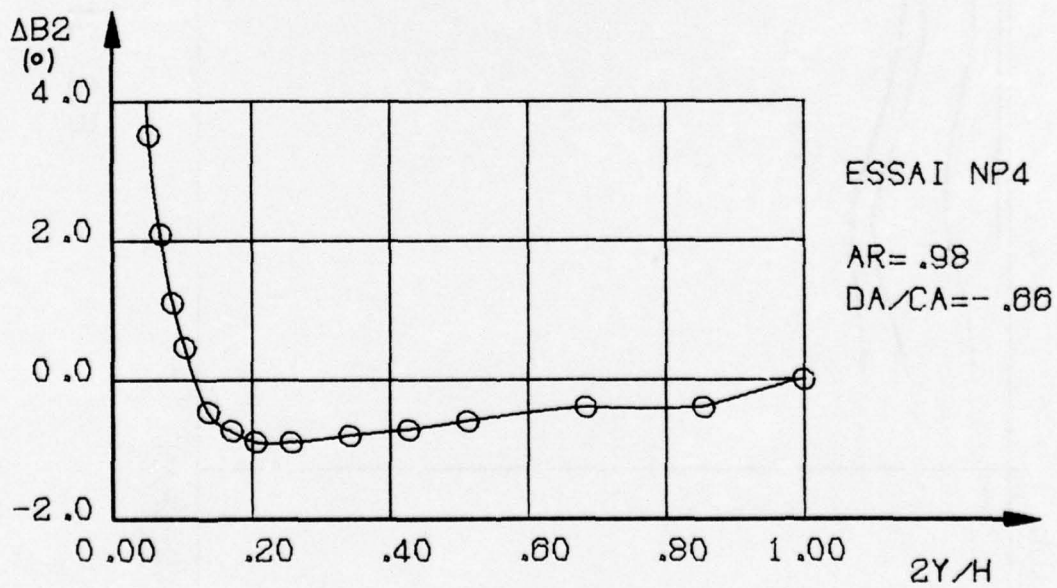


FIG. 32 b)

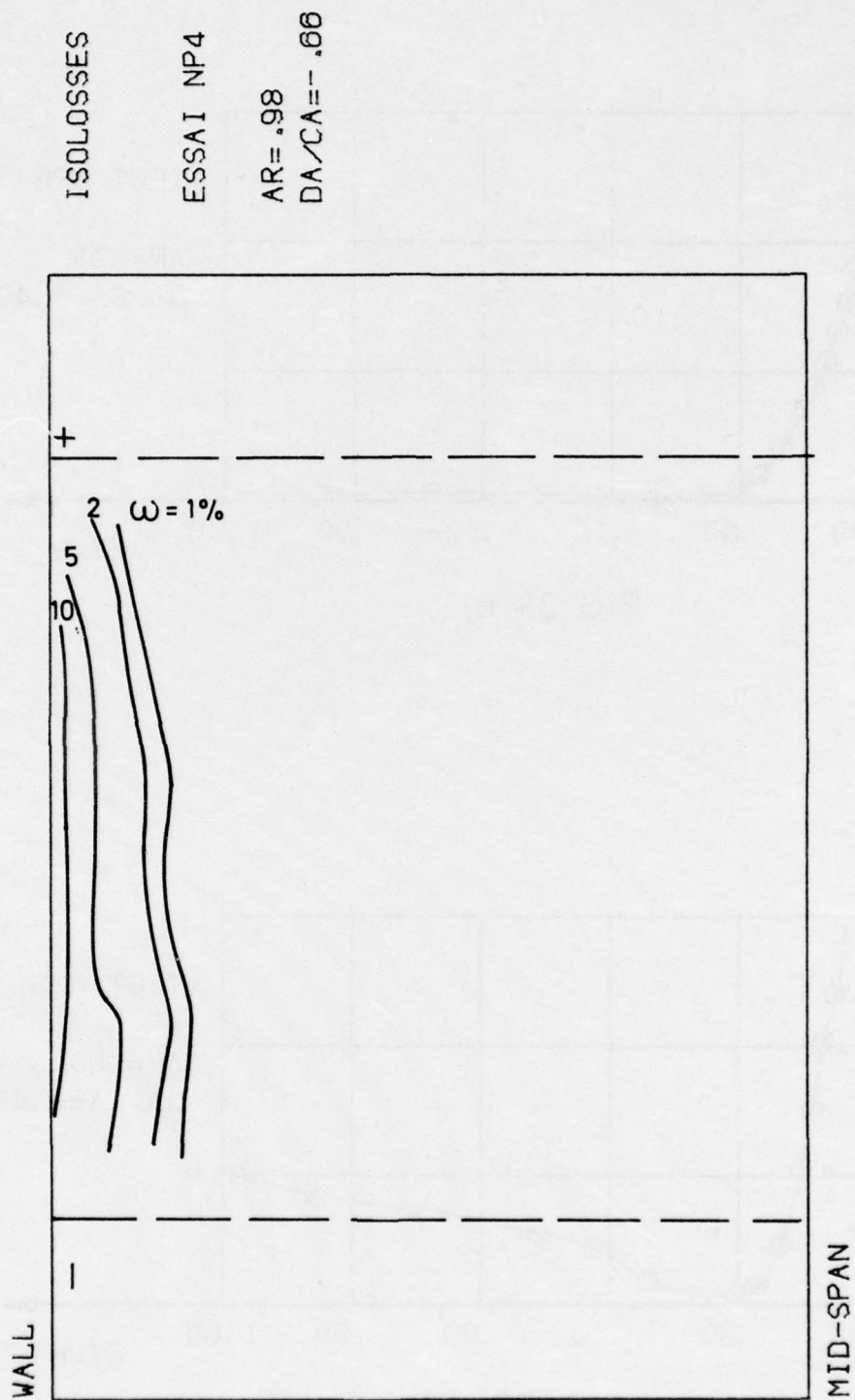


FIG. 32 c)

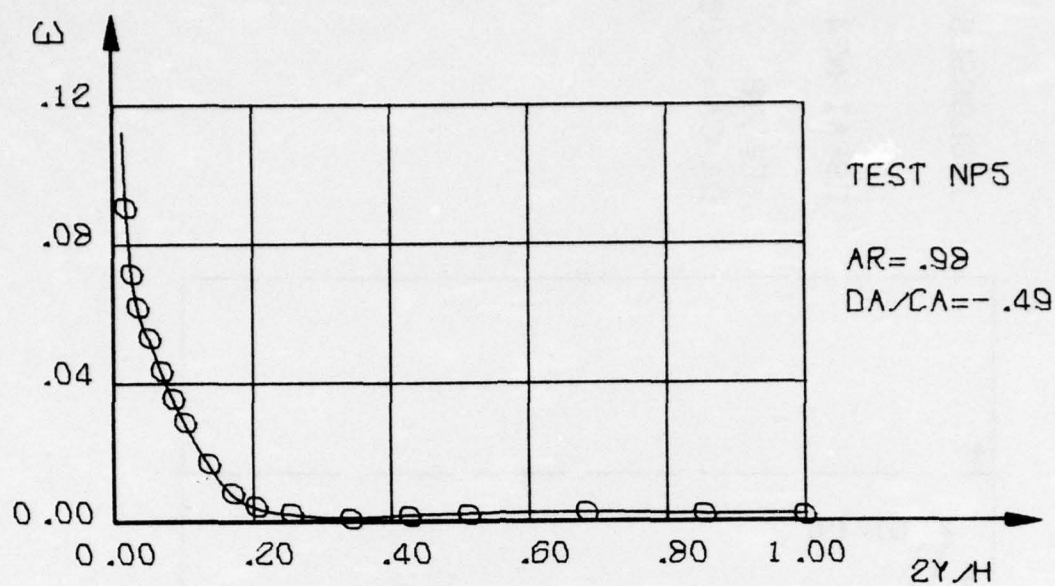


FIG. 33 a)

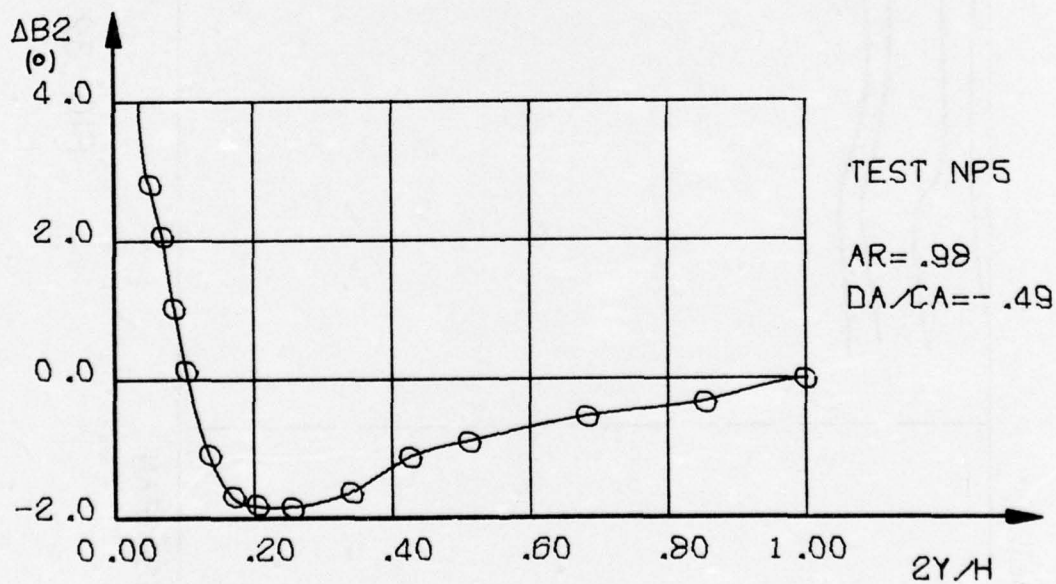


FIG. 33 b)

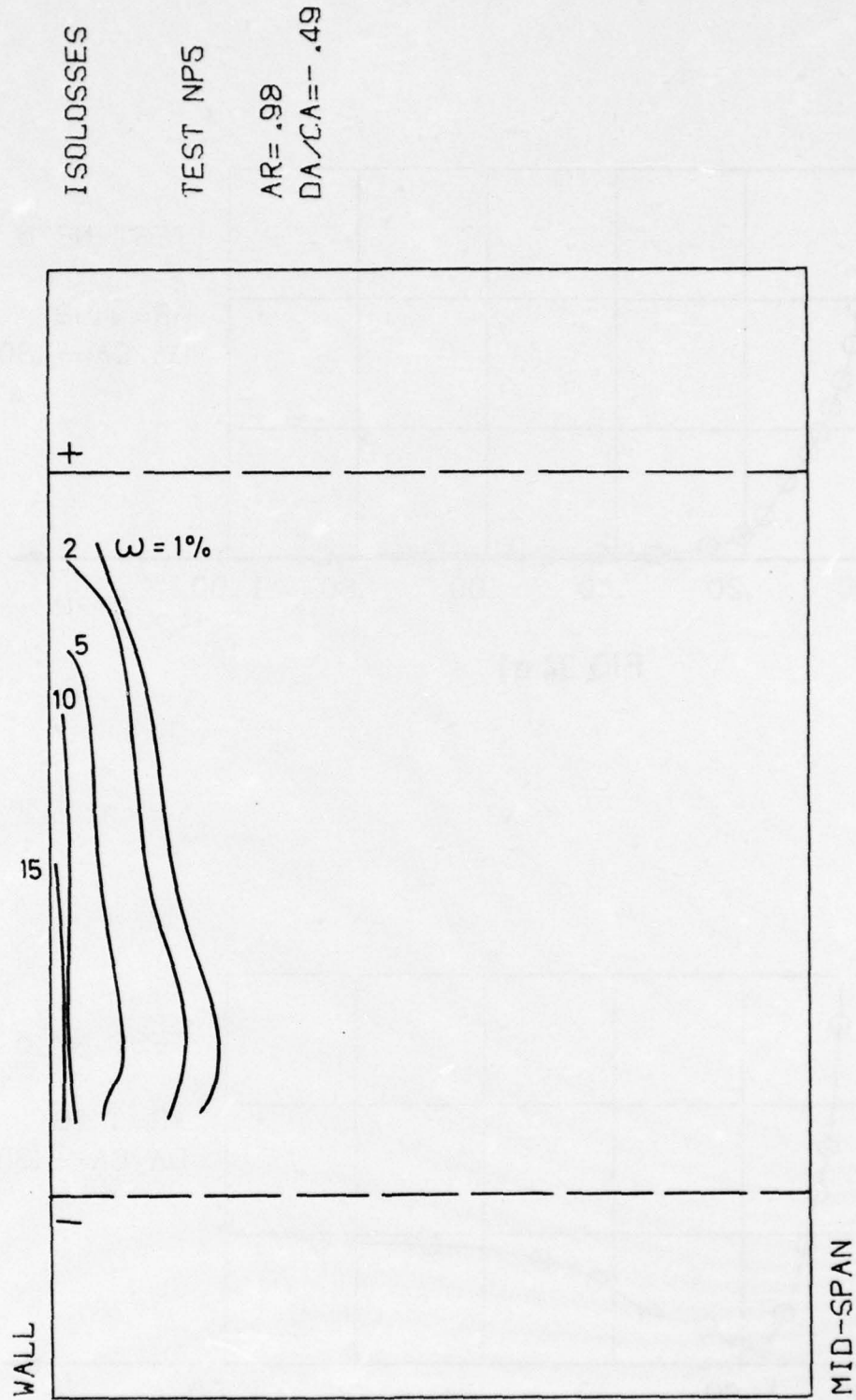


FIG. 33 c)

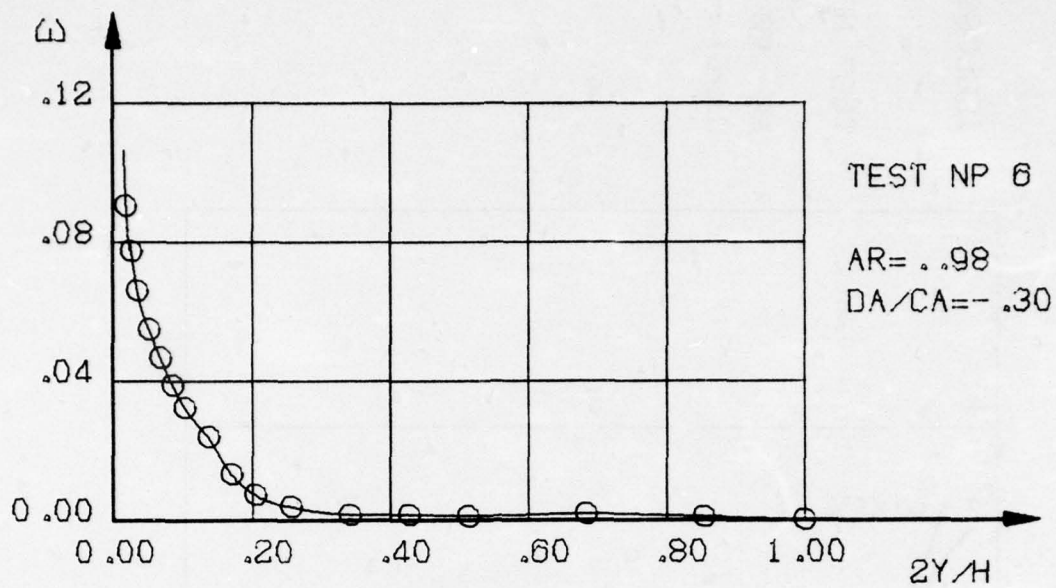


FIG 34 a)

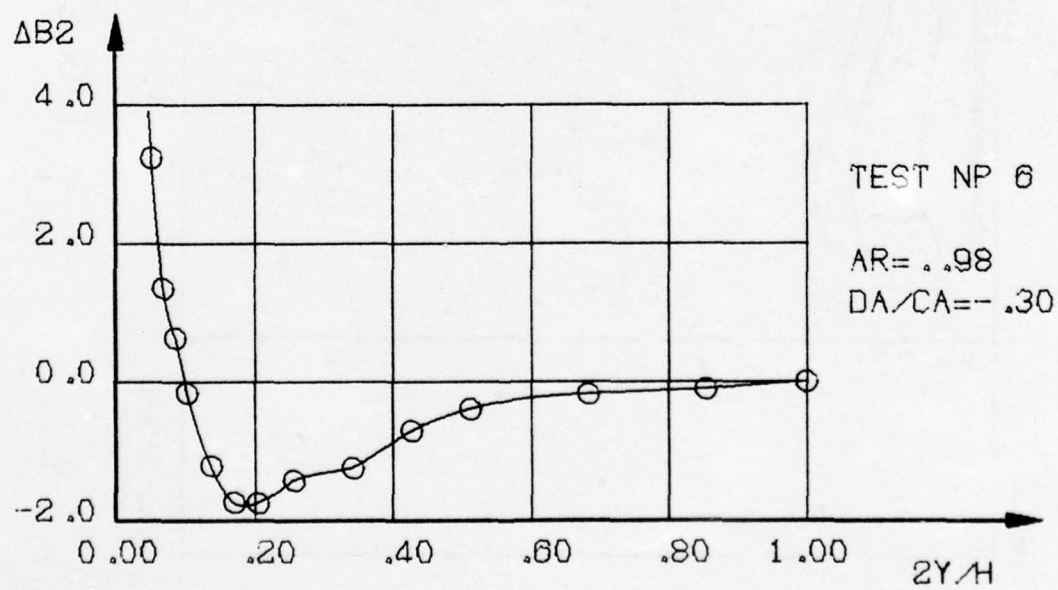


FIG 34 b)

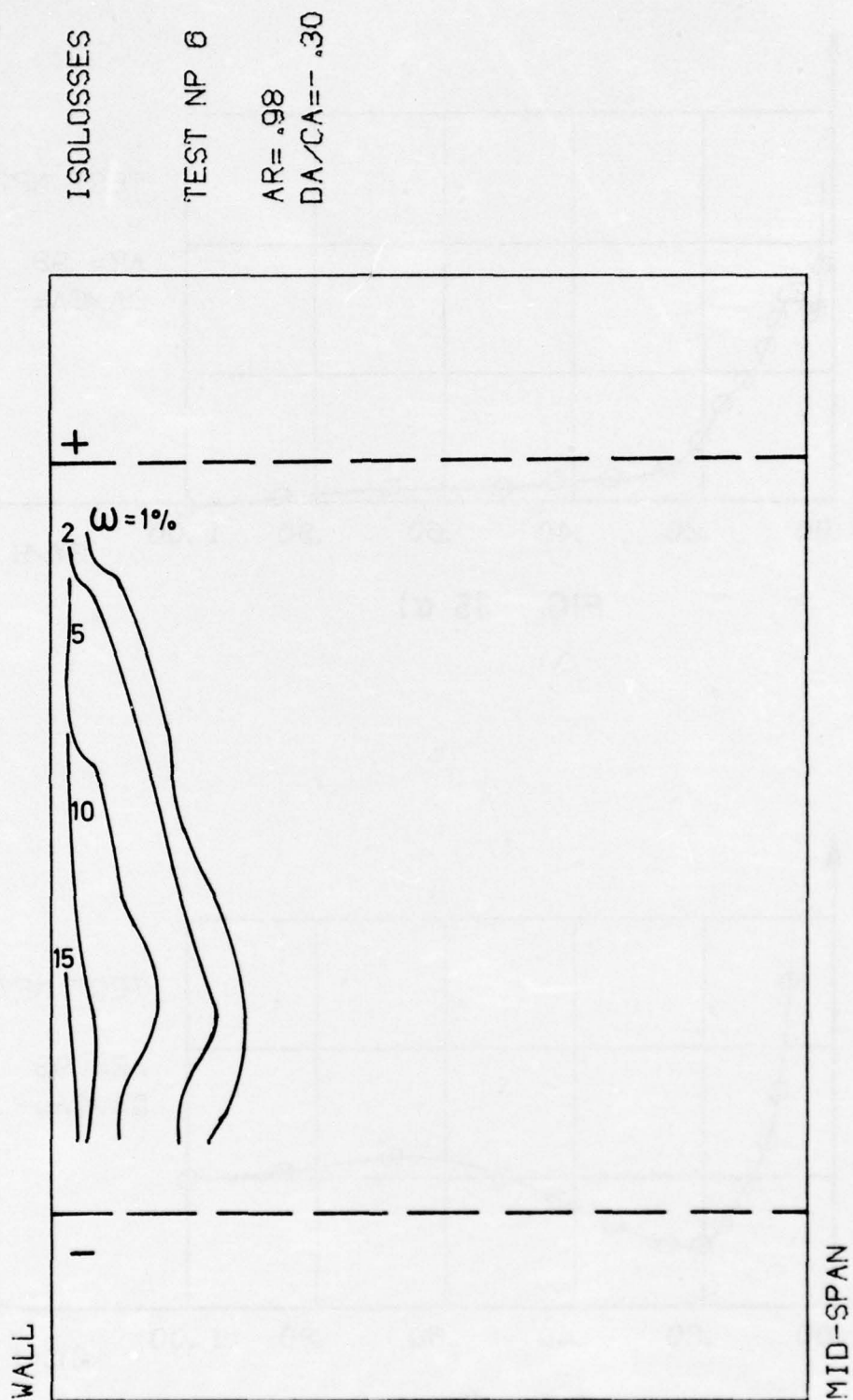


FIG. 34c)

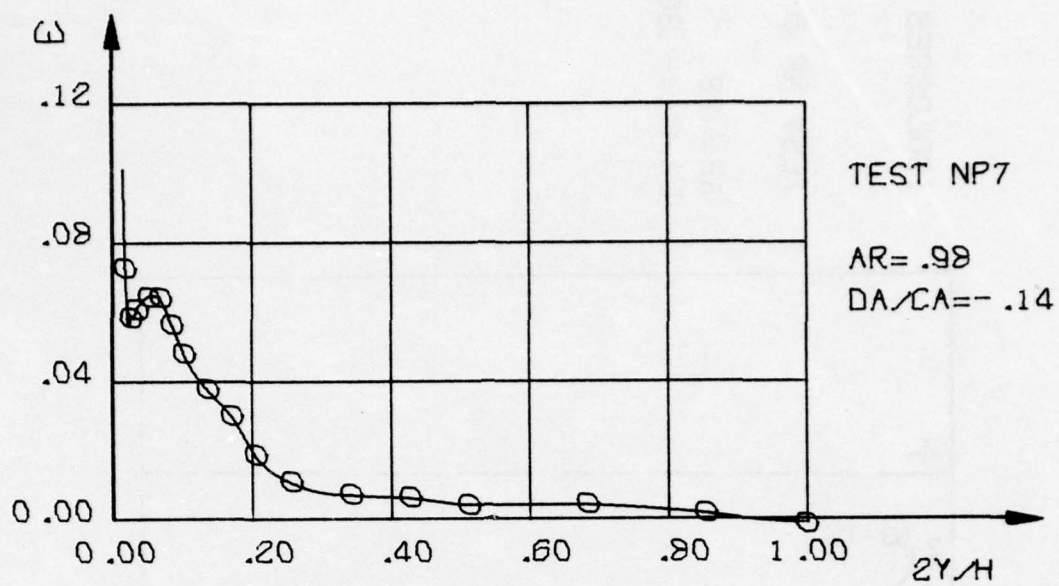


FIG. 35 a)

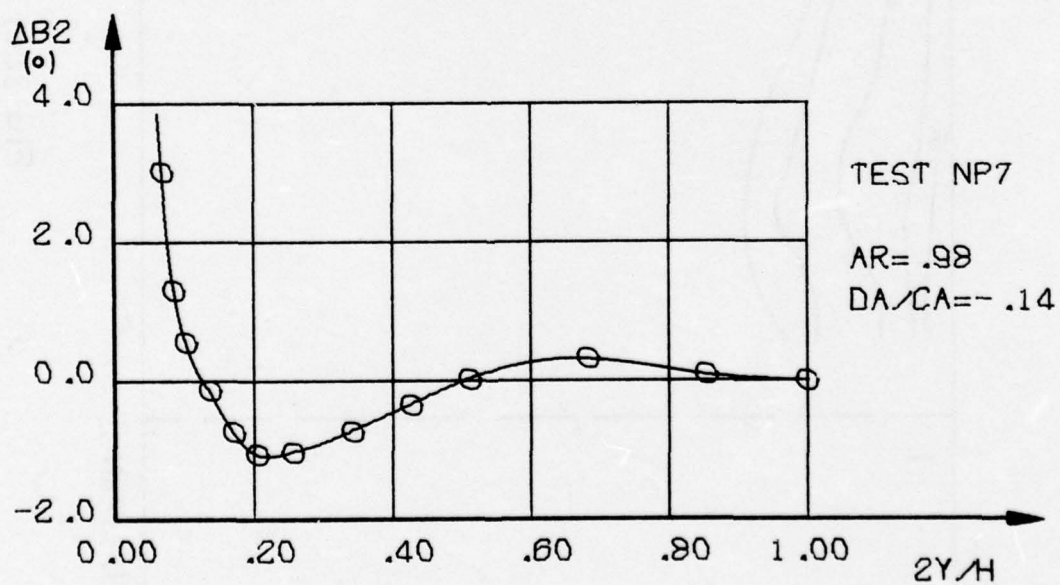


FIG 35 b)

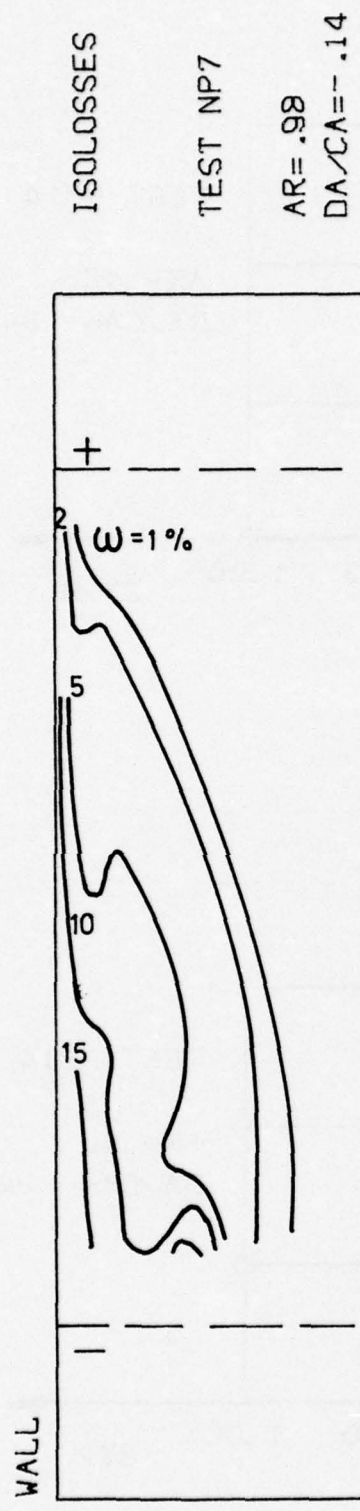


FIG. 35c)

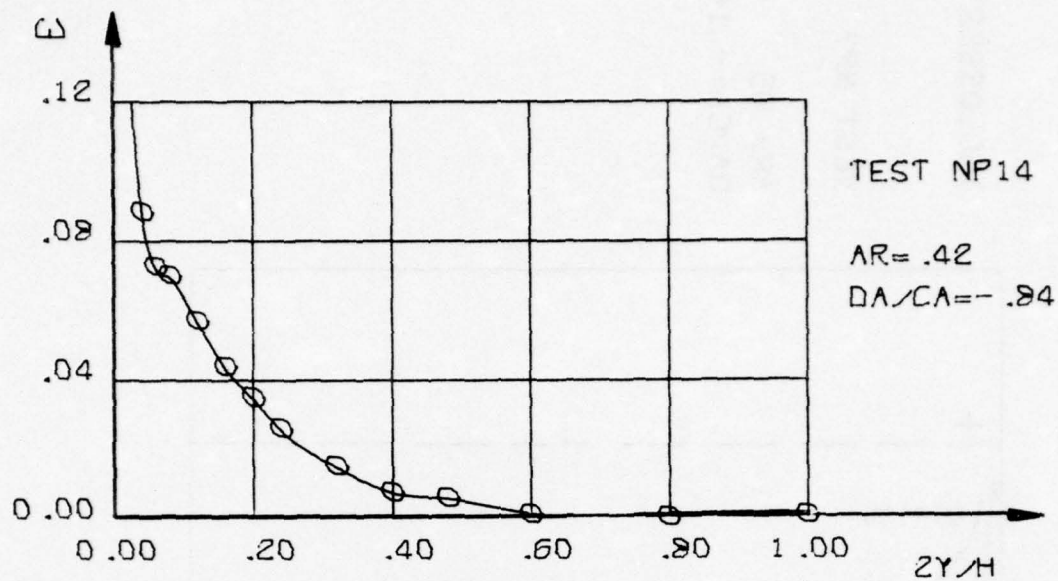


FIG. 36 a)

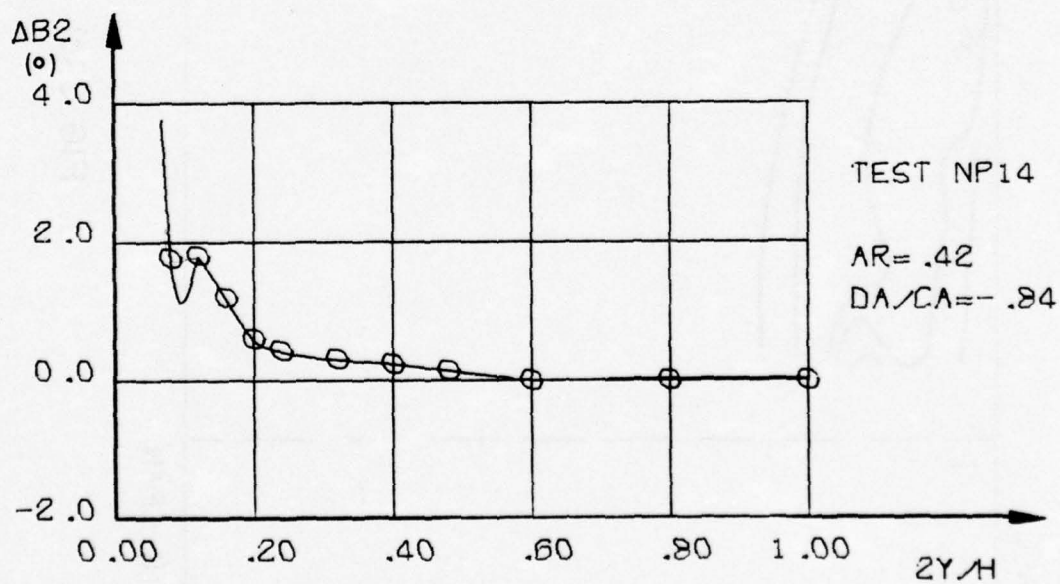


FIG 36 b)

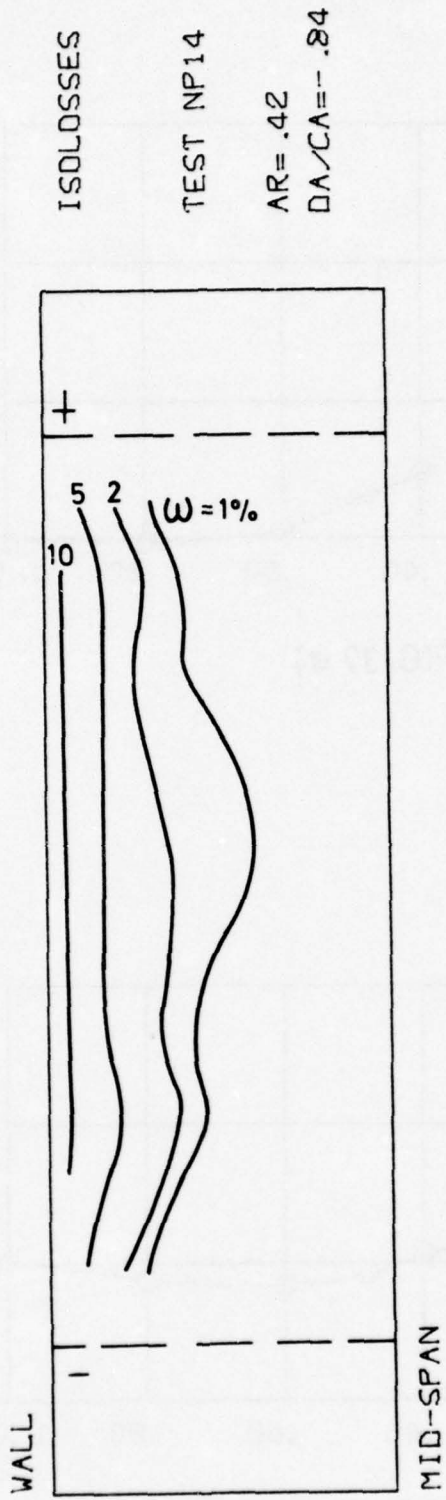


FIG. 36 c)

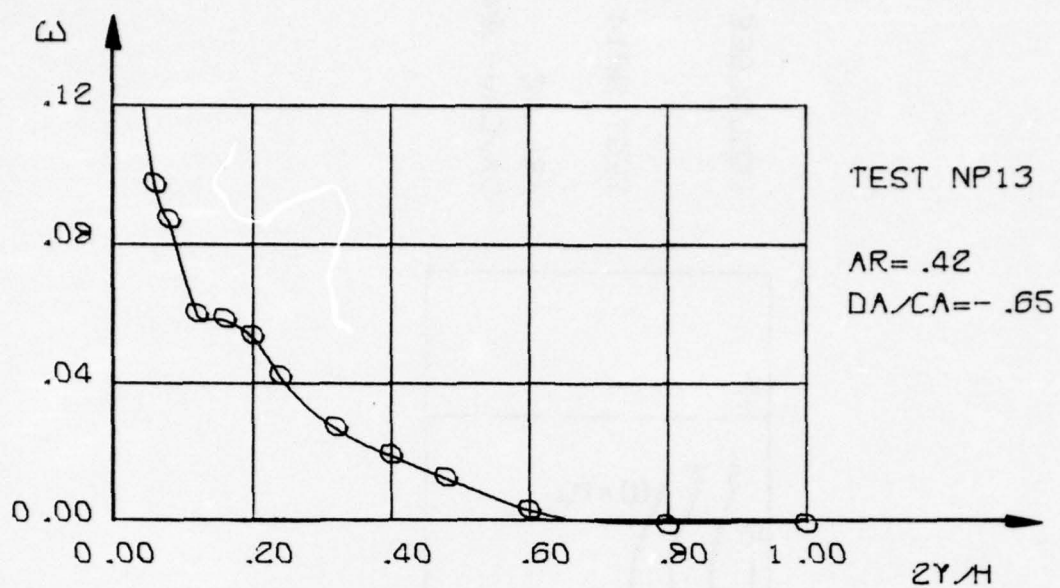


FIG. 37 a)

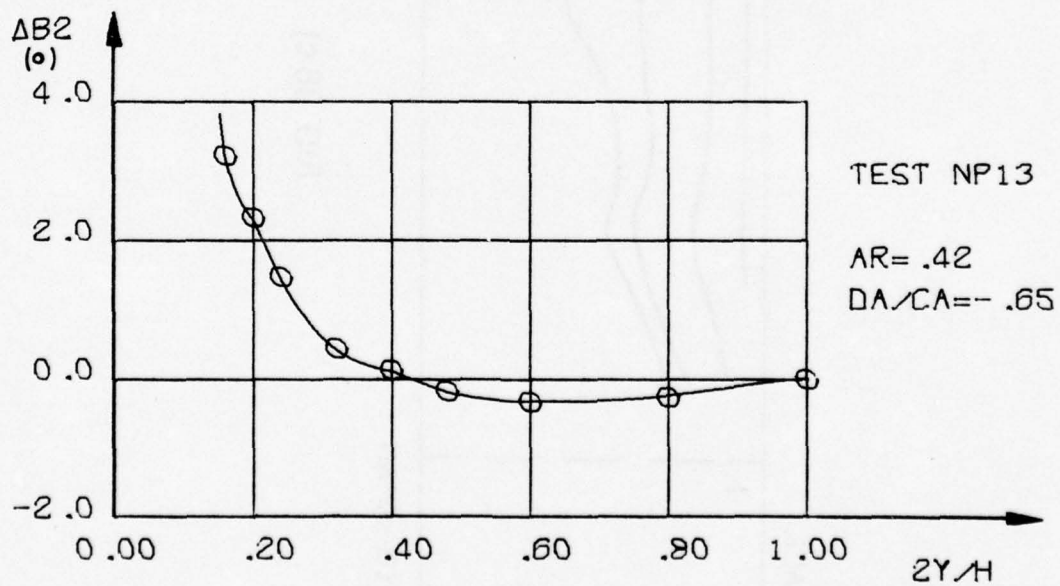


FIG. 37 b)

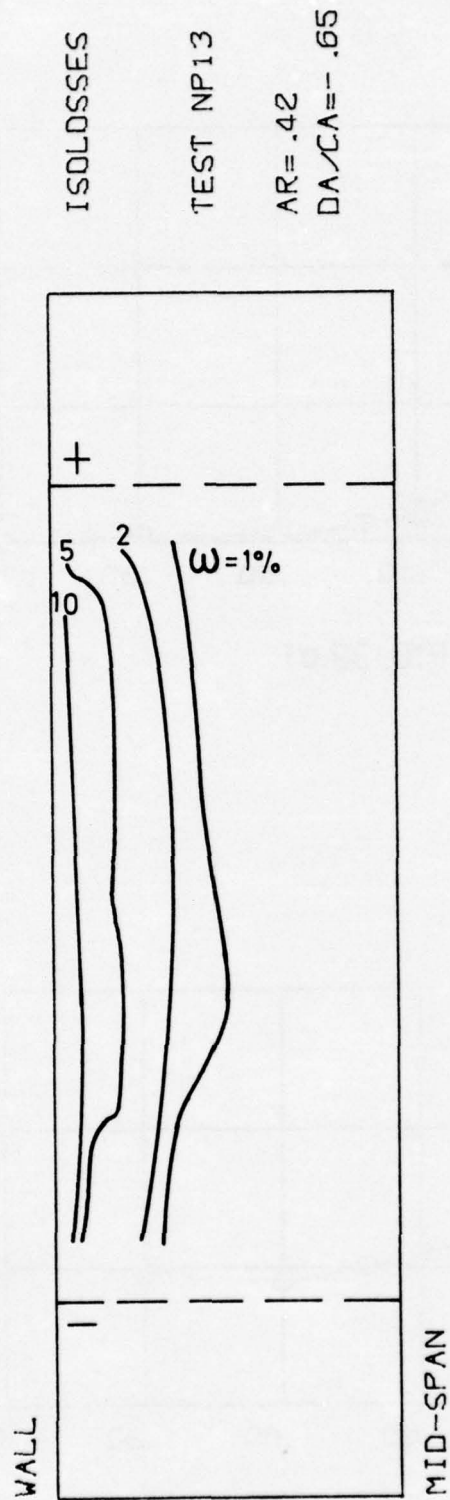


FIG 37 c)

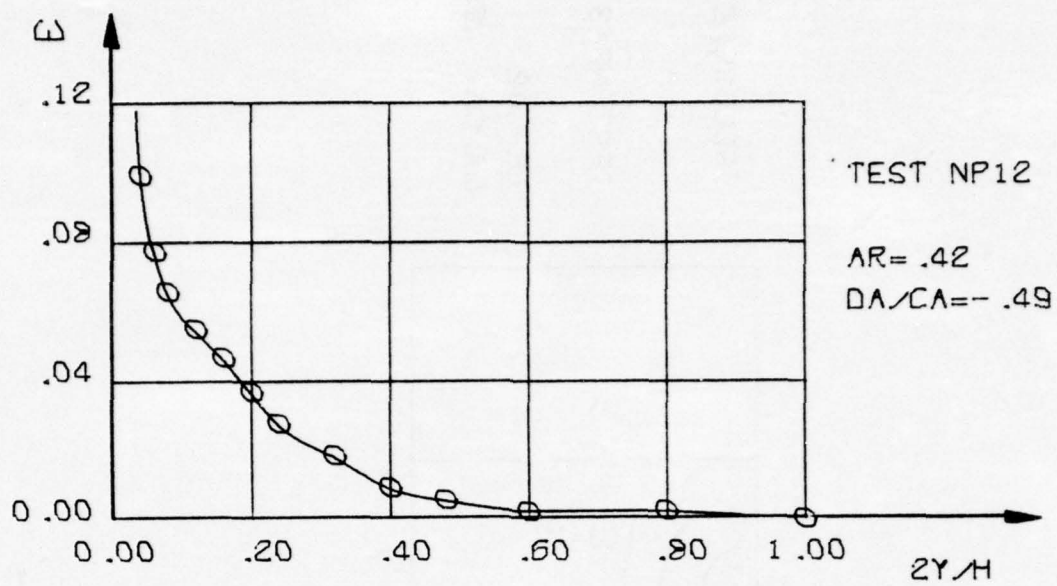


FIG. 38 a)

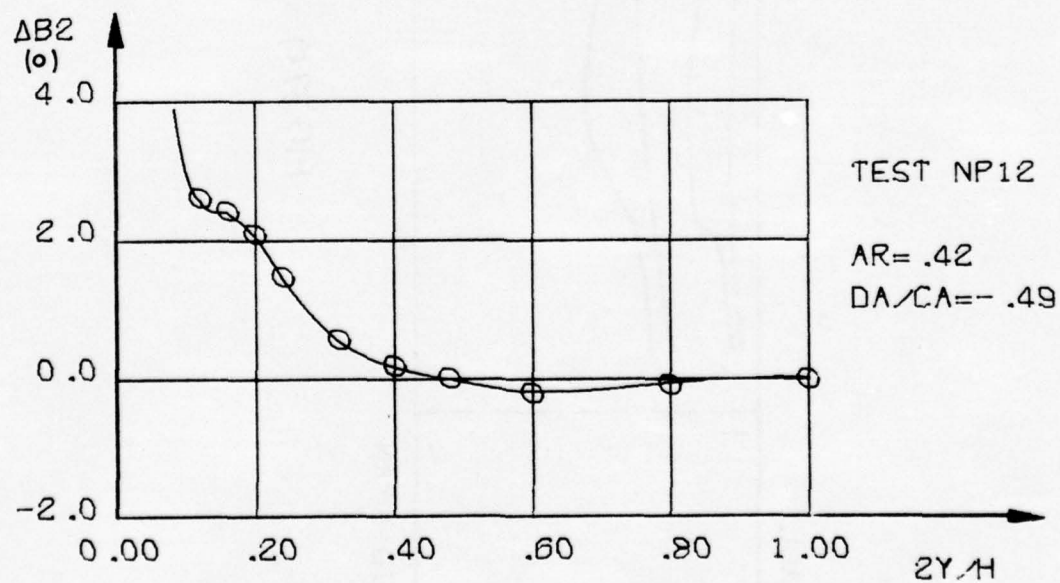


FIG. 38 b)

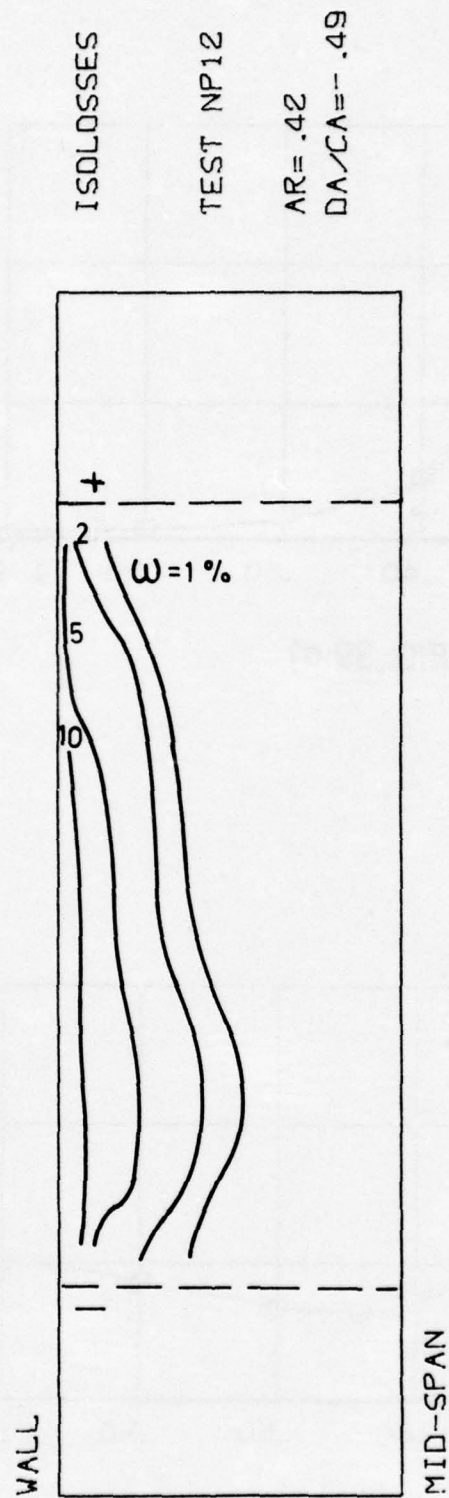


FIG. 38 c)

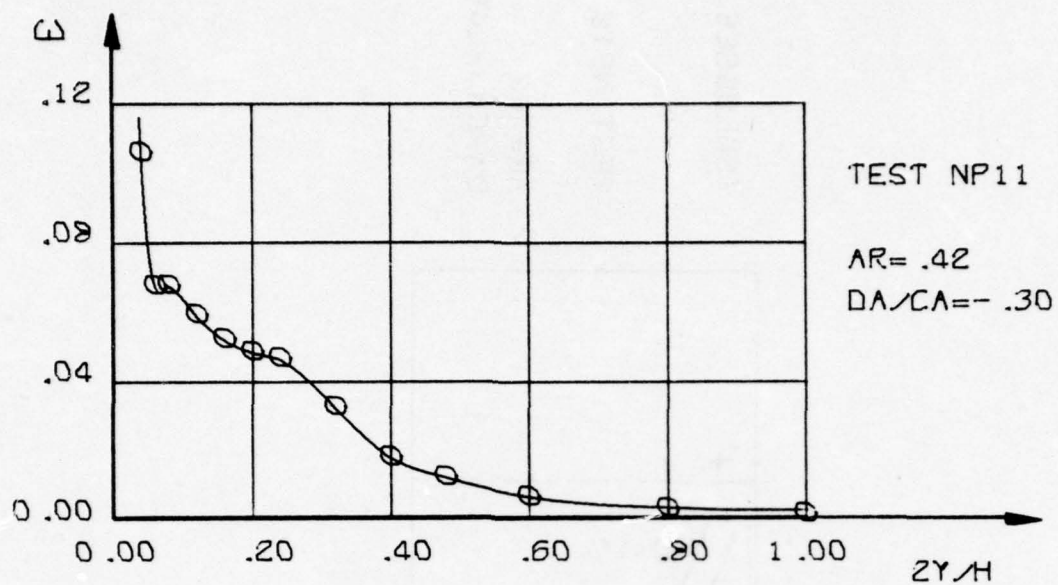


FIG. 39 a)

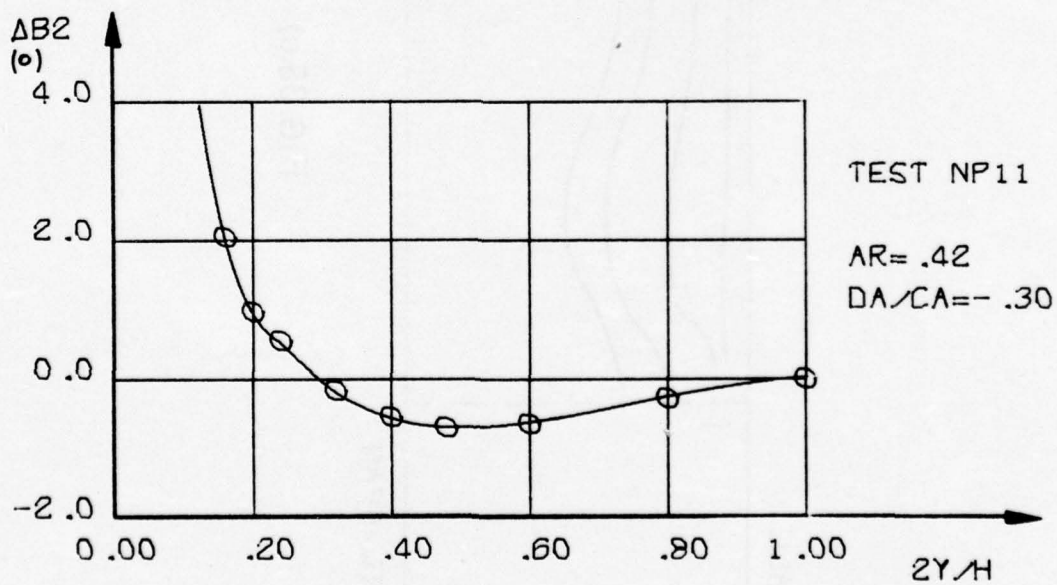


FIG. 39 b)

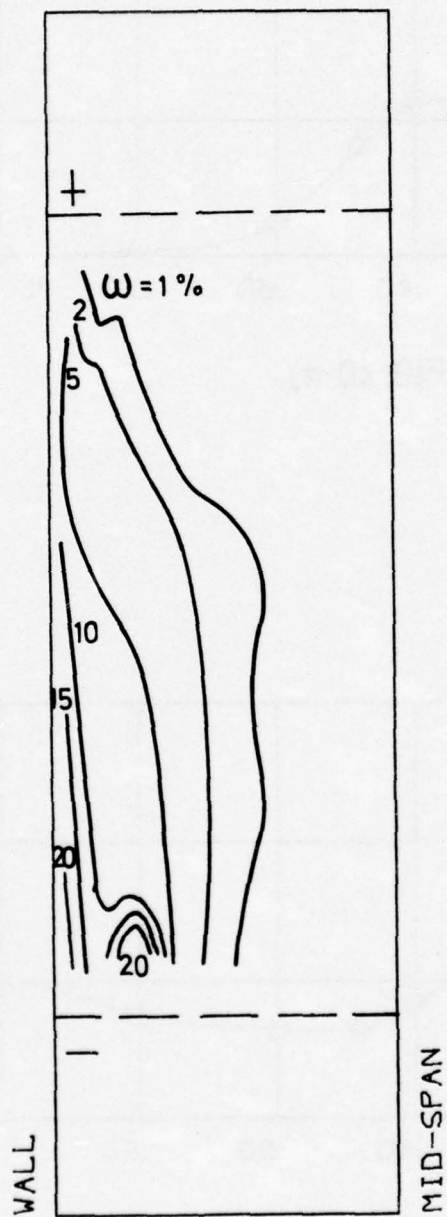


FIG. 39 c)

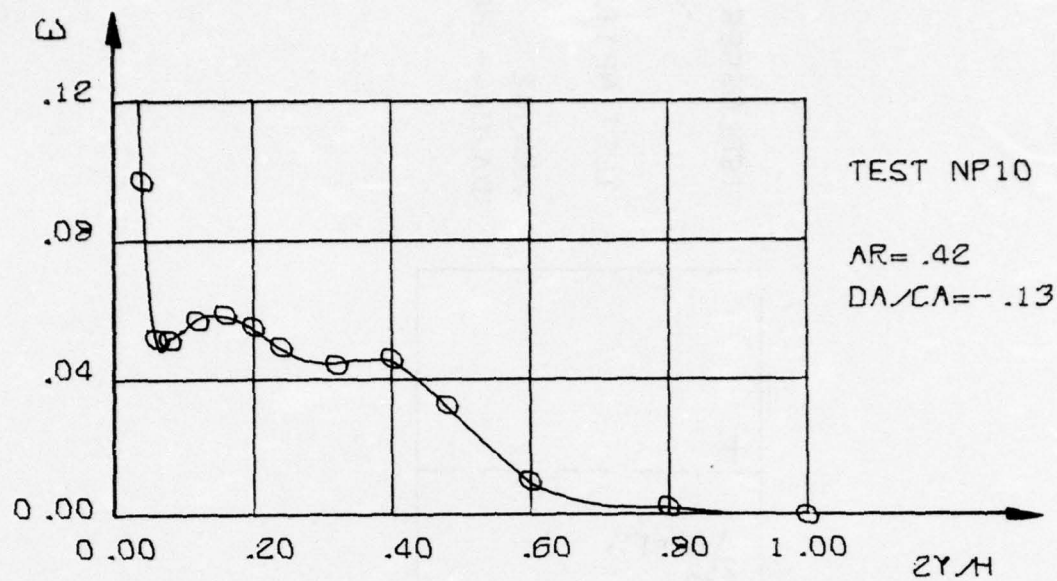


FIG. 40 a)

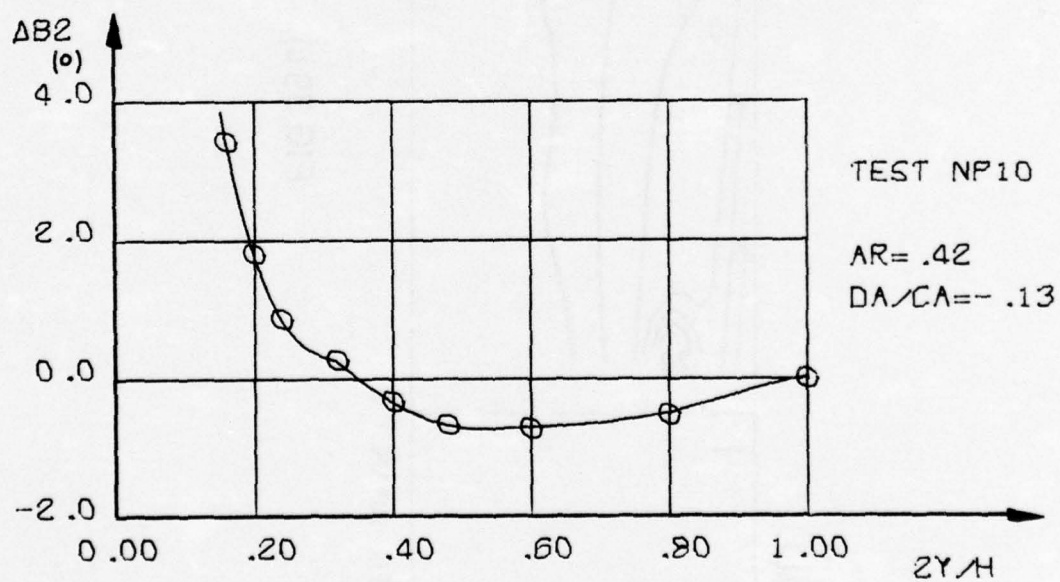


FIG. 40 b)

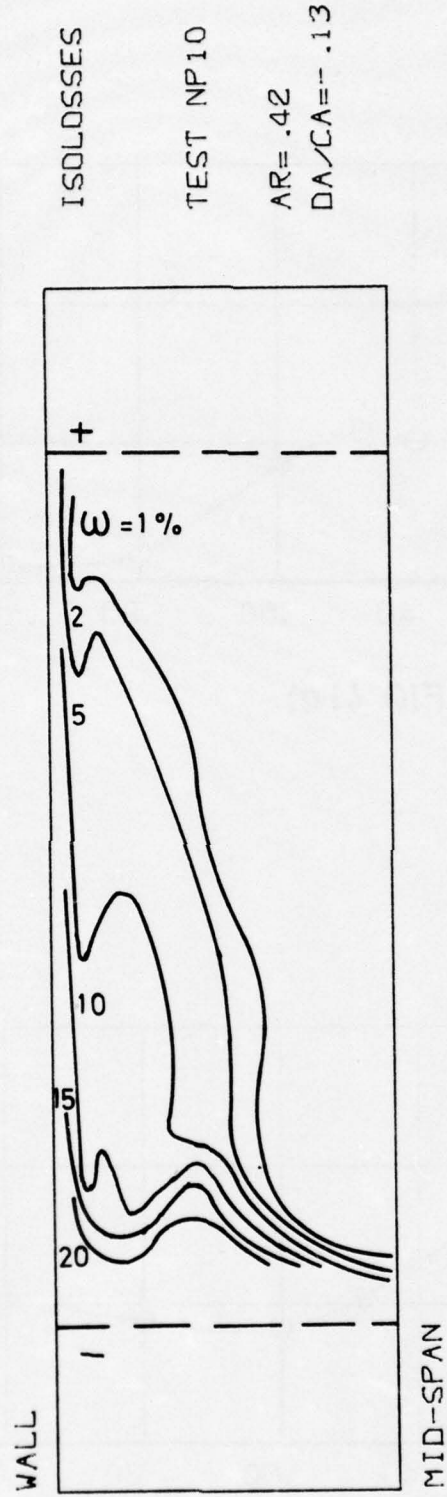


FIG. 40 c)

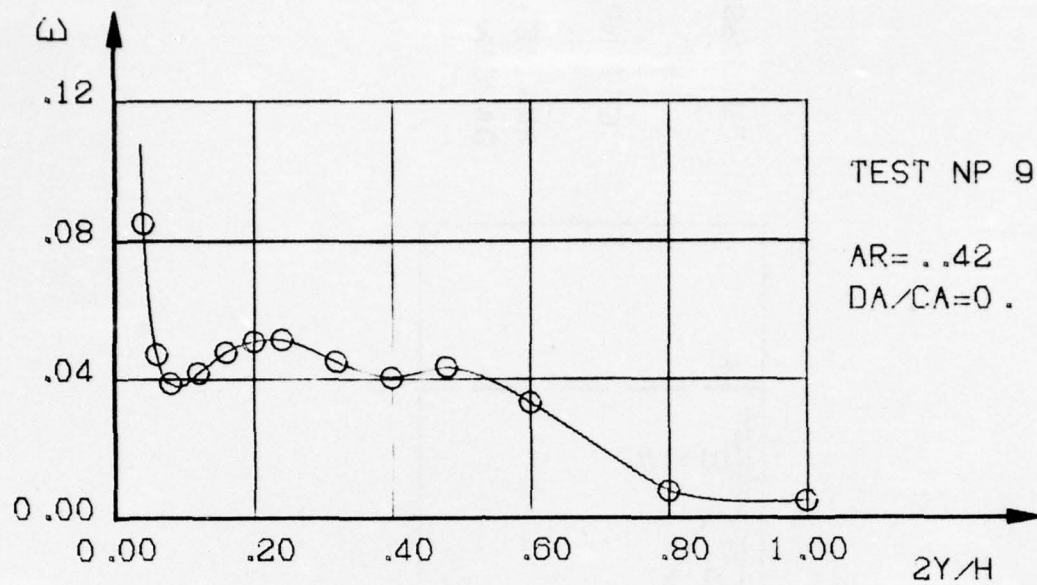


FIG. 41 a)

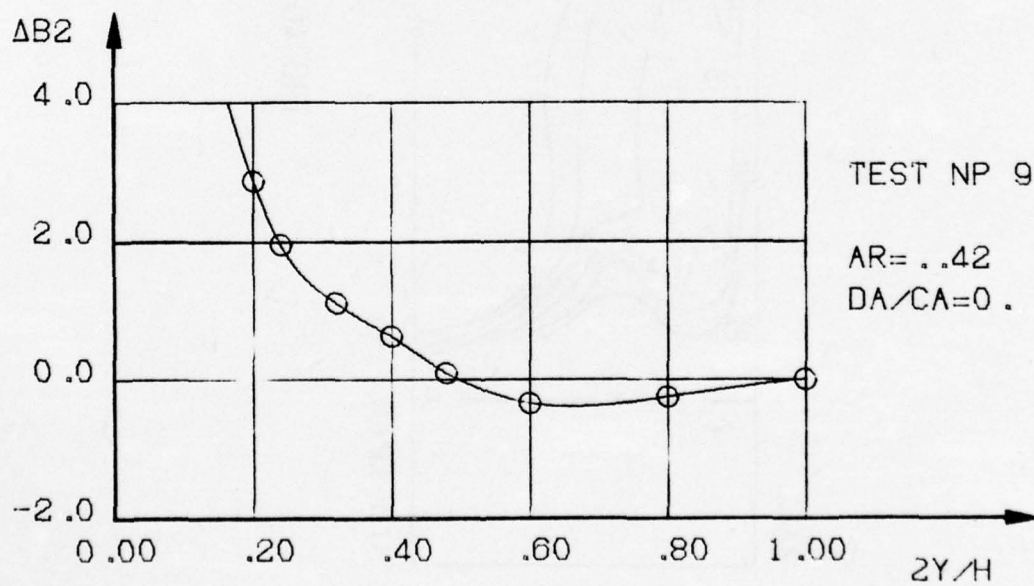


FIG. 41 b)

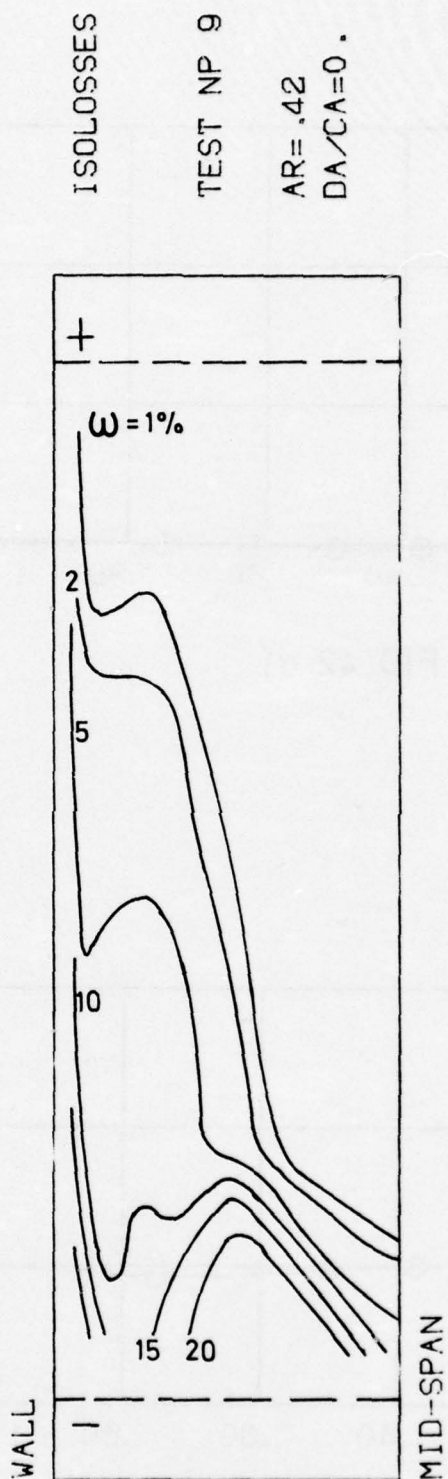


FIG. 41c)

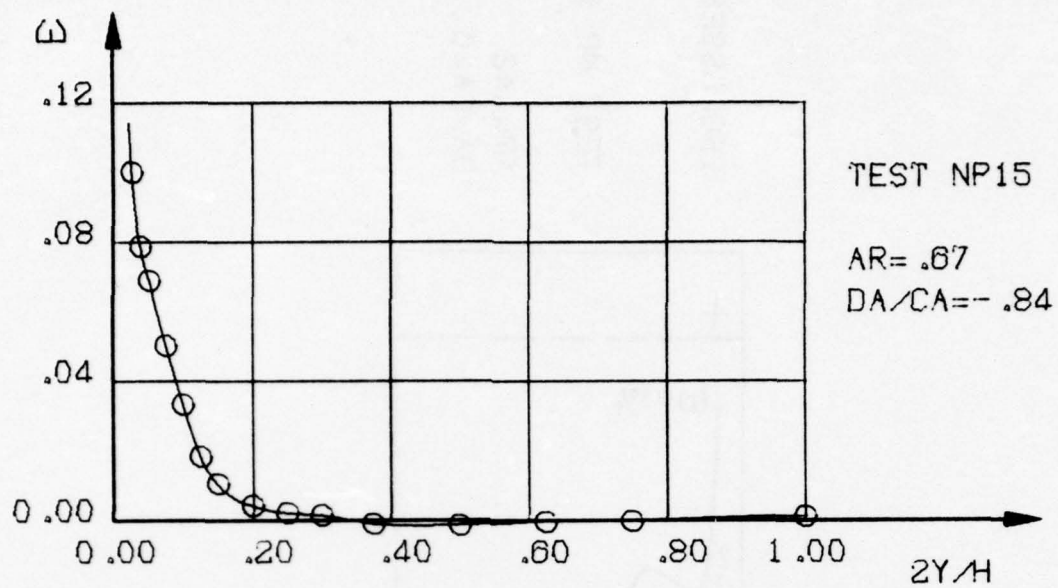


FIG. 42 a)

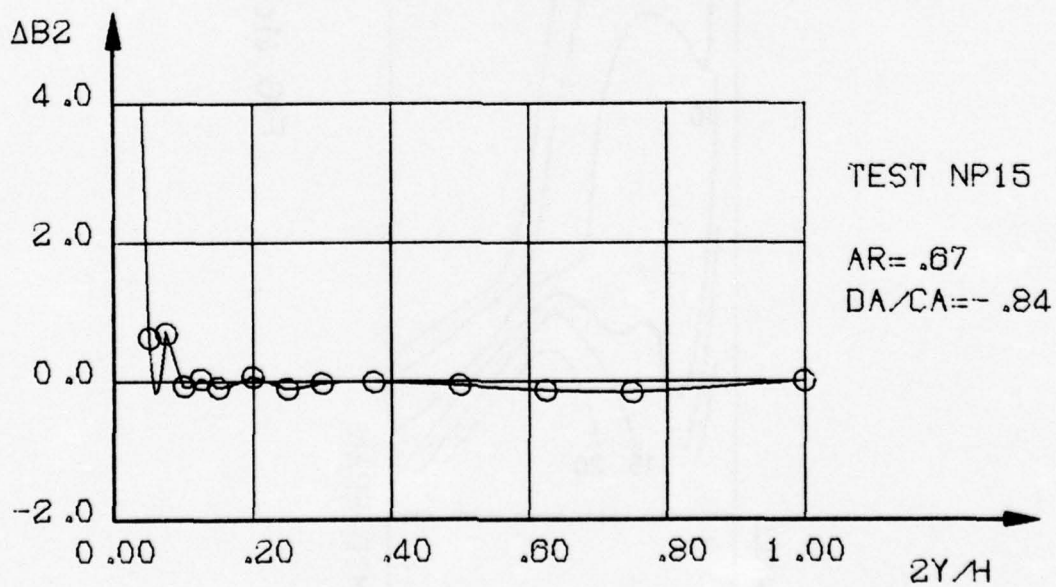


FIG. 42 b)

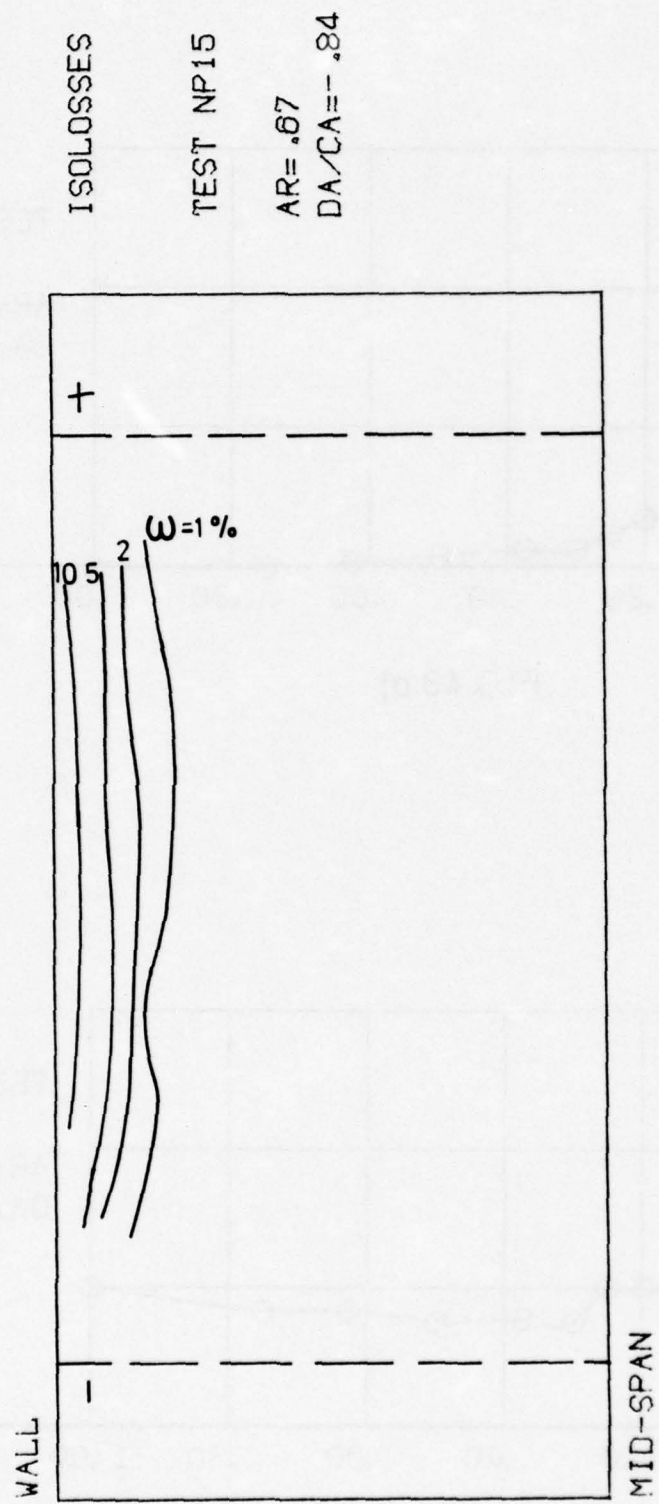


FIG 42c)

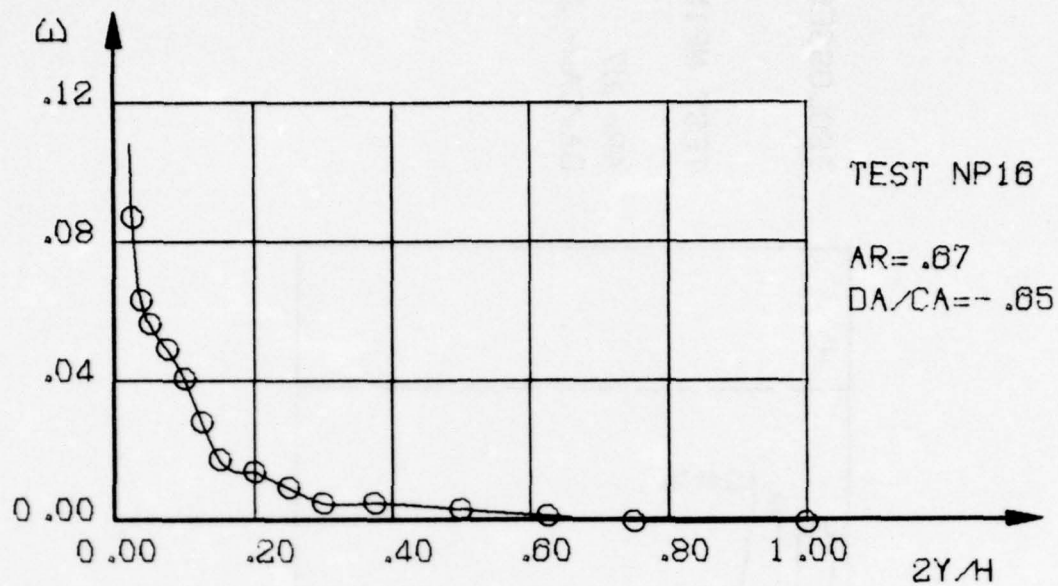


FIG. 43 a)

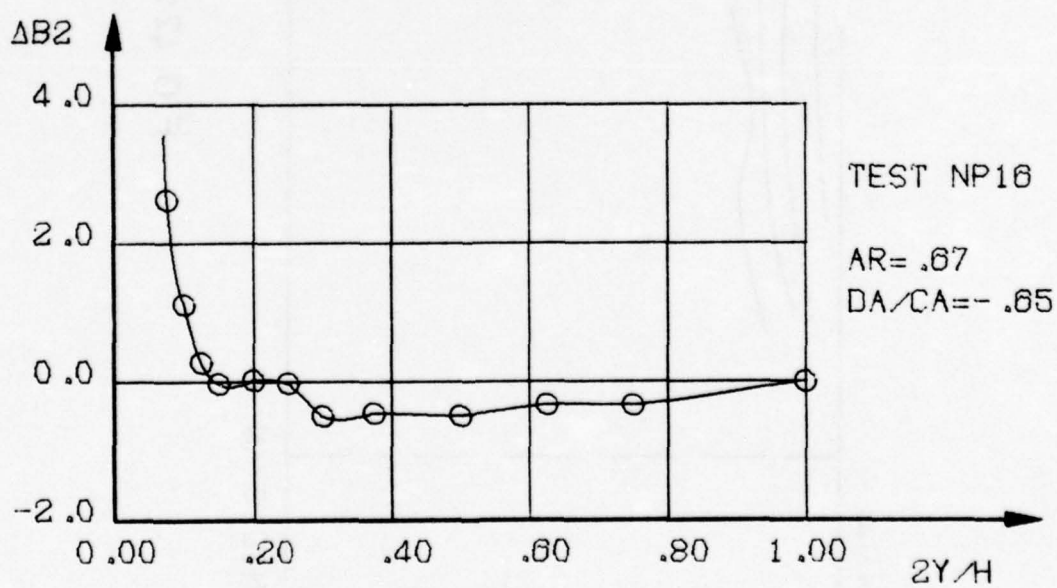


FIG. 43 b)

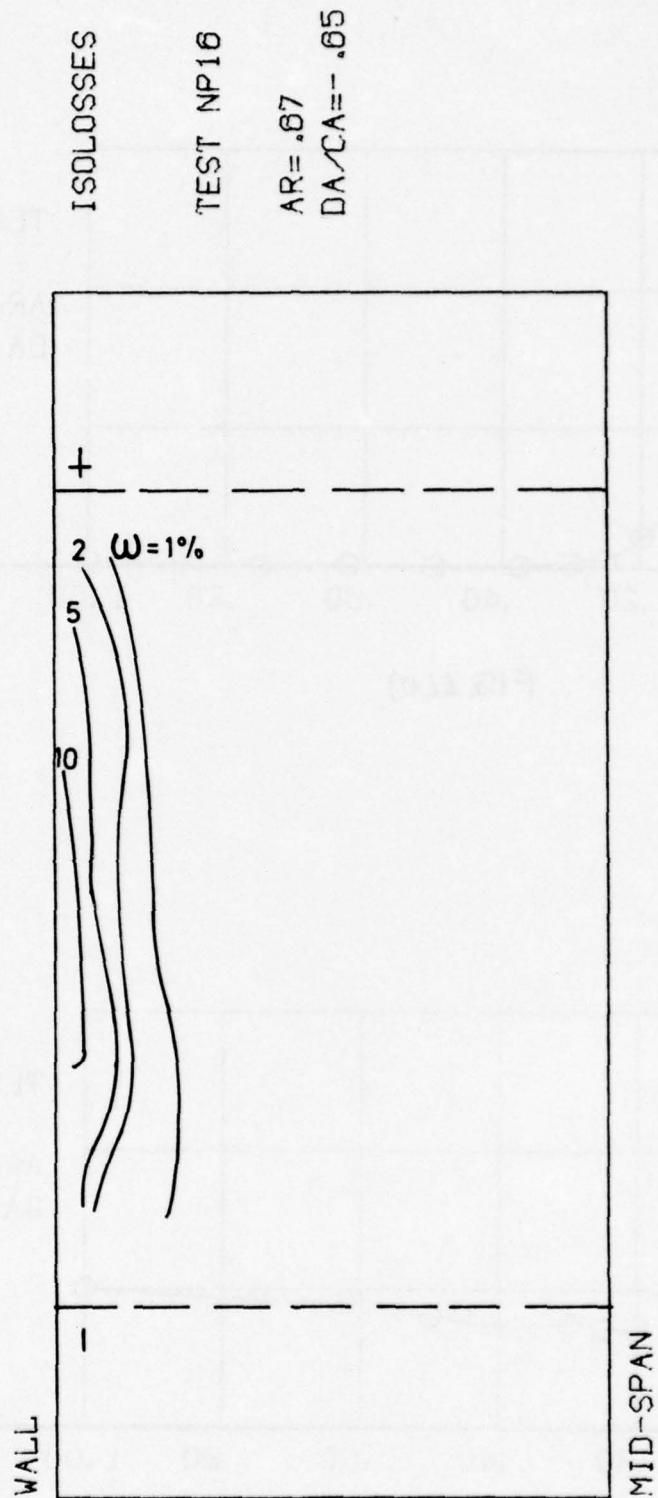


FIG 43c)

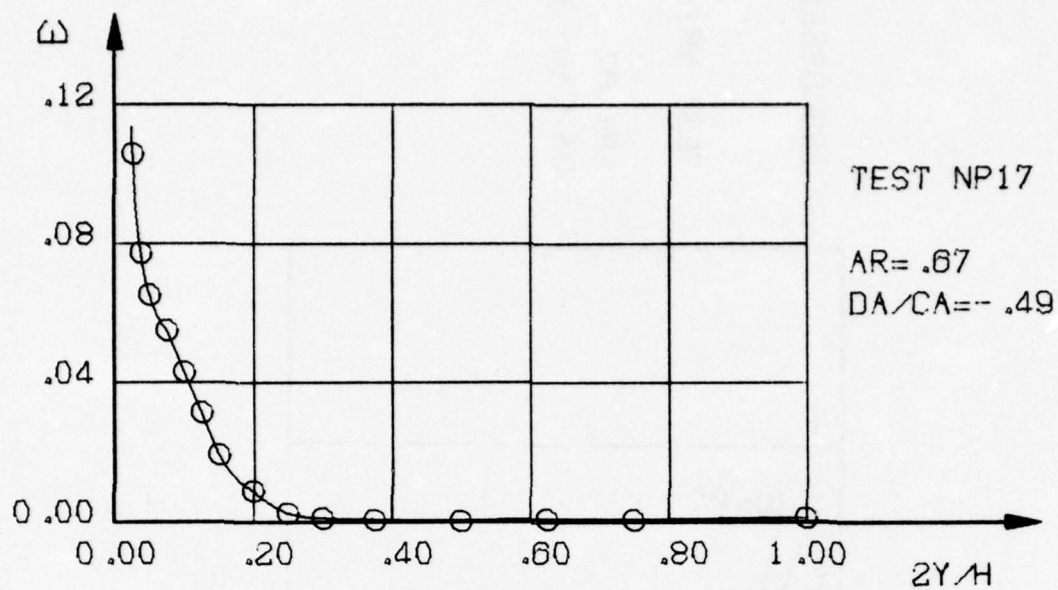


FIG. 44a)

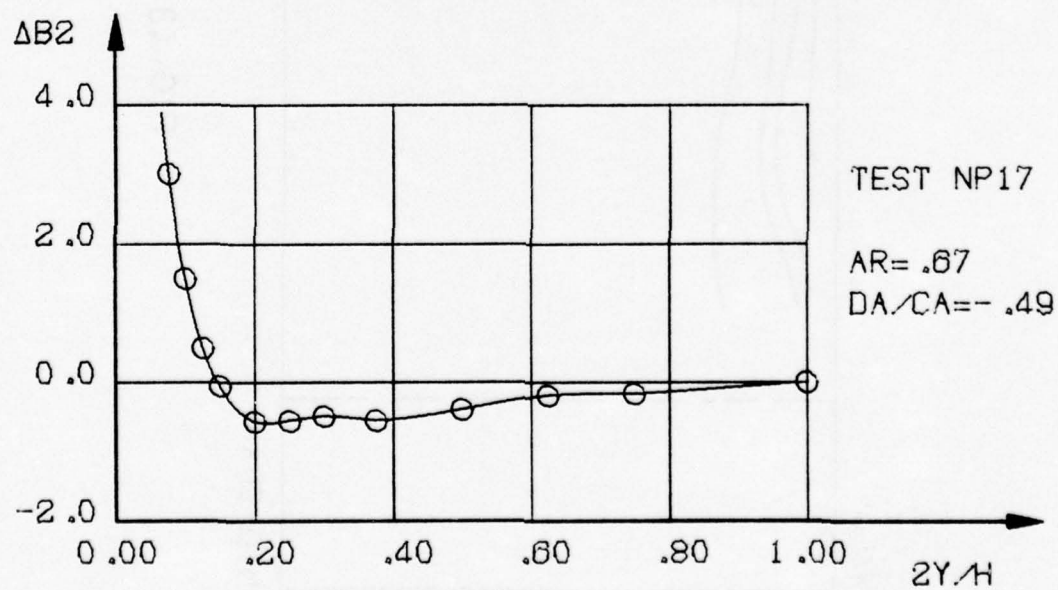


FIG. 44b)

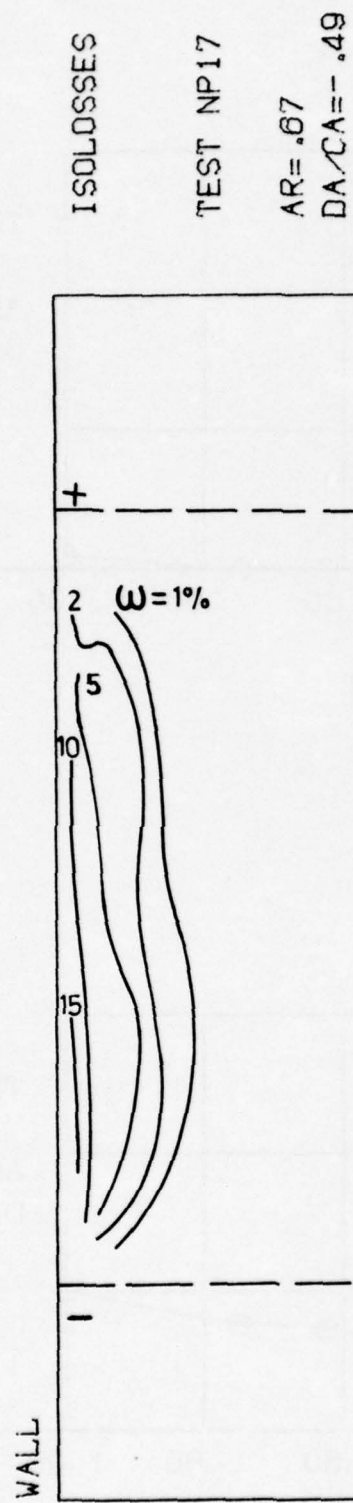


FIG.44 c)

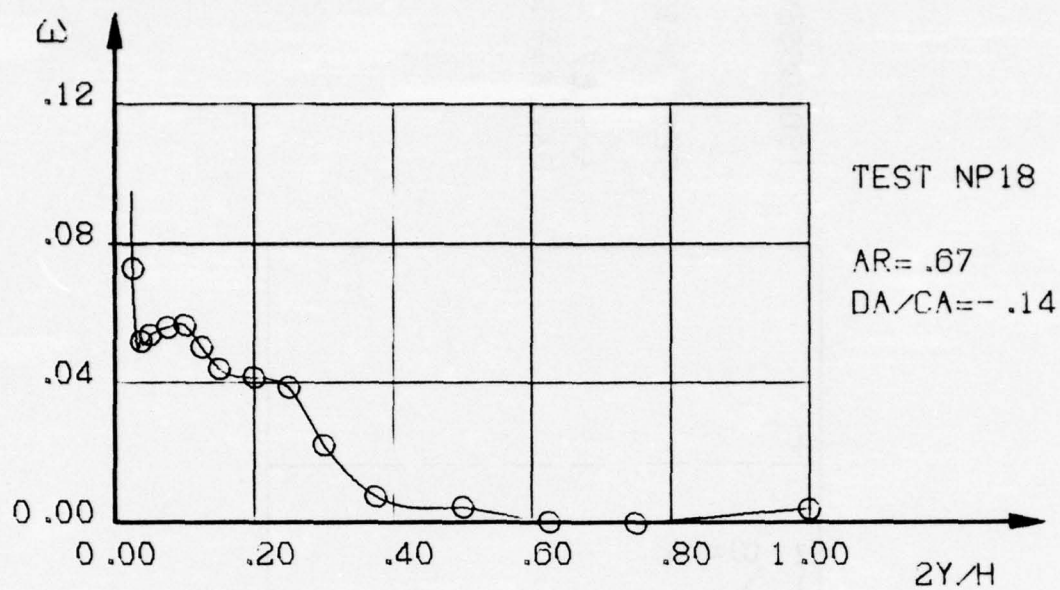


FIG. 45 a)

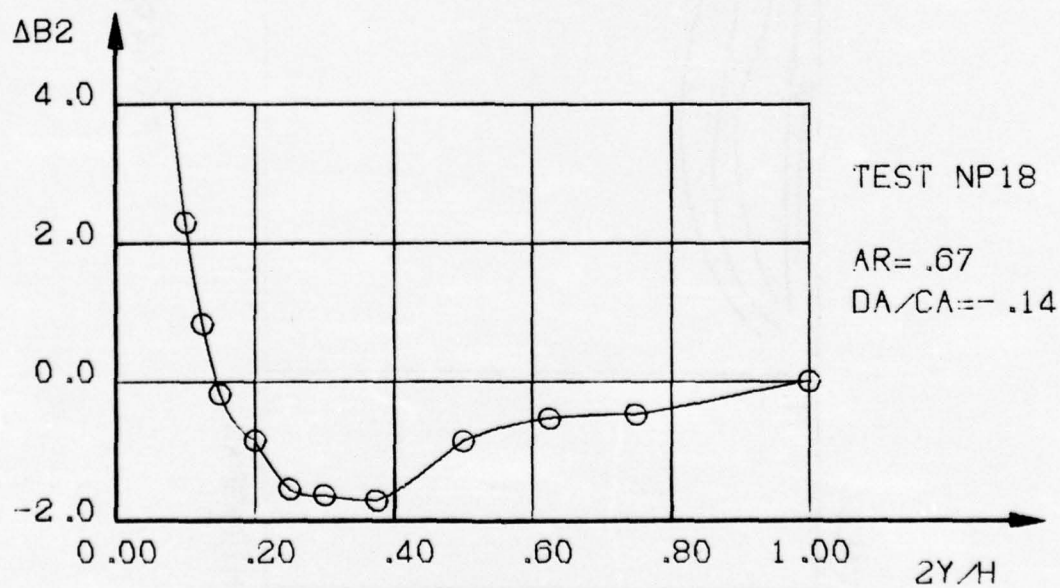


FIG. 45 b)

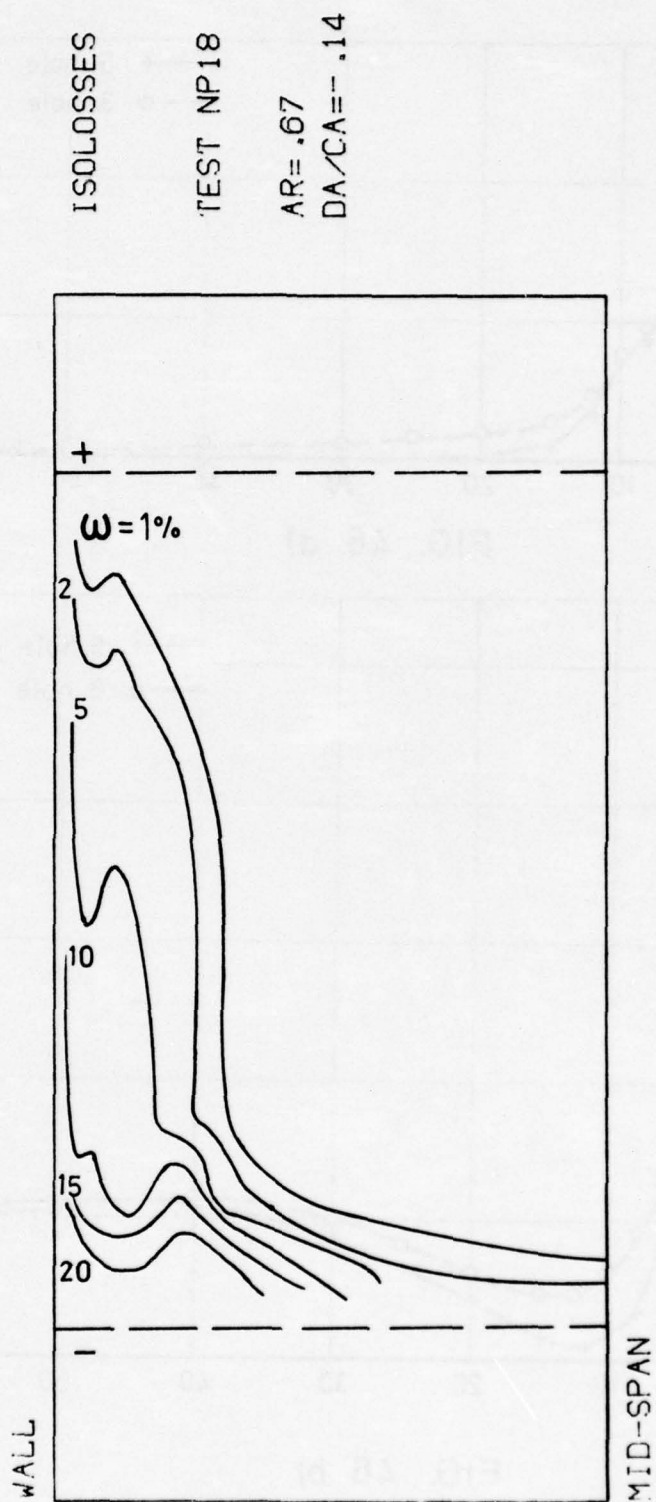


FIG 45 c)

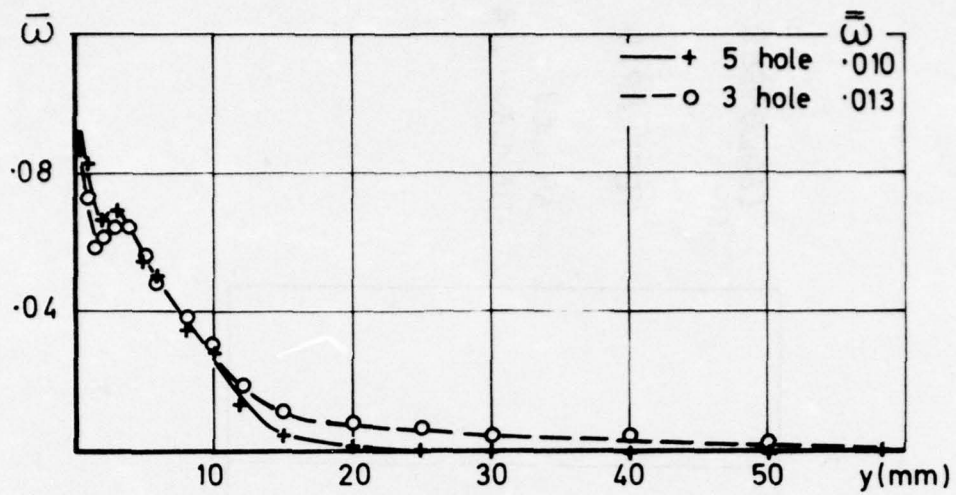


FIG. 46 a)

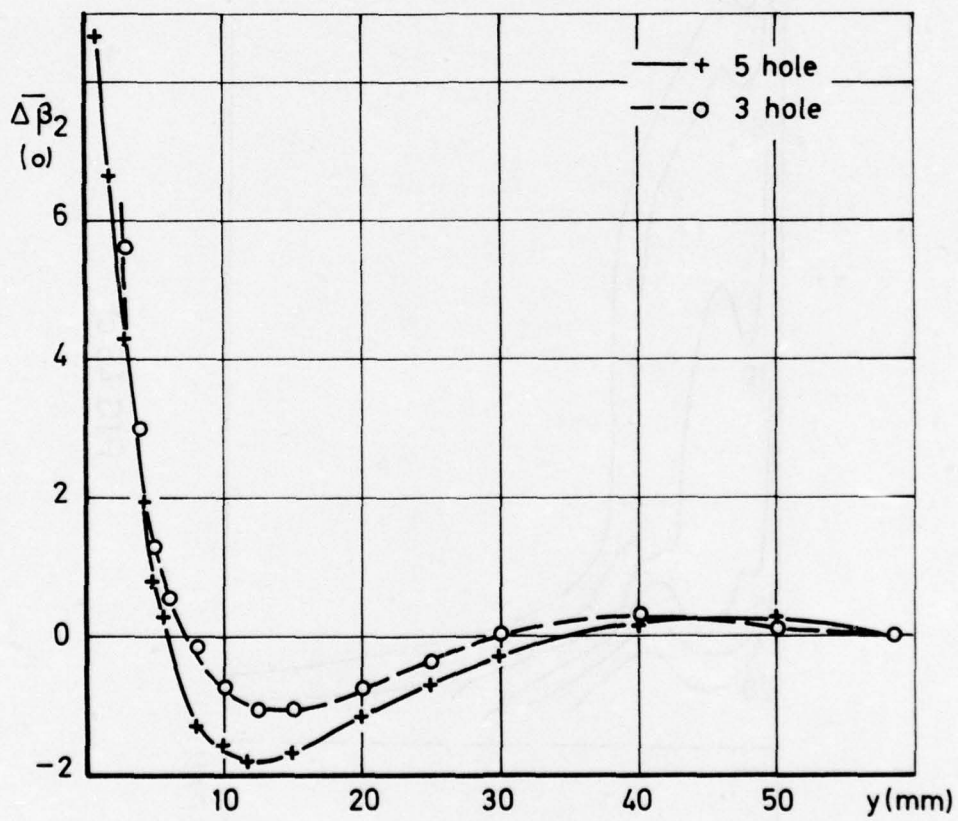


FIG. 46 b)

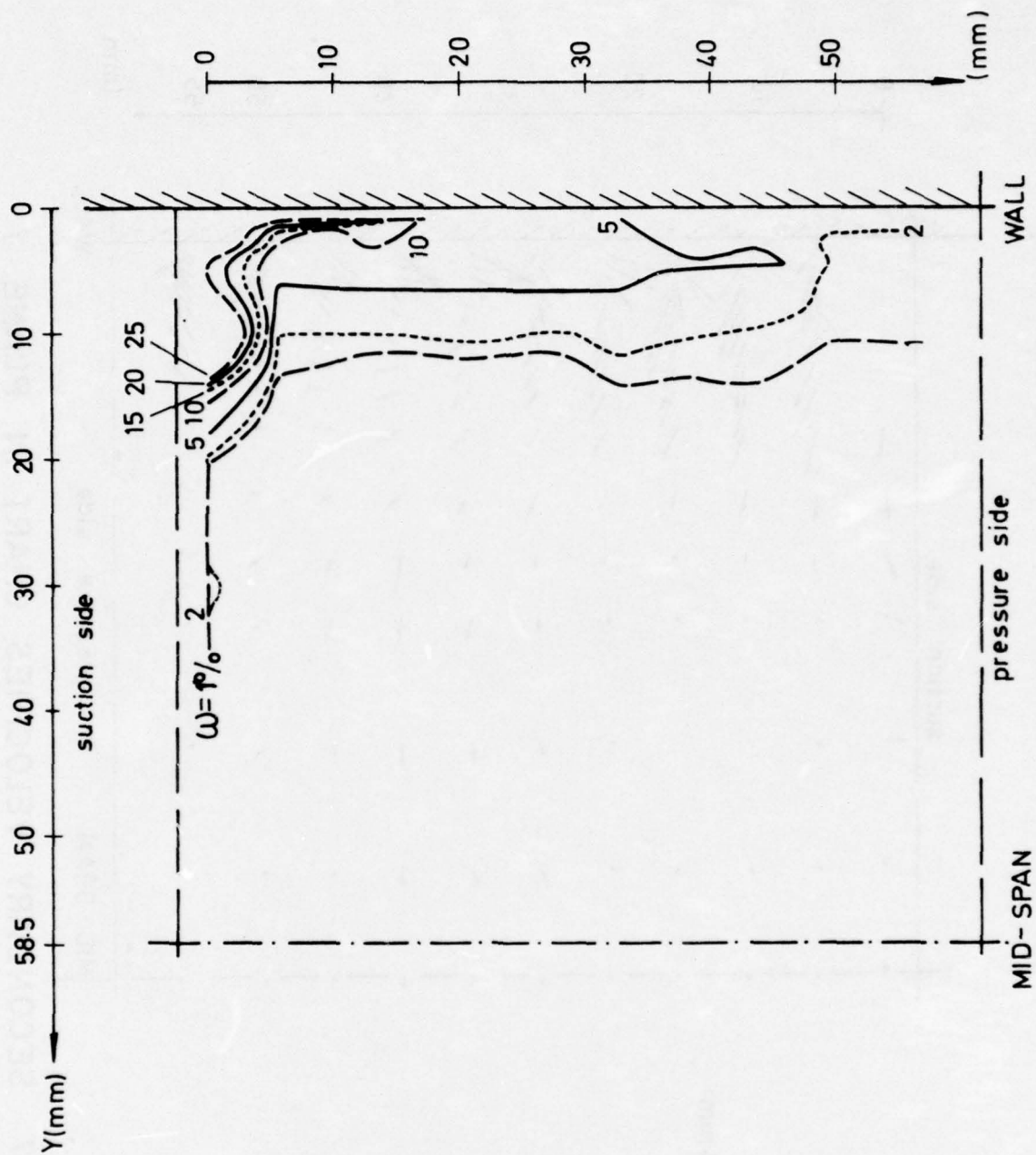


FIG. 46 c)

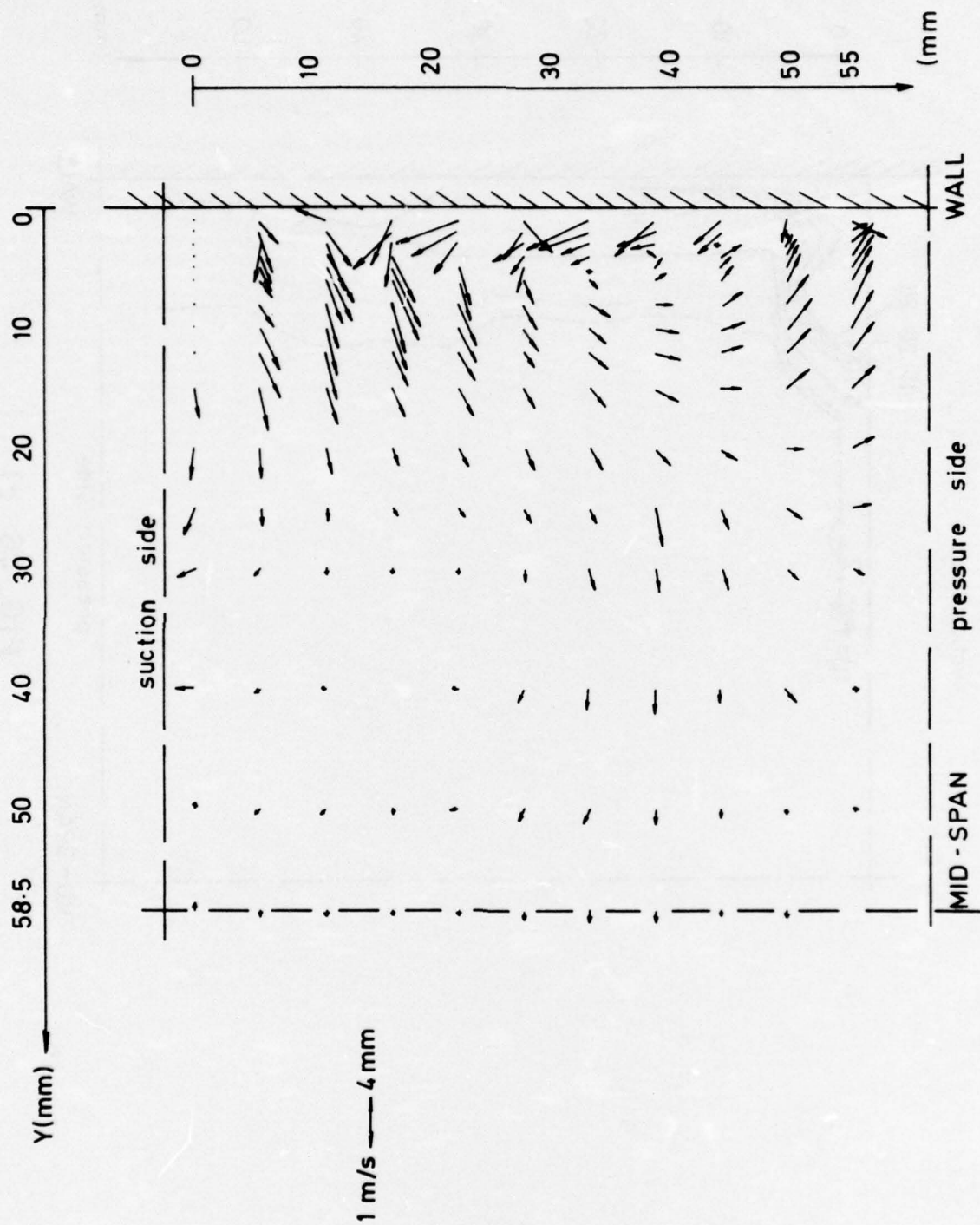


FIG. 47 SECONDARY VELOCITIES CHART IN PLANE 7

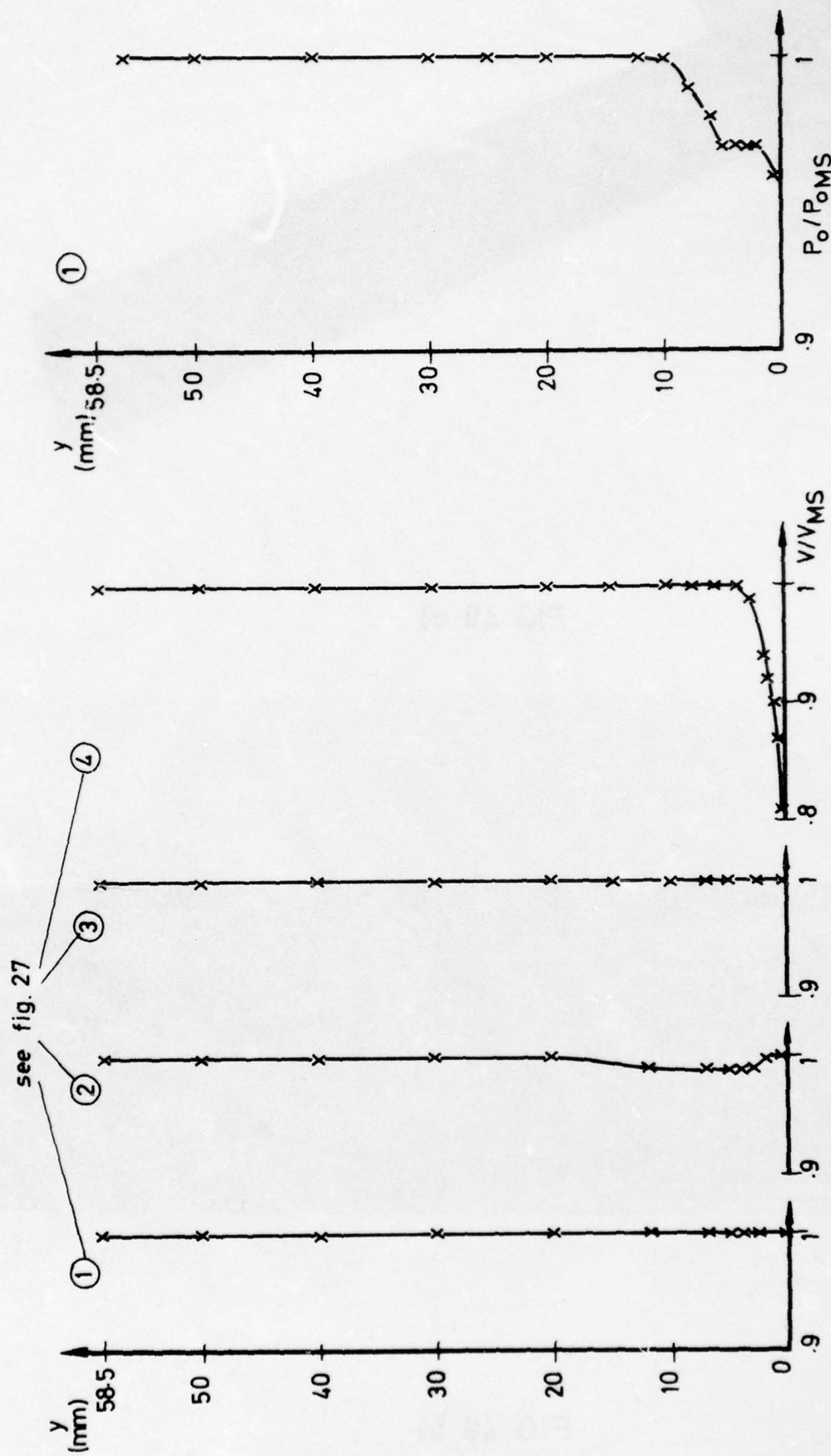


FIG. 48 a)
END-WALL VELOCITY PROFILES
(HOT - WIRE)

FIG. 48 b)
END-WALL TOTAL PRESSURE PROFILE
(5-HOLE PROBE)

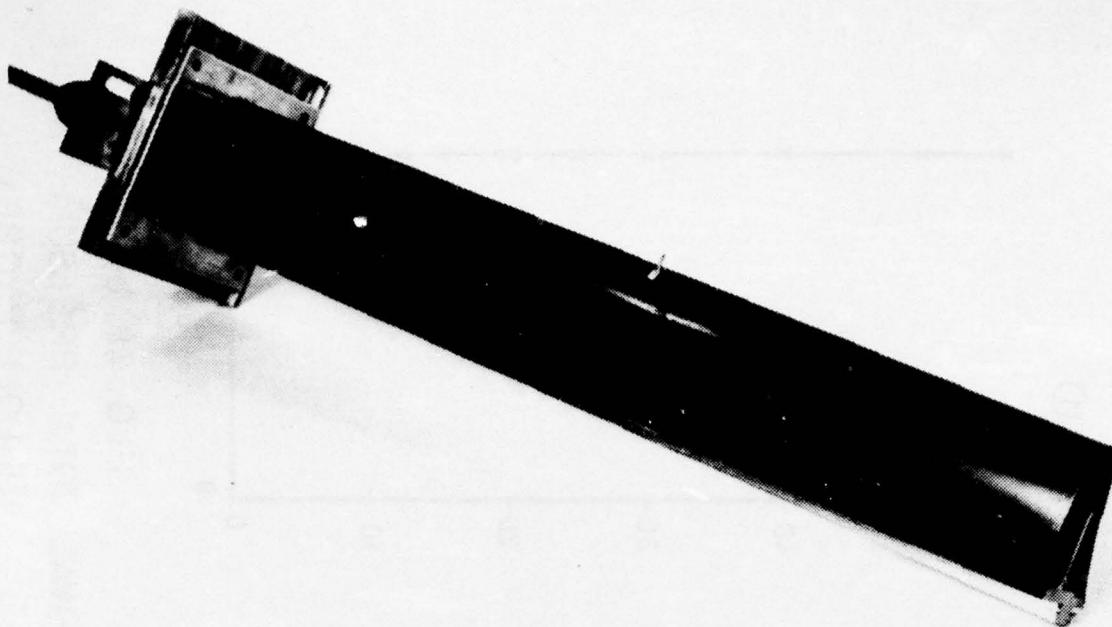


FIG 49 a)

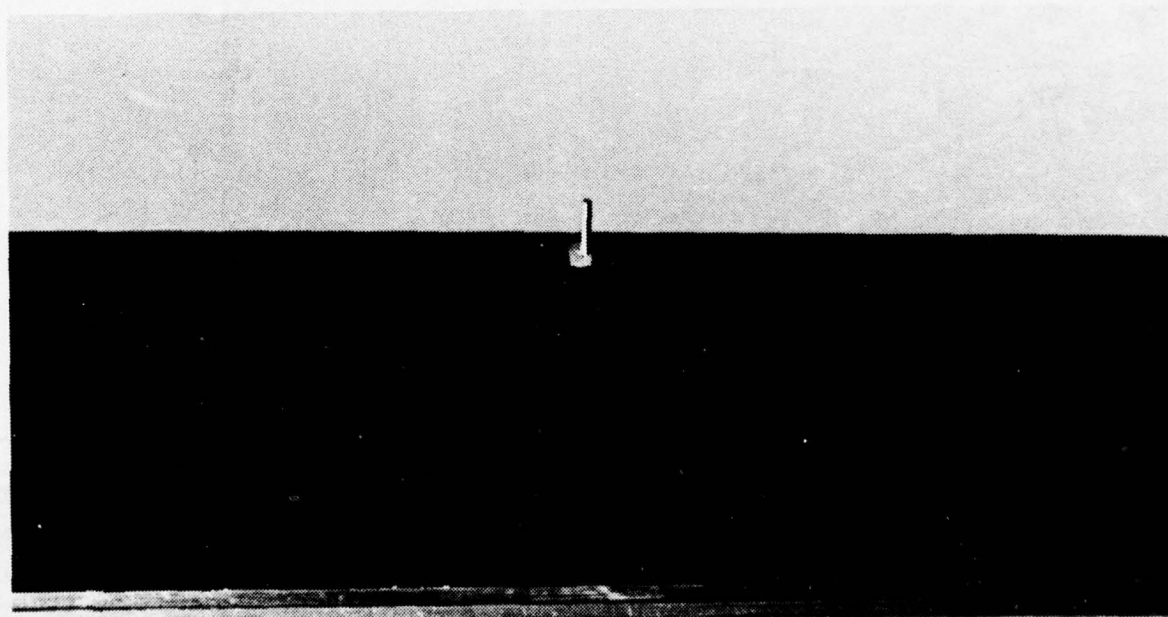


FIG 49 b)

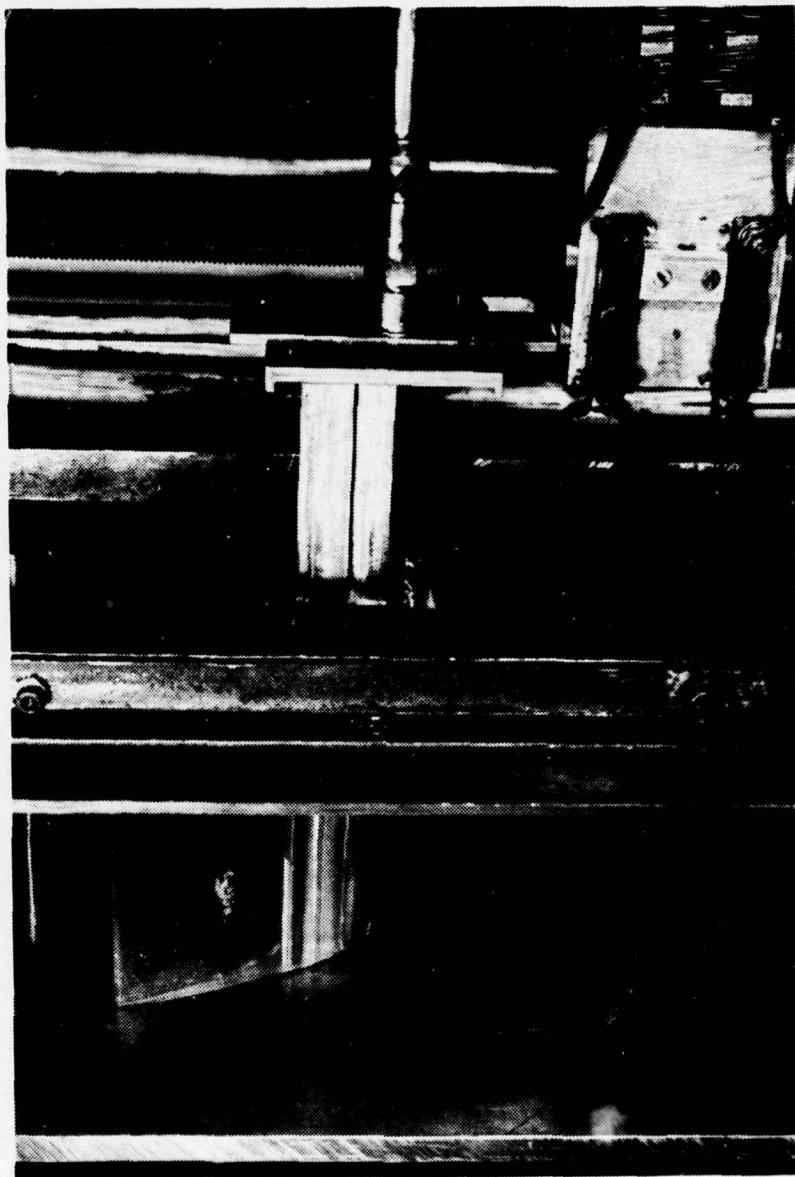


FIG. 50

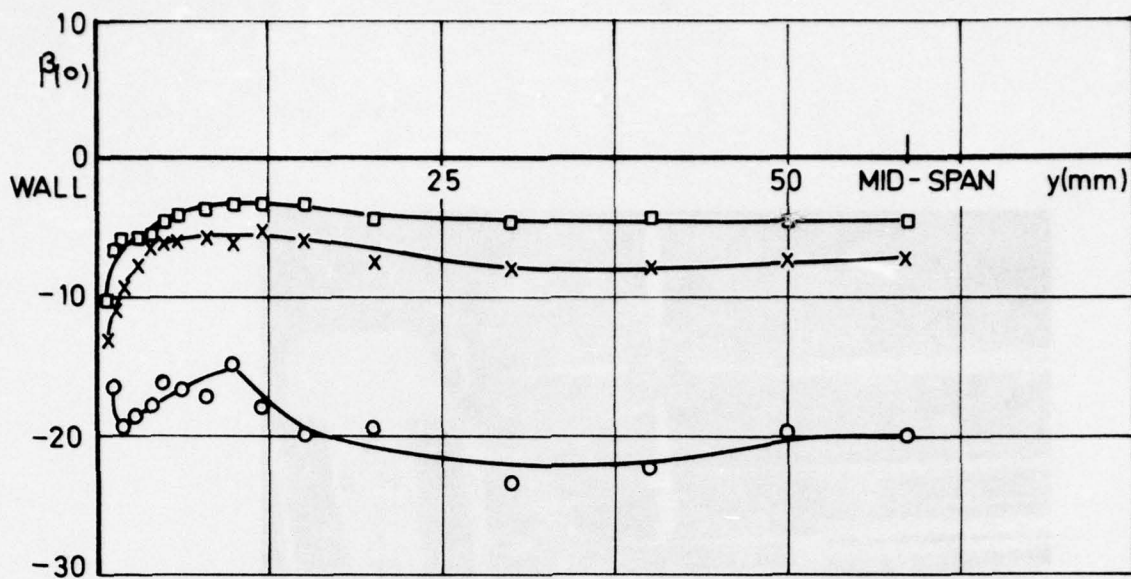


FIG. 51 a)

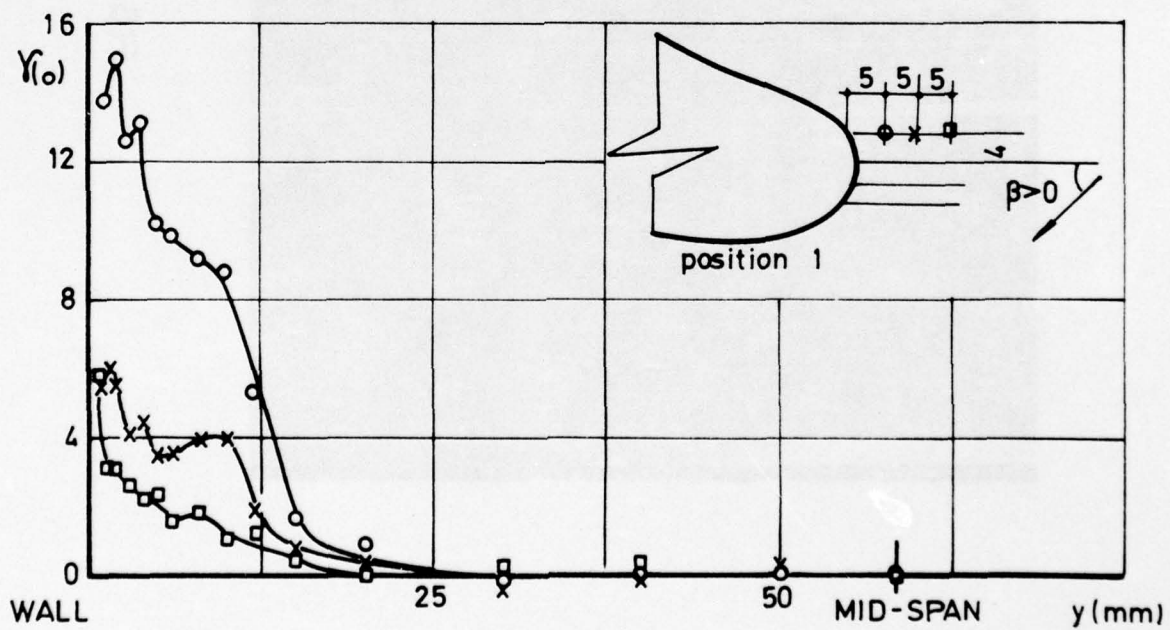


FIG. 51 b)

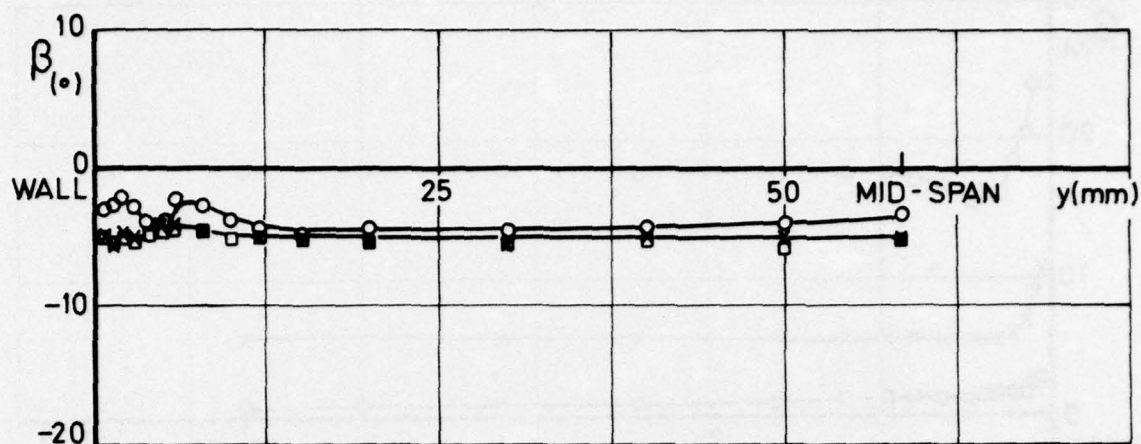


FIG 52 a)

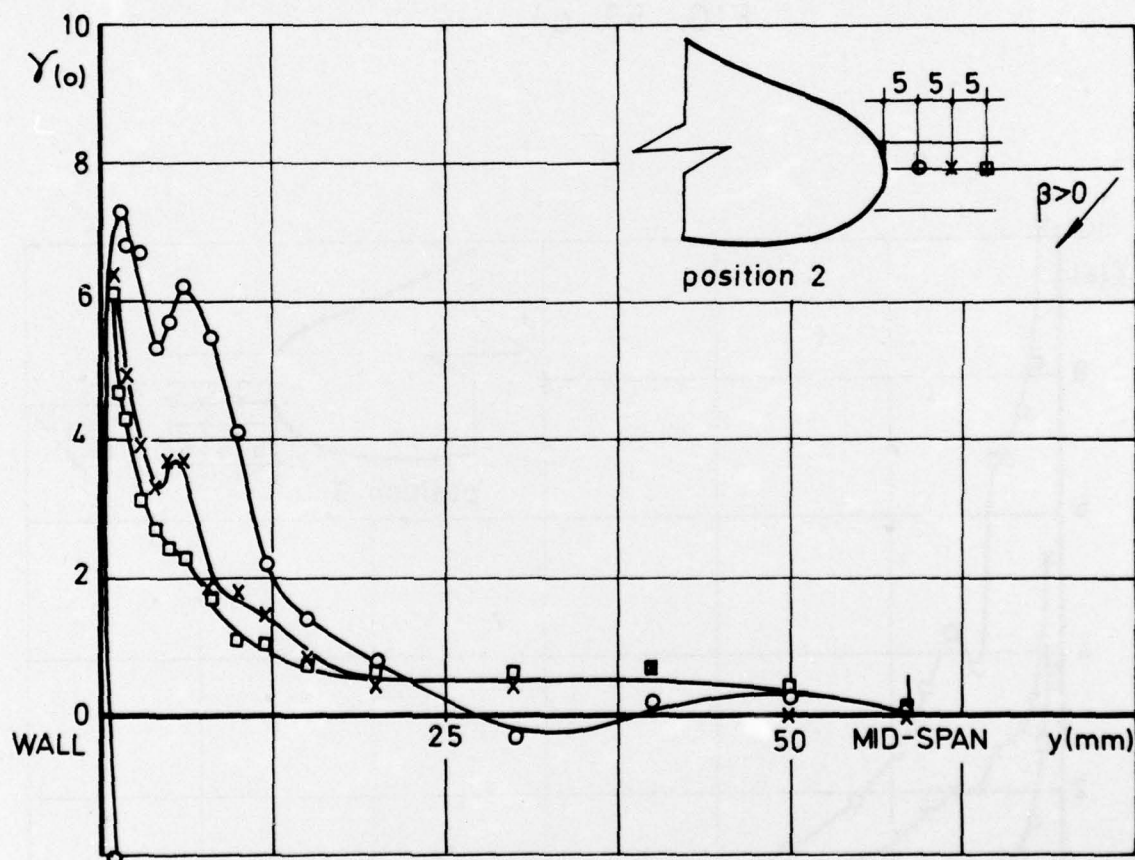


FIG. 52 b)

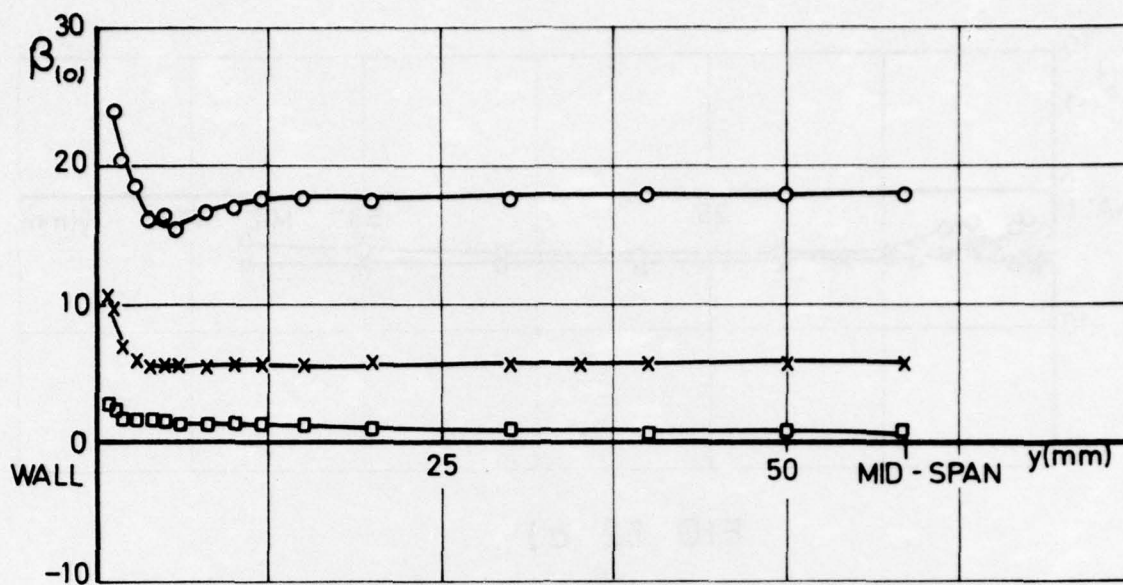


FIG. 53 a)

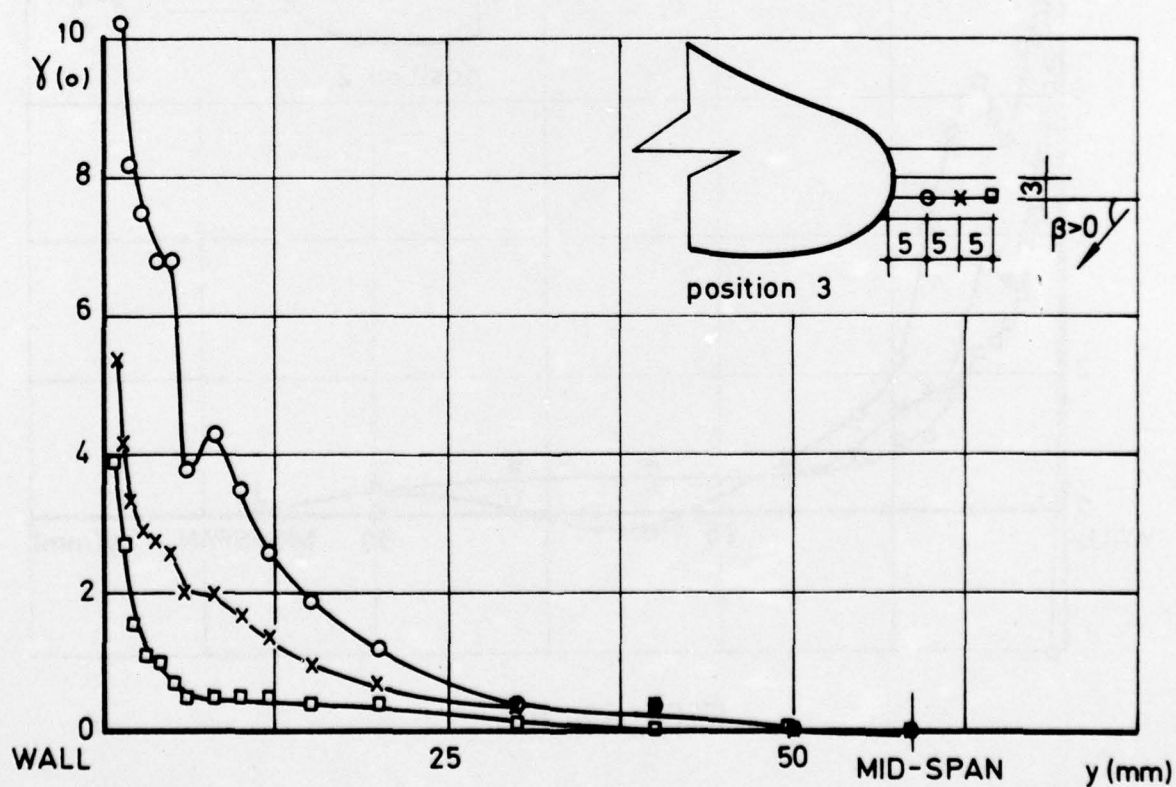


FIG. 53 b)

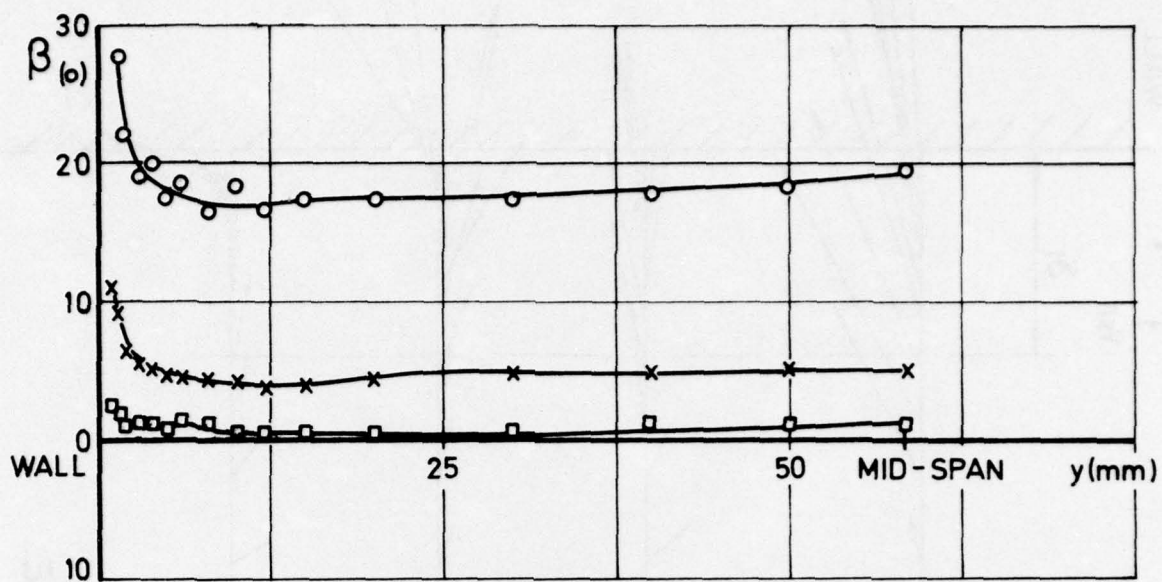


FIG. 54 a)

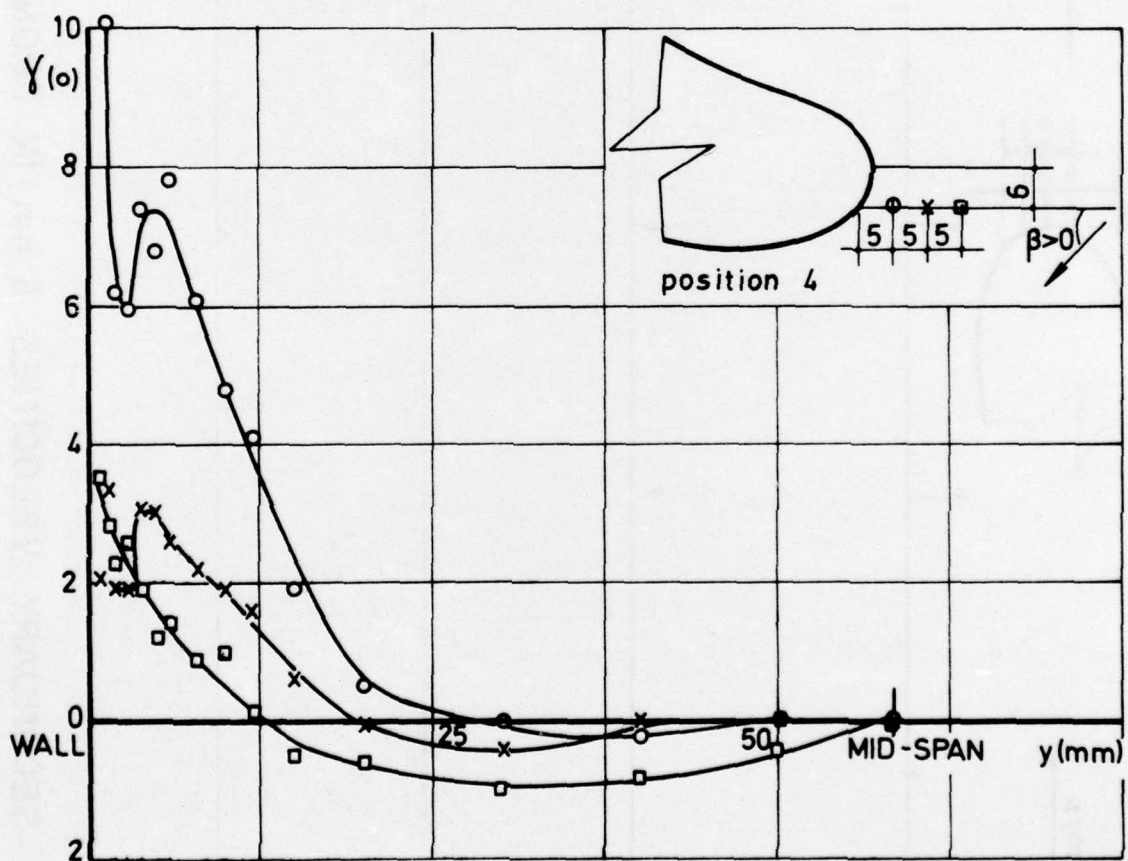


FIG. 54 b)

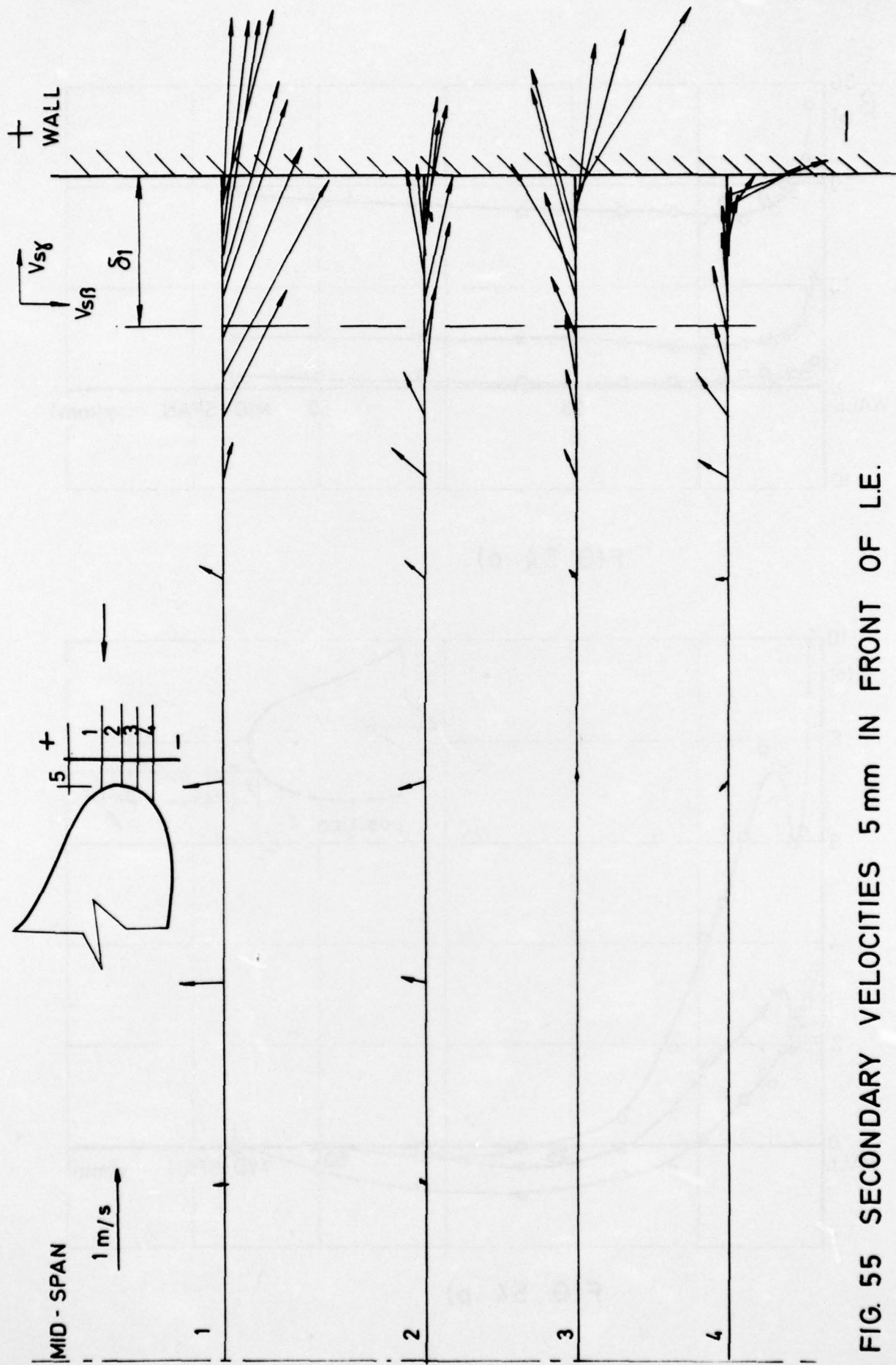


FIG. 55 SECONDARY VELOCITIES 5 mm IN FRONT OF L.E.

- 1 settling chamber
- 2 honeycomb
- 3 upper nozzle block (interchangeable)
- 4 cascade
- 5 upper cascade end wall
- 6 Perspex side wall (rotatable)
- 7 transition from rectangular to angular section
- 8 flexible outlet pipe
- 9 lower cascade end wall
- 10 lower nozzle block (movable)
- 11 inlet pipe

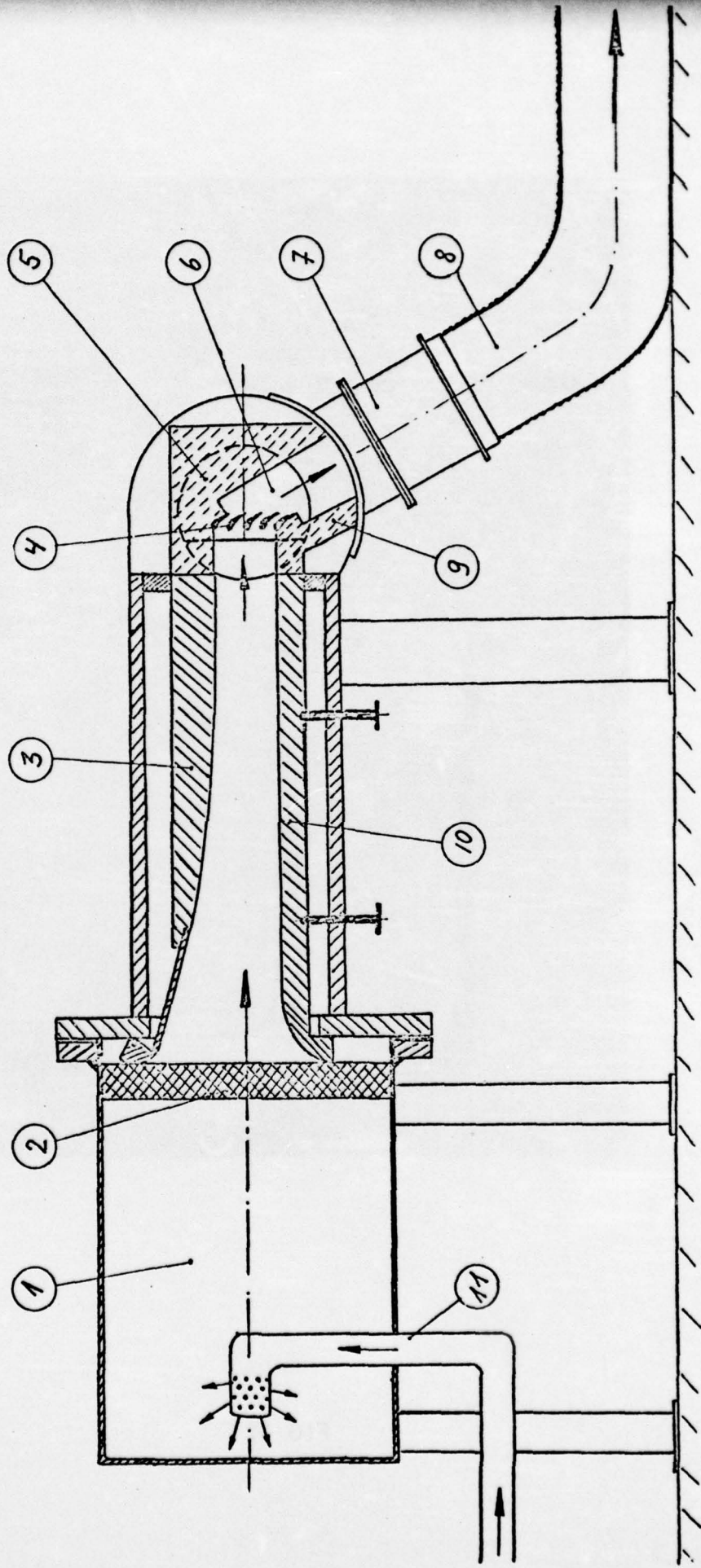


FIG. 56

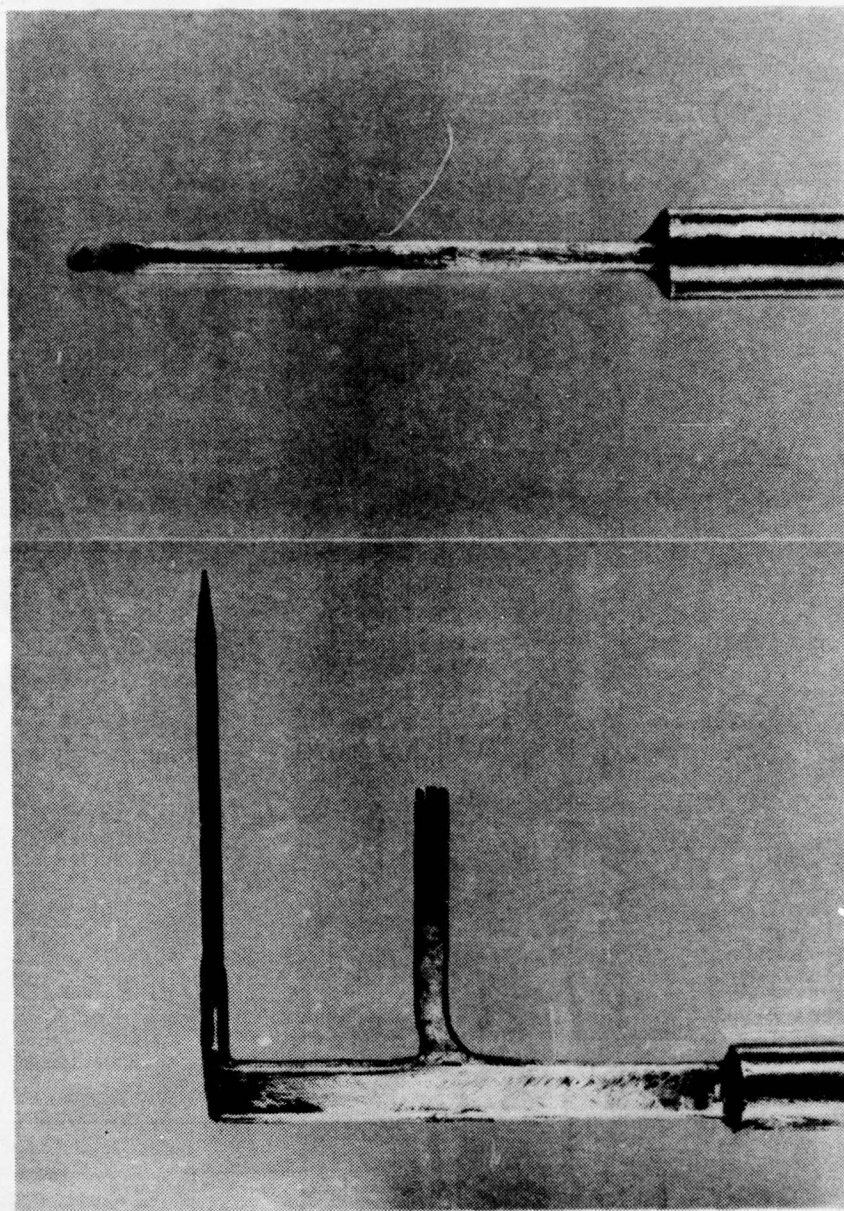


FIG. 57

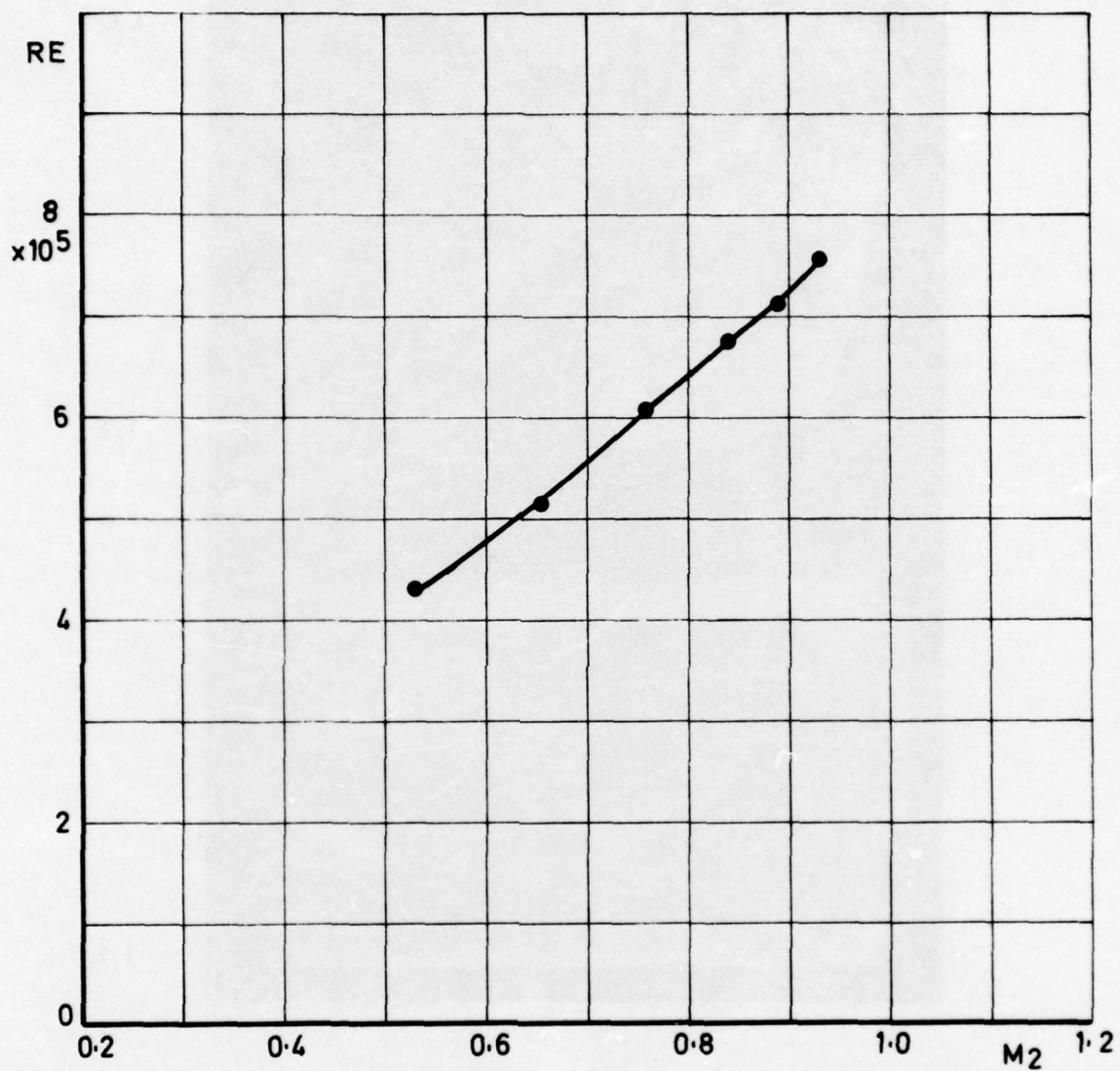
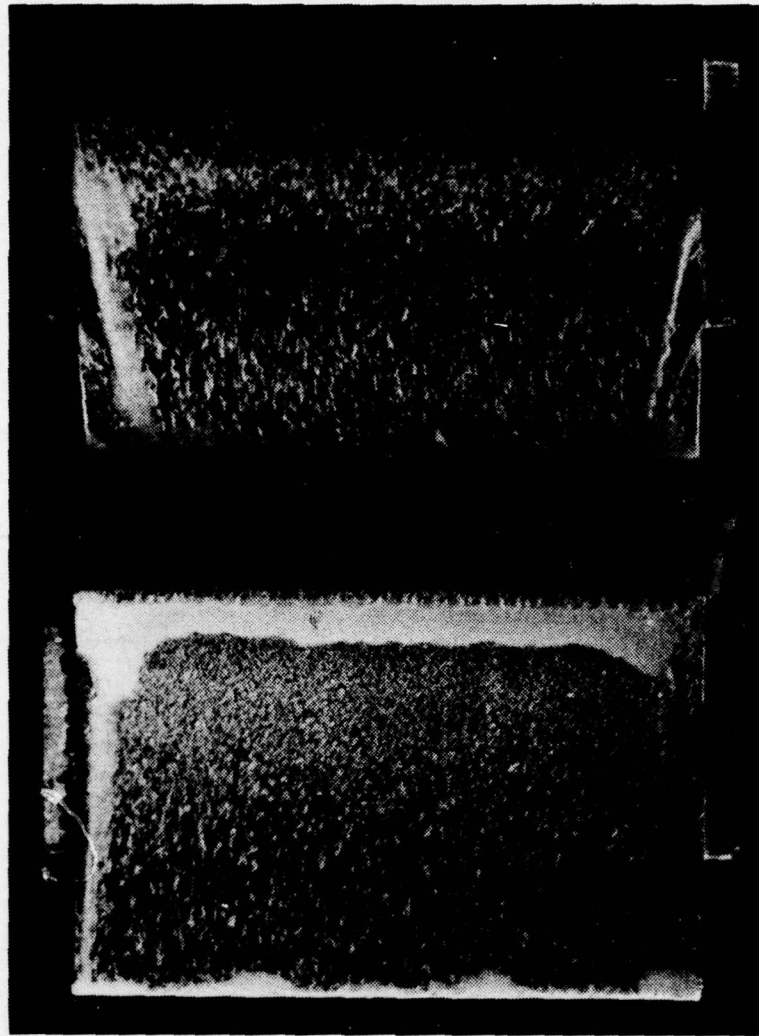


FIG. 58

SUCTION SIDE



L.E

T.E

L.E

T.E

PRESSURE SIDE

$$M_2 \approx 0,5$$

FIG. 59 - a



SIDE - WALL

$$M_2 \approx 0.5$$

FIG. 59 -b

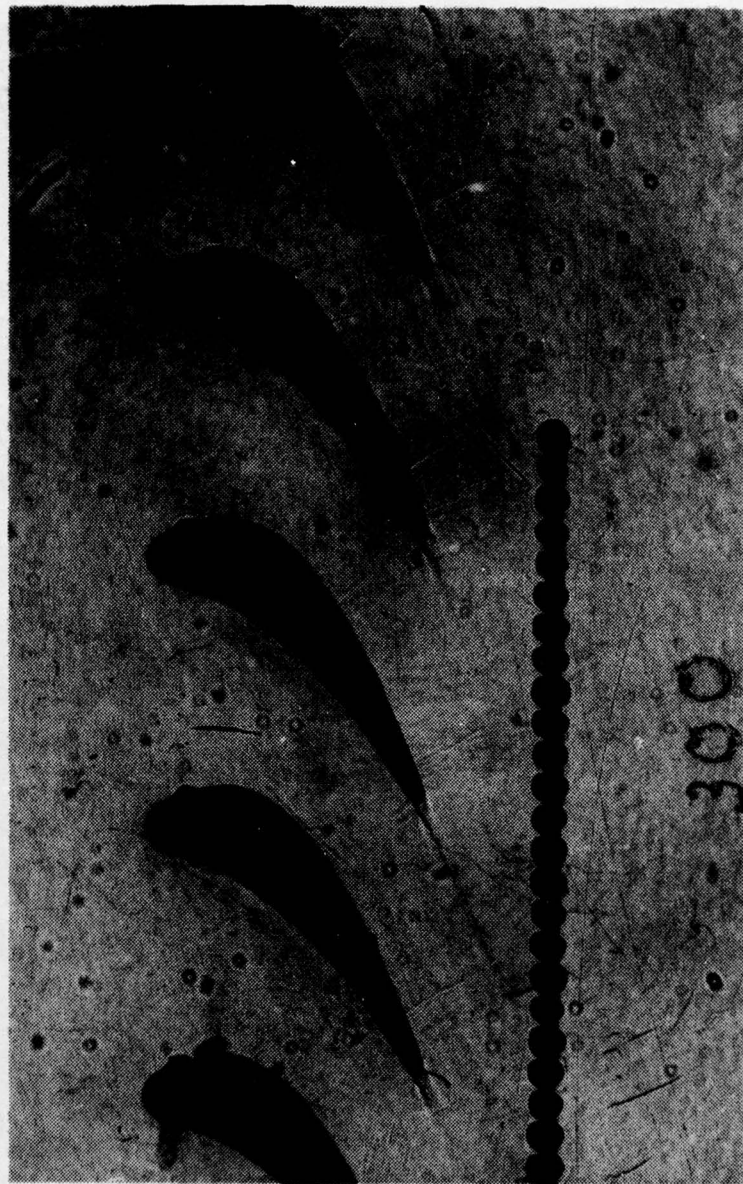
BLADE 4

5

6

7

8



$M_{2, is} = 0,92$

FIG. 60 - a

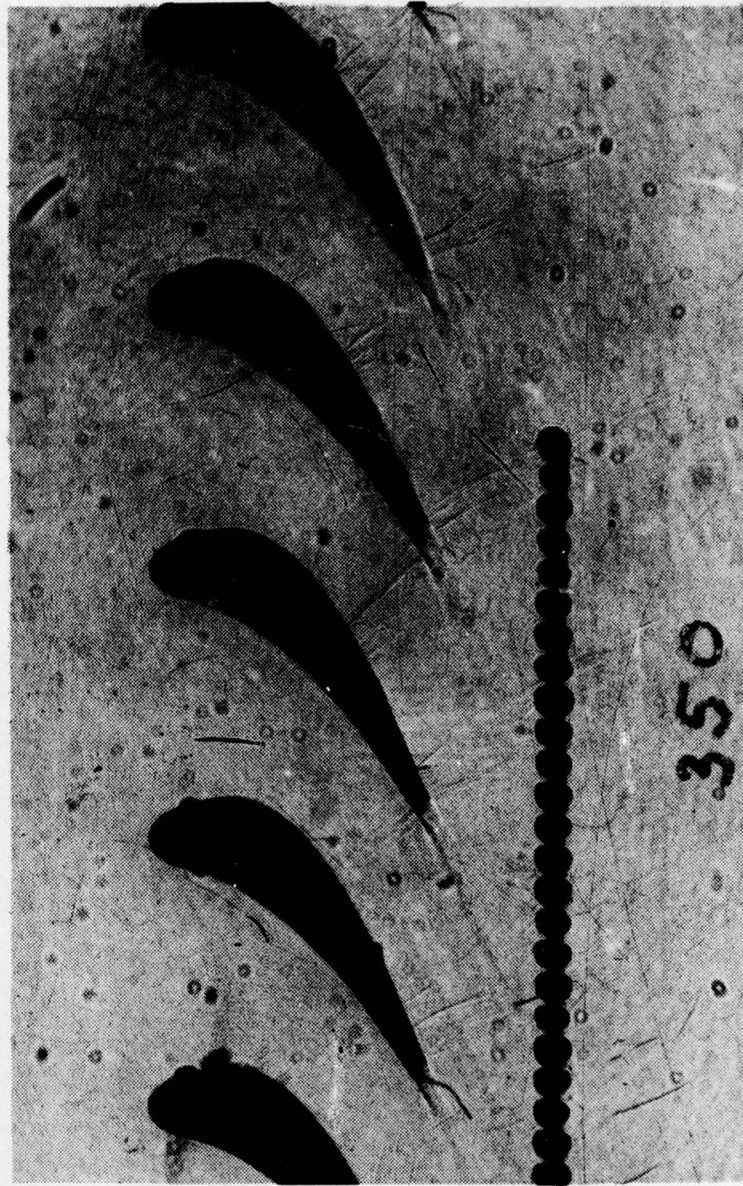
BLADE 4

5

6

7

8



$$M_{2,is} = 0,97$$

FIG. 60 - b

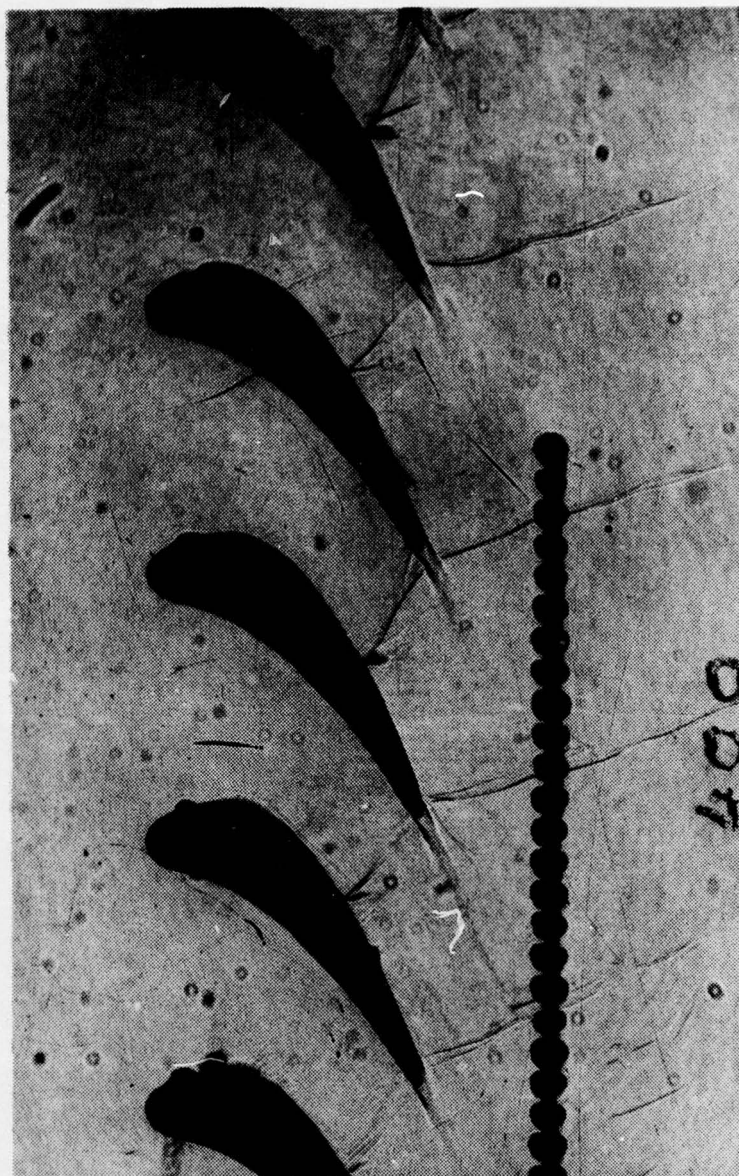
BLADE 4

5

6

7

8



$$M_{2,is} = 1,02$$

FIG. 60 - c

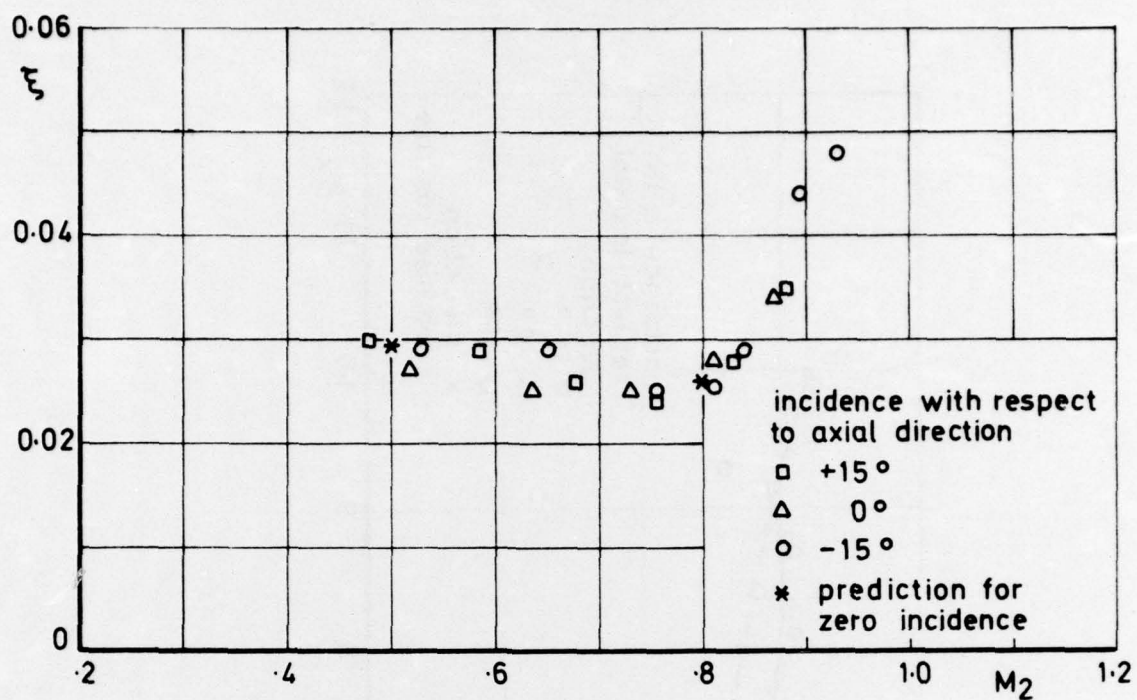


FIG. 61

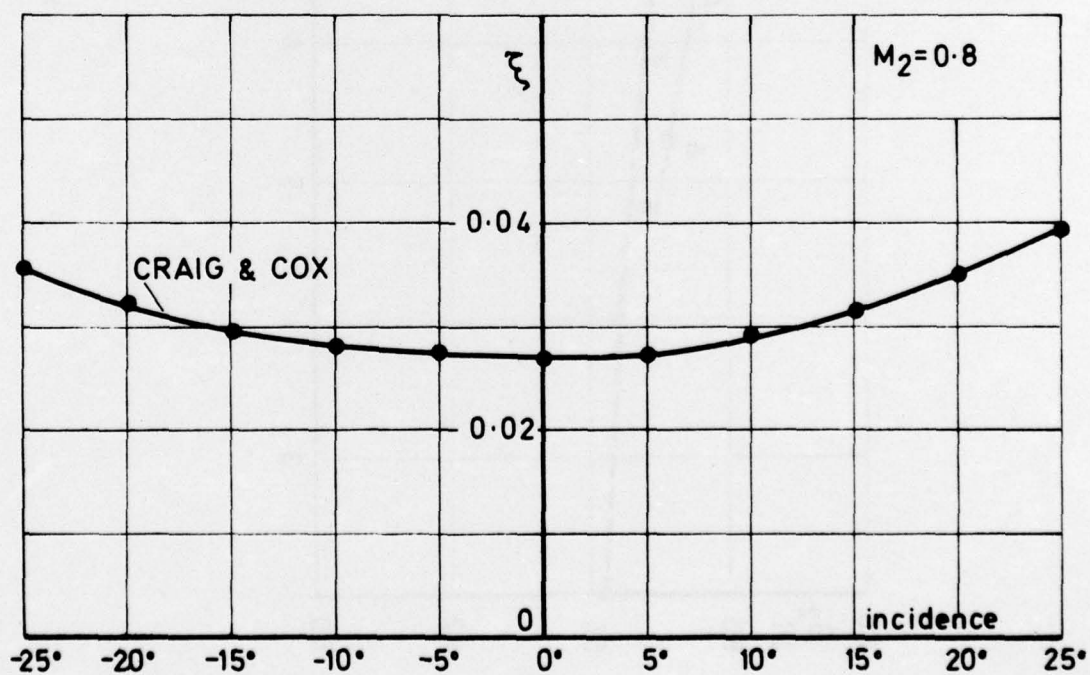


FIG. 62

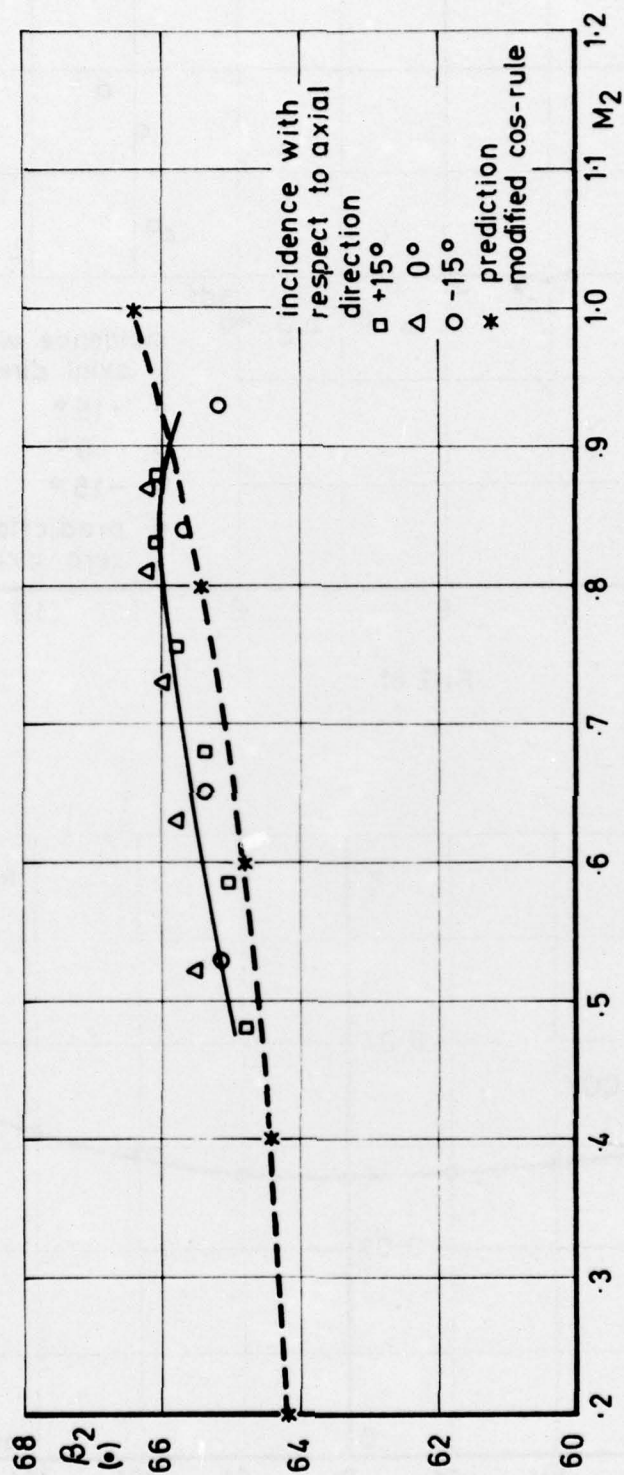


FIG. 63